

# Tabletop Coherent Extreme Ultraviolet and Soft X-ray Sources Based on High Harmonic Generation

by

Chien-Jen Lai

B.S., Electrical Engineering, National Taiwan University, 2004  
M.S., Electro-Optical Engineering, National Taiwan University, 2006

Submitted to the Department of Electrical Engineering and Computer Science  
in partial fulfillment of the requirements for the degree of

Doctor of Philosophy in Electrical Engineering

at the

MASSACHUSETTS INSTITUTE OF TECHNOLOGY

June 2014

© Massachusetts Institute of Technology 2014. All right reserved.

**Signature redacted**

Author.....  
Department of Electrical Engineering and Computer Science  
April 29, 2014

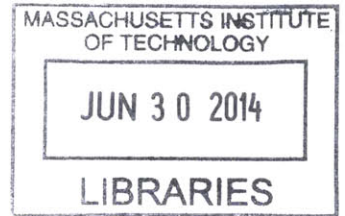
**Signature redacted**

Certified by.....  
Franz X. Kärtner  
Professor of Electrical Engineering  
Thesis Supervisor

**Signature redacted**

Accepted by.....  
Leslie A. Kolodziejski  
Professor of Electrical Engineering  
Chairman, Department Committee on Graduate Theses

ARCHIVES



**THIS PAGE IS INTENTIONALLY LEFT BLANK**

# Tabletop Coherent Extreme Ultraviolet and Soft X-ray Sources Based on High Harmonic Generation

by

Chien-Jen Lai

Submitted to the Department of Electrical Engineering and Computer Science  
on April 29, 2014,  
in partial fulfillment of the requirements for the degree of  
Doctor of Philosophy in Electrical Engineering and Computer Science

## Abstract

High harmonic generation (HHG) is a fascinating strong-field physics phenomenon that occurs when a laser pulse with a moderate intensity interacts with atoms and partially ionizes the atoms. A series of harmonics are generated at similar efficiencies and extend to a few tenth, even thousandth, order harmonics at the extreme ultraviolet (EUV) and soft X-ray range. Such an unprecedented broadband and coherent spectrum thus has many novel applications, one of which is to build tabletop coherent EUV and soft X-ray sources.

The development of EUV and soft X-ray lasers is very challenging because of the strong absorption of these wavelengths in almost all materials and the lack of appropriate reflection optics. So far, bright coherent EUV and soft X-ray sources are only available at several large-scale facilities, like free-electron lasers. However, the demands for coherent EUV sources is growing due to the advances in atomic physics, chemistry, and material science. Therefore, lab-scale EUV sources are highly desirable for these novel applications and research opportunities, and HHG emerges as a promising technology toward this goal.

This thesis will present my PhD work on HHG. It includes the numerical models developed to simulate HHG either on single-atom scale or for a macroscopic medium, the modification to the current theoretical model, the analysis of the influence of plasma defocusing on HHG, the study of the wavelength scaling of HHG efficiency and cutoff with visible and near-infrared (IR) lasers, and the generation of multi-mJ ultrashort mid-IR (2.6 mJ, 39 fs, and 2  $\mu\text{m}$  central wavelength) pulses at kHz repetition rate in the aim of extending the cutoff of HHG. With the kHz mid-IR pulses, an EUV source providing up to  $10^8$  photons/sec at 160 eV has been demonstrated, and photons in the water window range have also been detected. At the end, a chapter will summarize these research works and propose some possible future directions.

Thesis Supervisor: Franz X. Kärtner

Title: Professor of Electrical Engineering and Computer Science

**THIS PAGE IS INTENTIONALLY LEFT BLANK**



## **Acknowledgements**

First of all, I thank my advisor Prof. Franz Kärtner for the opportunity to work and study in the Optics and Quantum Electronics Group at MIT. I have enjoyed the nice lab environment, the exuberant academic atmosphere, and the fruitful discussions about research. Prof. Kärtner is a great mentor and research supervisor. His enthusiasm and insight in science always inspire me. I feel very fortunate to work under his guidance and supervision during my PhD study.

I thank my colleagues at MIT for their kind help in my research. I have enjoyed working with Dr. Kyung-Han Hong and Dr. Jeffrey Moses, and have learnt a lot from their expertise. I thank the talented labmates: Edilson Falcão-Filho, Giovanni Cirimi, Donnie Keathley, Louis Chang, Jonathas Siquera, Gregory Stein, and Peter Krogen. Without them, the HHG experiment in our lab would be impossible. I also appreciate the administrative support from our assistants Dorothy Fleischer and Donna Gale.

I would like to thank the Republic of China (Taiwan) Student Association at MIT and especially those who also work in the OQE group (Hsiang-Chieh Lee, Li-Jin Chen, Tsung-Han Tsai, Hung-Wen Chen, Shu-Wei Huang, and Jonathan Liu). They made my life in PhD study so wonderful.

Finally and most importantly, I wish to express my highest personal gratitude to my parents. Without their love, care and encouragement, I could not finish my PhD and this thesis. This thesis is dedicated to them.

**THIS PAGE IS INTENTIONALLY LEFT BLANK**

# Table of Contents

|  |           |
|--|-----------|
| <b>Chapter 1 Introduction to High Harmonic Generation .....</b>                        | <b>1</b>  |
| 1.1 High Harmonic Generation .....   | 1         |
| 1.2 Applications of High Harmonic Generation .....                                     | 5         |
| 1.3 About This Thesis .....  | 7         |
| <b>Chapter 2 Microscopic Picture of High Harmonic Generation .....</b>                 | <b>9</b>  |
| 2.1 Time-Dependent Schrödinger Equation Simulation .....                               | 10        |
| 2.2 The Three-Step Model .....   | 16        |
| 2.3 Wavelength Scaling of the Single Atom Efficiency .....                             | 23        |
| 2.4 Multiphoton and Non-adiabatic Effects .....  | 29        |
| 2.5 Conclusion .....   | 35        |
| <b>Chapter 3 Macroscopic Effects: Phase-Matching and Plasma Defocusing .....</b>       | <b>39</b> |
| 3.1 Phase-Matching .....   | 40        |
| 3.2 Plasma Defocusing .....  | 45        |
| 3.3 Fully Dimensional Simulation .....   | 56        |
| 3.4 Medium Length .....  | 65        |
| 3.5 Conclusion .....   | 69        |
| <b>Chapter 4 High Harmonic Generation Driven by Ti:Sapphire Based Lasers .....</b>     | <b>71</b> |
| 4.1 Comparison between 400nm and 800nm Driver Wavelengths .....                        | 72        |
| 4.2 Cutoff of HHG Spectrum in the EUV Regime with Visible Driver Wavelengths .....     | 76        |
| 4.3 Wavelength-Scaling of Single-Atom Efficiency .....                                 | 81        |
| 4.4 Conclusion .....   | 85        |
| <b>Chapter 5 High Harmonic Generation Driven by Mid-Infrared Ultrashort Pulses ...</b> | <b>87</b> |
| 5.1 Optical Parametric Chirped Pulse Amplification .....                               | 87        |
| 5.2 Cryogenic Yb:YAG System .....  | 91        |

|   |            |
|---|------------|
| 5.3 HHG Results .....                             | 95         |
| <b>Chapter 6 Conclusion and Future Work .....</b> | <b>99</b>  |
| 6.1 Conclusion .....                              | 99         |
| 6.2 Future Work .....                             | 102        |
| <b>Bibliography .....</b>                         | <b>105</b> |

# Chapter 1

## Introduction to High Harmonic Generation

### 1.1 High Harmonic Generation

The invention of lasers has made it possible to drive the polarization in materials with an intense electric field to which the response of materials is no longer linear, and therefore nonlinear optics has emerged as an essential research field. To describe nonlinear optical phenomena, one approach is to expand the polarization  $P$  driven by the driver field  $E$  by the following expansion [1]:

$$P = \chi_1 E + \chi_2 E^2 + \chi_3 E^3 + \dots \quad (1.1)$$

The above expansion has successfully explained many nonlinear optical phenomena, like second harmonic generation [2], self focusing [3], optical parametric amplification [4], etc. The expansion converges and is valid in the perturbative regime in which the applying field  $E$  is smaller than some characteristic field strength  $E_a$  in the order of the internal Coulomb field between atoms and electrons, and the strength of the  $q^{\text{th}}$  order nonlinear polarization should scale as  $(E/E_a)^q$ . However, as the laser technology advances, particularly with the advent of high-energy ultrashort pulse generation techniques, the laser field strength has

reached the internal field  $E_a$  around  $10^{14}\sim 10^{16}$  W/cm<sup>2</sup>, and Eq. (1.1) does not always converge. Nonlinear optics has come to a new regime called the strong field regime.

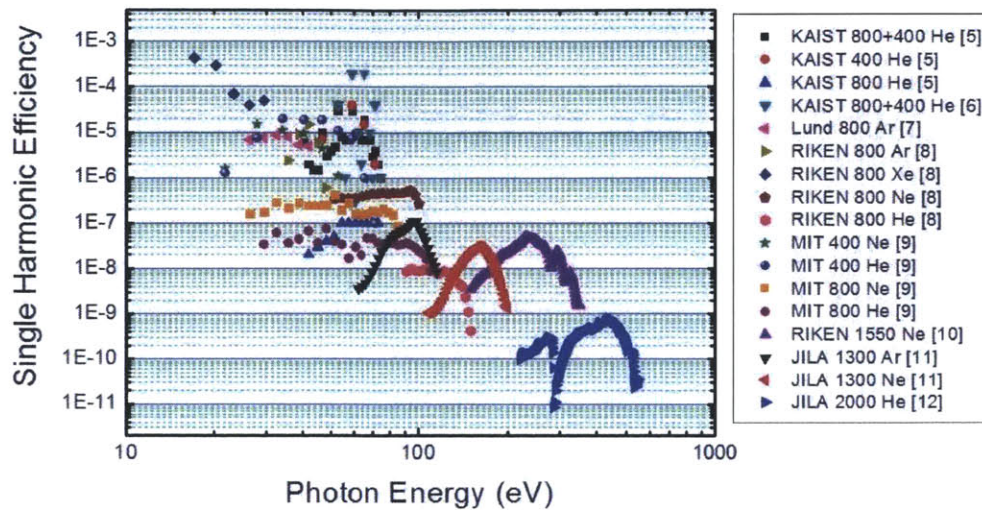


Fig. 1-1 HHG efficiencies and spectra from various driver wavelengths and gas media [5-8]. The names are the institutes where the experiments were done, the numbers are the driver wavelengths in nm, and the chemical formulas are the gas species used in the experiments.

There are several interesting strong-field phenomena, and a fascinating one is high harmonic generation (HHG). When a laser pulse is focused on a gas target with an intensity that is comparable to the internal atomic field on the valence electrons, the gas atoms can coherently emit a series of very high-order odd harmonics of the laser pulse at similar conversion efficiencies, and this phenomenon is named as HHG. Fig. 1-1 shows some HHG spectra from different gases with different driver wavelengths, and several interesting features can be observed. First, unlike the perturbative nonlinear optics in which the harmonic generation efficiency decreases rapidly as the harmonic order increases, the HHG spectrum shows a very wide plateau where the harmonic efficiencies are in the same order, and ends sharply at some cutoff photon energy beyond which the harmonic efficiency drops to zero quickly. More specifically, in Fig. 1-1, the harmonic spectra beyond 80 eV

clearly illustrates the plateaus and the cutoffs because it takes stronger fields to generate such high harmonics and drives the process deeper in the strong field regime. Below 30 eV, however, the harmonics from Xe are generated with a lower field strength that is more related to the perturbative regime, so we can see the harmonic efficiencies decrease significantly as the harmonic order increases, similar to the perturbative nonlinear optical processes. Empirically, it is found that the cutoffs can be predicted by the following formula [13]

$$E_{cutoff} \approx I_p + 3U_p, \quad (1.2)$$

where  $E_{cutoff}$  is the cutoff photon energy;  $I_p$  is the ionization potential of the atom;

$$U_p = \frac{e^2 E_0^2}{4m\omega_0^2} \quad (1.3)$$

is the ponderomotive energy, i.e. the average kinetic energy (K.E.) a charged particle of charge  $e$  and mass  $m$  can acquire in a sinusoidal electric field with amplitude  $E_0$  and frequency  $\omega_0$ . This cutoff energy formula will be explained in the discussion of the HHG mechanism. The HHG spectra only show odd harmonics because of the inversion symmetry of the gas media, and HHG only occurs with linear polarized driver pulses and disappears with circular or elliptical polarization [14].

Although the more quantitative physics about HHG will be discussed in Chapter 2, we briefly introduce the elegant semi-classical model of HHG here: the three-step-model (TSM) [15]. The strong electric field of the driver pulse first distorts the atomic potential and induces a potential barrier that can be tunneled through by the electron in the outer most orbital with a binding energy  $I_p$ . After tunneling through the barrier, the electron is ionized and immediately accelerated by the same intense electric field to propagate around the vicinity of the parent atom. Because the electric field is sinusoidal, after about half a laser cycle, some of the ionized electrons will come back to the parent atom with K.E.  $E_k$ .

Depending on the cross-section, the electron has a chance to recombine with the parent atom and emit a photon with energy  $E_k + I_p$ , and this is the semi-classical picture of HHG. Therefore, the TSM consists of the following three steps: ionization, propagation, and recombination, as summarized in Fig. 1-2.

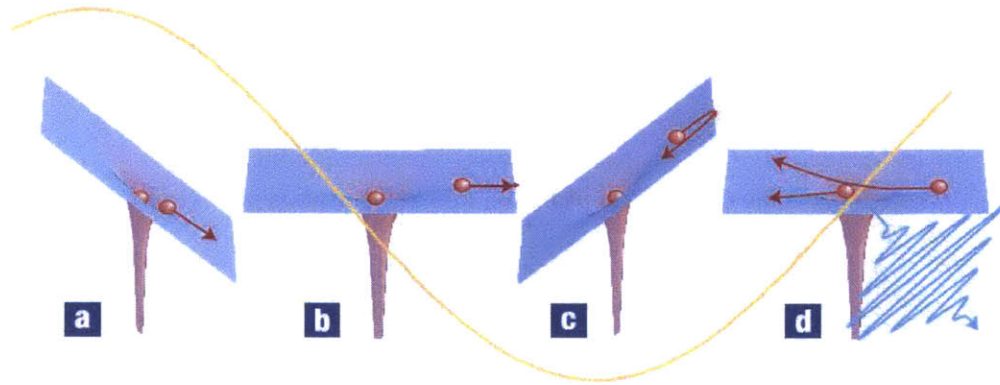


Fig. 1-2 A schematic illustration of the TSM from [16]. (a) An intense femtosecond pulse (yellow curve) extracts an electron wave packet by partially ionizing an atom. (b)-(c) The electron wave packet is pulled away from the atom by the same pulse and then driven back after a fraction of the laser oscillation cycle. (d) When the returning electron recollides with the atom, it has a chance to recombine with the atom and emit a high-energy photon.

The K.E.  $E_k$  has the same order of magnitude as the ponderomotive energy  $U_p$ . If we solve the classical equations of motion of a charged particle in a sinusoidal electric field and impose the following initial and boundary conditions:

1. The initial and the final positions of the particle must be zero, i.e. at the parent atom;
2. The initial velocity of the particle is zero due to the tunneling ionization;

then, we can find that the maximal returning K.E. is  $3.17U_p$ . Therefore, according to the TSM, the maximal photon energy emitted by HHG, which is also the cutoff of the HHG spectrum, should be

$$E_{cutoff} = I_p + 3.17U_p, \quad (1.4)$$



which agrees with the experimental spectra well. If the electric field is not linearly polarized, the ionized electron will go astray and miss the parent atom, so the recombination will not happen. This explains why HHG cannot be observed with circular or elliptical polarization. Beyond the semi-classical description of the TSM, a quantum mechanical description of HHG can be found in Ref. [17], which shows the coherence and the plateau structure of the HHG spectrum.

## **1.2 Applications of High Harmonic Generation**

As shown in Fig. 1-1, the HHG spectrum can cover the entire extreme ultraviolet (EUV) range (10~124 eV), so it is a good candidate for coherent EUV sources. Compared to the large facilities of coherent EUV sources, like the synchrotron or free electron lasers (FEL), the compact size of the HHG experimental apparatus that can fit into a normal size laboratory as a tabletop EUV coherent source is an important advantage. Because of the generation process, the high harmonics inherit the temporal features and the good spatial quality from the driver laser pulses. The ~10-fs pulse duration and the timing jitter that can be well controlled at the driving source provide excellent temporal resolution and stability that are difficult to achieve otherwise. The high spatial quality provides good focusing capability to achieve high brightness [7]. Despite these advantages, the problem of a HHG-based EUV source is the efficiency or the total photon flux. As shown in Fig. 1-1, the efficiency is  $\sim 10^{-4}$  around 50 eV, and  $\sim 10^{-8}$  around 100 eV. The low efficiency limits the applications for such a source. One combinational way to achieve high quality and high flux is to seed other EUV sources with the HHG beam [7]. Therefore, improving the driving source and phase-matching condition is an important issue, particularly for the higher photon energy.

Because of the unprecedented broad and coherent spectrum, HHG can generate very short pulses and has started the experimental attosecond research that explores the electronic dynamics in molecules [18]. The HHG spectrum with separated harmonics actually corresponds to a pulse train with a repetition rate equal to a half-cycle of the driver laser wavelength due to the odd harmonics. The applications of such dense pulse trains are limited, and therefore an isolated attosecond pulse is desired. An isolated attosecond pulse can be generated by driving the HHG process with few-cycle pulses [18] and applying various gating techniques, like polarization gating [19], double optical gating [20], or ionization gating [21]. With these gating methods, isolated attosecond pulses can be generated with less demanding laser systems. So far, isolated attosecond pulses with pulse durations as short as 80 as have been demonstrated [18], and many exciting attosecond experiments have been conducted [22-24]. The current difficulty is the limited pulse energy ( $\sim$ nJ). Generating  $\mu$ J-level isolated attosecond pulses is one of the most important tasks in the attosecond community, which will make the conventional pump-probe technique possible in attosecond experiments [21], and a 1.3- $\mu$ J 500-as isolated pulse has just been reported recently [25].

The HHG process itself also reveals a lot of information about the electronic orbitals in the HHG spectrum that makes HHG spectroscopy a powerful tool to study atomic or molecular structures. A famous example is the observation of the Cooper minimum of Ar [26] and various molecules [27]. The Cooper minimum is a minimum of the photoionization cross-section due to the destructive interference between the bound-state and the continuum-state electron wave functions that causes a dip on the HHG spectrum. The observations of Cooper minima in HHG spectra from various molecules can help theorists develop more accurate models of the molecules. Another interesting HHG

spectroscopy finding is the observation of the giant resonance of Xe HHG spectrum that suggests HHG sometimes can be a multi-electron process rather than single-active-electron process [28]. The orbital structure of diatomic molecules can even be tomographically reconstructed by the HHG spectra [29]. Therefore, HHG not only serves as a novel EUV source for cutting-edge research, the process itself also contains abundant interesting physics to explore.

### **1.3 About This Thesis**

This PhD work is to pursue a better understanding of HHG for the development of coherent EUV or soft X-ray sources, and consists of both theoretical and experimental work. The theoretical work can be further divided into the study of the microscopic and the macroscopic phenomena of HHG respectively. Chapter 2 discusses the microscopic part that considers how to model HHG from one single atom. The wavelength scaling of the single-atom efficiency (SE) is discussed in depth because our experiment on the wavelength scaling of the SE has led to a modification of current models. Chapter 3 deals with the macroscopic part that considers the coherent summation of the high harmonics (HH) emitted from each individual atoms. The impact of plasma defocusing is analyzed and emphasized as a dominant factor influencing HHG efficiency. An efficient algorithm for fully dimensional simulation of HHG is also discussed in Chapter 3. Chapter 4 and Chapter 5 present my experimental works. Chapter 4 shows the experiments done with Ti:sapphire-based laser systems, including the second harmonic of the Ti:sapphire wavelength, and the optical parametric amplification (OPA) system built on it. It studies the wavelength scaling of HHG efficiency and cutoff driven by wavelengths between 400 nm and 800 nm, which has been less explored before. Chapter 5 is devoted to our mid-infrared (IR) optical parametric chirped pulse amplification (OPCPA) system and its HHG results. Although mid-IR driver wavelength can extend the cutoff to the water window

range (284-543 eV) and provide a number of interesting research opportunities, mid-IR ultrashort pulse generation is complicated and is actually an ongoing research topic. Chapter 6 is the conclusion of the thesis.

## Chapter 2

# Microscopic Picture of High Harmonic Generation

In this chapter, the fundamental mechanism of HHG on single atom scale is investigated, and some numerical models are introduced to help understand and analyze HHG. An approach using the Schrödinger equation is considered the most direct way to study atomic physics phenomena, including HHG. Therefore, in Section 2.1, an efficient numerical algorithm to solve the time-dependent Schrödinger equation (TDSE) is developed. Although TDSE provides a fundamental and direct approach to HHG, the computation is time-consuming, and some physics insight becomes obscured behind the numerical results. A simplified model based on the strong-field approximation (SFA), called three-step model (TSM), is thus introduced in Section 2.2 as a convenient substitute of the TDSE approach. As the names suggests, TSM divides the HHG process into three steps and makes the physics more transparent. The conversion efficiency of HHG has always been an important topic in the study of HHG, in particular, how it changes with different driver wavelengths. Section 2.3 discusses the wavelength scaling of HHG single-atom efficiency (SE). Section 2.4 extends the discussion of the wavelength scaling of SE to shorter driver wavelengths for which the SFA is less applicable. A modified TSM is thus proposed to explain the

abnormal wavelength scaling observed in our experiment. The modified TSM also solves a divergence problem due to the conflict between the ionization model and the TSM. Section 2.5 concludes the microscopic physics of HHG discussed in this chapter.

## 2.1 Time-Dependent Schrödinger Equation Simulation

HHG results from the interaction between a molecule and strong laser field, so the process should be studied by TDSE. Solving the Schrödinger equation of a multi-electron system has always been challenging for current computation system, and single-active electron (SAE) approximation is thus a good start for our task: we assume only the outermost electron is involved in the HHG process while the other electrons together with the nucleus form an effective potential  $V(\mathbf{r})$ , where  $\mathbf{r}$  is the position of the outermost electron. Then, the TDSE can be written in atomic units as:

$$i\frac{\partial}{\partial t}|\Psi\rangle = (H_0 + H_I)|\Psi\rangle; \quad (2.1)$$

$$H_0 = -\frac{1}{2}\nabla^2 + V(\mathbf{r}); \quad (2.2)$$

$$H_I = -\mathbf{A}(t) \cdot \mathbf{p}. \quad (2.3)$$

Here  $|\Psi\rangle$  is the wave function of the active electron;  $H_0$  is the molecular Hamiltonian without the laser field;  $H_I$  is the Hamiltonian describing the laser-electron interaction under velocity gauge and dipole approximation;  $\mathbf{A}(t)$  is the vector potential of the driver electric field;  $\mathbf{p}$  is the momentum operator. Since only linear polarized field is considered, and the target atom for HHG is usually spherically symmetric, we can assume  $\mathbf{A}(t) = \hat{\mathbf{z}}A(t)$  and  $V(\mathbf{r})=V(r)$ , and employ the azimuthal symmetry. The Hamiltonians then become:

$$H_0 = -\frac{1}{2}\left[\frac{1}{r^2}\frac{\partial}{\partial r}\left(r^2\frac{\partial}{\partial r}\right) - \frac{\mathbf{L}^2}{r^2}\right] + V(r); \quad (2.4)$$

$$H_I = -A(t)p_z = iA(t)\left(\cos\theta\frac{\partial}{\partial r} - \frac{\sin\theta}{r}\frac{\partial}{\partial\theta}\right). \quad (2.5)$$

$\mathbf{L}^2$  is the angular momentum operator that, when multiplied on a spherical harmonic function  $Y_l^m$ , fulfills the following relation:

$$\mathbf{L}^2 Y_l^m = l(l+1)Y_l^m. \quad (2.6)$$

The wave function can be expanded by the eigen-vectors of  $H_0$  as

$$|\Psi\rangle = \sum_{l=0}^{l_{MAX}} \sum_{n=1}^{n_l} c_{nl}(t) |\phi_{nl}\rangle \exp(-i\omega_{nl}t), \quad (2.5)$$

where

$$H_0 |\phi_{nl}\rangle = \omega_{nl} |\phi_{nl}\rangle; \quad (2.6)$$

$$\langle \mathbf{r} | \phi_{nl} \rangle = r^{-1} u_{nl}(r) Y_l^0(\theta); \quad (2.7)$$

$c_{nl}(t)$  is the time-varying coefficient of each eigen-state component in the expansion of the wave function;  $\omega_{nl}$  is the eigen-value of the eigen-vector  $|\phi_{nl}\rangle$  of  $H_0$ ;  $l_{MAX}$  is the largest angular momentum considered in the computation;  $n_l$  is number of the eigen-states with angular momentum number  $l$  included in the calculation. Because the velocity gauge usually requires a much smaller  $l_{MAX}$  than the length gauge to reach a converged result [30], the velocity gauge for  $H_l$  is employed here. By substituting Eq. (2.7) into Eq. (2.6), we reach the following eigen-function problem for  $u_n(r)$ :

$$\left[ -\frac{1}{2} \frac{\partial^2}{\partial r^2} + \frac{l(l+1)}{2r^2} + V(r) \right] u_{nl}(r) = \omega_{nl} u_{nl}(r), \quad (2.8)$$

where  $n$  distinguishes different eigen-functions with the same angular momentum number  $l$ .  $n$  is similar to the conventional principal quantum number although here it is allowed to be less than  $l$  due to our convention. We also demand that

$$\int_0^\infty u_{nl} u_{n'l'} dr = \delta_{nn'} \delta_{ll'}. \quad (2.9)$$

Next we need to write down the equation of motion, i.e. the differential equations for  $c_{nl}(t)$ . By left-multiplying  $\exp(i\omega_{nl}t) \langle \phi_{nl} |$  to Eq. (2.1), we have

$$i \frac{d}{dt} c_{nl}(t) = \sum_{l'=0}^{l_{MAX}} \sum_{n'=1}^{n_r} c_{n'l'}(t) \exp[-i(\omega_{n'l'} - \omega_{nl})t] \langle \phi_{nl} | H_I | \phi_{n'l'} \rangle. \quad (2.10)$$

These are simply first-order coupled equations with matrix elements  $\langle \phi_{nl} | H_I | \phi_{n'l'} \rangle$ . Because of azimuthal symmetry, the magnetic quantum number is always 0, and the spherical harmonics  $Y_l^0$  become Legendre polynomials with a constant pre-factor. With the help of the recursive relations and the orthogonality of Legendre polynomials we can derive the following expression for the matrix elements in Eq. (2.10):

$$\langle \phi_{nl} | H_I | \phi_{n'l'} \rangle = iA(t) \mathbf{D}_{nl,n'l'}, \quad (2.11)$$

where

$$\mathbf{D}_{nl,n'l'} = C_{ll'} \left[ l \delta_{l(l'+1)} \int_0^\infty \left( u_{nl} \frac{d}{dr} u_{n'l'} - l u_{nl} \frac{u_{n'l'}}{r} \right) dr + l' \delta_{l(l'-1)} \int_0^\infty \left( u_{nl} \frac{d}{dr} u_{n'l'} + l' u_{nl} \frac{u_{n'l'}}{r} \right) dr \right] \quad (2.12)$$

and

$$C_{ll'} = \frac{1}{\sqrt{(2l+1)(2l'+1)}} \quad (2.13)$$

are independent of  $A(t)$ . Then,

$$\frac{d}{dt} c_{nl}(t) = \sum_{l'=-l+1}^{n_r} \sum_{n'=-1}^{n_r} A(t) \mathbf{D}_{nl,n'l'} \exp[-i(\omega_{n'l'} - \omega_{nl})t] c_{n'l'}(t). \quad (2.14)$$

Eq. (2.14) can be solved by the Runge-Kutta method. The eigen-states  $u_{nl}$  will not be called during the computation, which is therefore efficient for both memory and speed.

An absorptive boundary must be implemented at some large radius to account for the ionization effect that leads to a fraction of the wave function leaking away to infinity. Since the Schrödinger equation preserves the norm of the wave function, an artificial boundary absorber should be implemented. In the TDSE simulation presented here, a boundary absorber in the following form



$$F(r) = \left[ 1 + \exp\left(\frac{r - \alpha R}{\beta R}\right) \right]^{-1} \quad (2.15)$$

is employed.  $R$  is the boundary of the radial coordinate, and  $\alpha$  ( $<1$ ) and  $\beta$  are parameters to adjust for correct absorbing (or ionizing) behavior without affecting the wave function near the nucleus. At the end of every computation loop calculating Eq. (2.14), the computed wave function is multiplied by Eq. (2.15). Although this step seems involved with the detail structure of the wave function, we can use the eigen-states  $u_{nl}$  and the boundary absorber to construct one single matrix that maps the coefficients  $c_{nl}$  to the corresponding wave function, puts on the boundary absorber, and then converts it back to a new set of coefficient  $c'_{nl}$ . The dimension of this matrix is given by the number of  $c_{nl}$ 's considered, and no eigen-state  $u_{nl}$  is needed during the calculation of Eq. (2.14). Fig. 2-1 (a) shows the boundary absorber used for Ar HHG simulation and the ground state wave function of Ar. The SAE potential is obtained from Ref. [31]. Fig. 2-1 (b) shows the decay of ground state due to ionization.

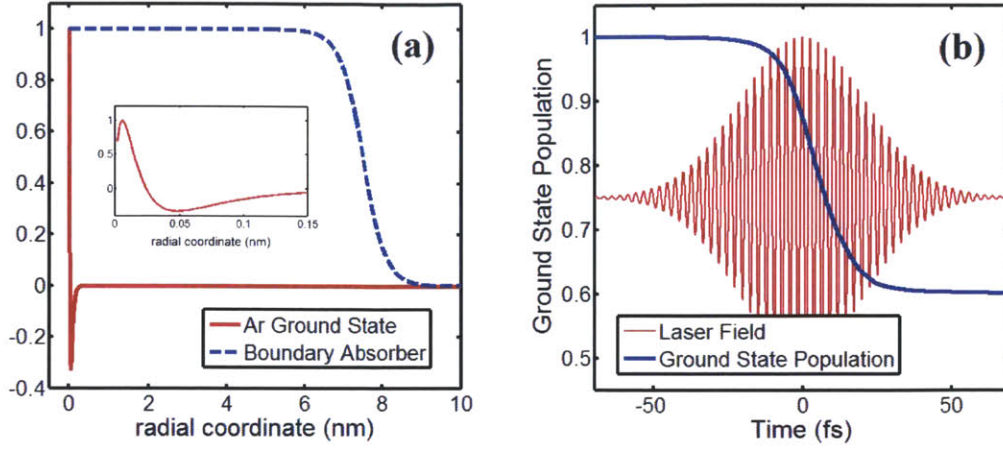


Fig. 2-1 (a) The boundary absorber (blue dashed) to account for ionization effects. Referring to Eq. (2.15),  $R = 10$  nm,  $\alpha = 0.75$ , and  $\beta = 0.03$ . The flat part of the absorber has to be broad enough to cover the vicinity of the atom whose size is determined by the ground state wave function (red solid). The inset shows a closer look of the radial wave function of the 3p electron of Ar ground state. (b) The ground state population calculated by the TDSE simulation (blue). The electric field of the driver pulse (red) has a central wavelength of 800 nm, a peak intensity of  $2.7 \times 10^{14}$  W/cm<sup>2</sup> and pulse duration of 35 fs at the full-width at half-maximum (FWHM) of the intensity.  $l_{MAX} = 30$ .

After calculating all  $c_n(t)$ , we have all of the information about  $|\Psi\rangle$  and can calculate the instantaneous dipole moment by

$$d(t) = \langle \Psi | r \cos \theta | \Psi \rangle. \quad (2.16)$$

Again, with the help of the recursive relations and the orthogonality of Legendre polynomials, we can reach the following expression for the instantaneous dipole moment:

$$d(t) = \sum_{l=0}^{l_{MAX}-1} \sum_{n,n'} \mathbf{Z}_{nn'}^l \operatorname{Re} [c_{n'(l+1)}^* c_{nl}], \quad (2.17)$$

where

$$\mathbf{Z}_{nn'}^l = \frac{2l+2}{\sqrt{(2l+1)(2l+3)}} \int_0^\infty r u_{nl} u_{n'(l+1)} dr. \quad (2.18)$$

Then, the HHG spectrum can be derived from  $d(t)$ . Fig. 2-2 (a) and (b) show the HHG spectra calculated with a flattop pulse and a Gaussian pulse respectively.

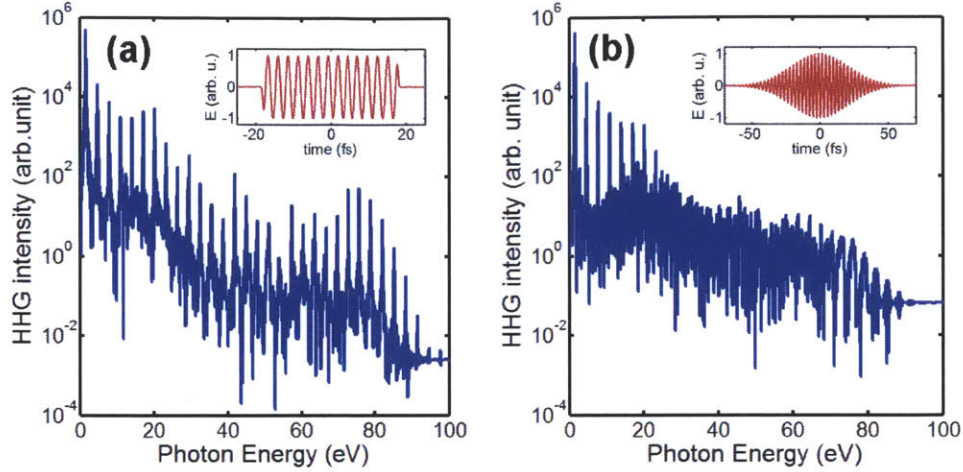


Fig. 2-2 HHG spectra of Ar calculated by TDSE with (a) flattop and (b) Gaussian driver pulses, as shown in the inlets respectively. For both of the driver pulses, the central wavelengths are 800 nm, the FWHM pulse durations are 35 fs, and the peak intensities are  $2.7 \times 10^{14}$  W/cm<sup>2</sup>.

The recipe for the numerical simulation of the TDSE can be summarized below:

1. Find a suitable SAE potential  $V(r)$  by searching literature or by developing a new model.
2. Solve the eigen-problem Eq. (2.8) for  $l = 0, 1, 2, \dots, l_{MAX}$  for the eigen-vectors  $u_n(r)$  and the eigen-values  $\omega_{nl}$ .
3. Calculate matrix elements  $\mathbf{D}_{nl,n'l'}$  with Eq. (2.12) and Eq. (2.13).
4. Construct a matrix that performs the boundary absorption.
5. Calculate matrix elements  $\mathbf{Z}_{mm}^l$  with Eq. (2.18).
6. Solve Eq. (2.14) iteratively. At each step of iteration, apply the boundary absorber matrix and calculate the instantaneous dipole with  $\mathbf{Z}_{mm}^l$ .
7. Calculate the emitted electric field from the dipole.

In step 2, one can build a very large database of the interested gas with very large  $l_{MAX}$  and very large  $n$  (i.e. very large  $\omega_{nl}$ ) that can be reused for different simulation tasks for the same gas species in the future. In step 3-5, we only select moderate  $l_{MAX}$  and  $n$  (i.e. an upper bound of actual  $\omega_{nl}$ ) to build these matrices. With appropriate choices of the parameters,

the matrices constructed in step 3-5 can be used for driver pulses with different parameters, and this computation can be very efficient. It provides a first-principle approach for comparison with other theoretical or numerical approaches and experimental results in the following sections.

## 2.2 The Three-Step Model

Although the first-principle calculation by TDSE is appealing, its computation takes a significant amount of time. Meanwhile, the approximated SAE potential is sometimes difficult to acquire and may affect the accuracy of the solution of the TDSE. In this section, we introduce an analytic formalism under the strong-field approximation (SFA) first formulated by Ref. [17] and then improved by Ref. [32-33]. SFA assumes that once an electron is ionized, it only sees the laser field, and the influence from the nucleus is negligible. This assumption is good for electrons that can acquire a lot of kinetic energy (K.E.) from the laser field and are hardly scattered by the nucleus. Again, we write down the Schrödinger equation, but in the length gauge this time for its transparent physics meaning:

$$i \frac{\partial}{\partial t} |\Psi\rangle = (H_0 + H_I) |\Psi\rangle, \quad (2.19)$$

with

$$H_0 = -\frac{1}{2} \nabla^2 + V(\mathbf{r}); \quad (2.20)$$

$$H_I = -\mathbf{r} \cdot \mathbf{E} = -xE(t). \quad (2.21)$$

The general solution of Eq. (2.19) can be written as

$$\begin{aligned} |\Psi(t)\rangle = & -i \int_0^t dt' \exp\left[-i \int_{t'}^t H(t'') dt''\right] H_I(t') \exp\left[-i \int_0^{t'} H_0(t'') dt''\right] |g\rangle \\ & + \exp\left[-i \int_0^t H_0(t'') dt''\right] |g\rangle. \end{aligned} \quad (2.22)$$

$|g\rangle$  is the initial ground state that satisfies

$$H_0 |g\rangle = -I_p |g\rangle, \quad (2.23)$$

and

$$\exp\left[-i\int_0^t H_0(t') dt'\right] |g\rangle = \exp(iI_p t) |g\rangle. \quad (2.24)$$

$|g\rangle$  is assumed as the only bound state involved in the HHG process (therefore, SAE is assumed implicitly). The amplitude of  $|\Psi(t)\rangle$  projected onto any continuum state  $|\mathbf{v}\rangle$  can be expressed as

$$a_{\mathbf{v}}(t) = \langle \mathbf{v} | \Psi(t) \rangle = -i \int_0^t dt' \langle \mathbf{v} | \exp\left[-i\int_{t'}^t H(t'') dt''\right] H_I(t') \exp\left[-i\int_0^{t'} H_0(t'') dt''\right] |g\rangle. \quad (2.25)$$

So far, Eq. (2.25) is exact, although it is not very useful because we have not and will not show how to calculate the operation of the complete Hamiltonian  $H$  on the wave functions. Here comes the SFA, which assumes that the continuum state is simply a plane wave state with a time-varying wave-vector  $\mathbf{v}$ .  $|\mathbf{v}\rangle$  completely ignores the atomic potential  $V(\mathbf{r})$  and is not scattered. With the SFA, the continuum states are simple and known as the Volkov states [34], which satisfy

$$\langle \mathbf{v} | \exp\left[-i\int_{t'}^t H(t'') dt''\right] = \exp\left[-i\int_{t'}^t \frac{1}{2} (\mathbf{v} + \mathbf{A}(t) - \mathbf{A}(t''))^2 dt''\right] \langle \mathbf{v} + \mathbf{A}(t) - \mathbf{A}(t') |. \quad (2.26)$$

If we define the canonical momentum as

$$\mathbf{p} = \mathbf{v}(t) + \mathbf{A}(t), \quad (2.27)$$

which is in fact independent of  $t$ , then we have

$$a_{\mathbf{p}}(t) = -i \int_0^t dt' \langle \mathbf{p} - \mathbf{A}(t') | H_I(t') |g\rangle \exp\left\{-i\int_{t'}^t dt'' \left[ (\mathbf{p} - \mathbf{A}(t''))^2 / 2 \right] + iI_p t'\right\}. \quad (2.28)$$

HHG results from a transition from one continuum state to the ground state, and the corresponding dipole moment is

$$d(t) = \int d^3 \mathbf{p} a_{\mathbf{p}}(t) e^{-i t \cdot \mathbf{p}} \langle g | x | \mathbf{p} - \mathbf{A}(t) \rangle + c.c. \quad (2.29)$$

Since the continuum components are assumed much smaller than the ground state, here we only consider the continuum-ground state transition and neglect the depletion of the ground state. By substituting Eq. (2.28) into Eq. (2.29), we have

$$d(t) = i \int d^3 \mathbf{p} \int_0^t dt' E(t') \langle \mathbf{p} - \mathbf{A}(t') | x | g \rangle \langle g | x | \mathbf{p} - \mathbf{A}(t) \rangle \exp[-iS(\mathbf{p}, t, t')] + c.c., \quad (2.30)$$

where

$$S(\mathbf{p}, t, t') = \int_{t'}^t \frac{1}{2} (\mathbf{p} - \mathbf{A}(t''))^2 dt'' + I_p(t - t'). \quad (2.31)$$

Eq. (2.30) says that the dipole moment at time  $t$  is a coherent summation of all possible trajectories that transits at some moment  $t'$  from the ground state to a continuum state indexed by a canonical momentum  $\mathbf{p}$ .

Eq. (2.30) along with Eq. (2.31) is the integral solution of the TDSE under SFA, and can be used for practical calculation given the dipole matrix element of the ground-continuum transition  $\langle \mathbf{p} - \mathbf{A}(t') | x | g \rangle$ . However, the fast-oscillating nature of  $\exp[-iS(\mathbf{p}, t, t')]$  in Eq. (2.30) allows us to apply saddle point analysis to further simplify the integral of Eq. (2.30) and acquire more physics insight from it [17]. The integral is mostly determined by the small region around the saddle point where the first derivatives of  $S(\mathbf{p}, t, t')$  with respect to  $\mathbf{p}$  and  $t'$  both vanish such that the integral can build up coherently without suffering the fast oscillation of  $\exp[-iS(\mathbf{p}, t, t')]$ . The saddle point is determined by

$$\nabla_{\mathbf{p}} S(\mathbf{p}, t, t') \Big|_{\mathbf{p}=\mathbf{p}_s, t'=t'_s} = \int_{t'_s}^t (\mathbf{p}_s - \mathbf{A}(t'')) dt'' = 0; \quad (2.32)$$

$$\frac{\partial}{\partial t'} S(\mathbf{p}, t, t') \Big|_{\mathbf{p}=\mathbf{p}_s, t'=t'_s} = -\frac{1}{2} (\mathbf{p}_s - \mathbf{A}(t'_s))^2 - I_p = 0. \quad (2.33)$$

Because of the sinusoidal behavior of the driver field  $\mathbf{A}(t)$ , Eq. (2.32) and Eq. (2.33) have more than one saddle point solution  $(t'_s, \mathbf{p}_s)$ . The saddle point analysis shows that the instantaneous dipole moment at time  $t$  is determined by the electron that is excited at some specific ionization times  $t'_s$  to the corresponding continuum states with canonical momentum  $\mathbf{p}_s$ . Since  $(\mathbf{p}_s - \mathbf{A}(t''))$  is the instantaneous velocity of the ionized electron at time  $t''$ , Eq. (2.32) simply states that only the electron trajectory that comes back to the origin (i.e. the parent atom) contributes to the integral of Eq. (2.30) and induces HHG. This is consistent with the physical picture of TSM introduced in Chapter 1. Eq. (2.33) states that at the ionization time  $t'_s$ , the initial K.E. of the electron is  $-I_p$ , and therefore the velocity is a pure imaginary number  $i\sqrt{2I_p}$ . The negative K.E. is due to the quantum tunneling under the potential barrier, as illustrated in Fig. 2-3 (a). For small  $I_p$ ,

$$t'_s \approx t'_{s0} + i\sqrt{2I_p}/E(t'_{s0}), \quad (2.34)$$

where  $t'_{s0}$  is a real number and is the solution of Eq. (2.33) when  $I_p = 0$ .  $\text{Im}(t'_s)$  can be regarded as the time the electron spends under the potential barrier, during which the electric field decelerates the imaginary velocity of the electron to zero. Then, the electron tunnels out from the barrier with zero velocity at the moment of  $\text{Re}(t')$ . The physical interpretation of the complex  $t'$  also applies to larger  $I_p$ .

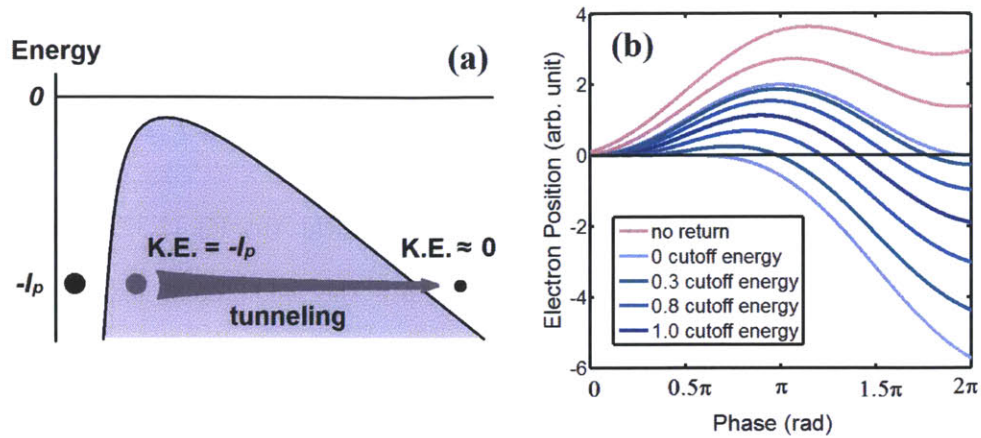


Fig. 2-3 (a) Illustration of tunneling ionization. (b) Electron trajectories in a sinusoidal electric field with zero initial velocity and zero initial position. The horizontal axis shows the phase of the electric field whose peak locates at phase 0 or  $\pi$  (cosine pulse). The trajectories start with phases between 0 and  $-\pi/2$  never return to the origin (pink). The other trajectories start with phases between 0 and  $\pi/2$  return to the origin at different times with different K.E.. The highest returning K.E. is the cutoff energy.

An interesting and important feature of HHG is the existence of the long and short trajectories of electrons. Fig. 2-3 (b) shows the trajectories of free electrons starting from the origin with zero initial velocity in a sinusoidal electric field whose phase is shown as the horizontal axis. The cutoff energy, which is the maximum K.E. the electron may have at the moment of recombination at the origin, is 3.17 times the ponderomotive energy. Fig. 2-3(b) shows that for any recombining K.E. lower than the cutoff energy, there are always two trajectories: the trajectory having earlier ionization time but later recombination time is called long trajectory while the other is called short trajectory. For small  $I_p$ , the long trajectories ionize at phases between 0 and 0.31 rad and recombine at phases between  $2\pi$  and 4.4 rad. The short trajectories ionize at phases between 0.31 and  $\pi/2$  rad and recombine at phases between 4.4 and  $\pi/2$ . The most energetic trajectory, i.e. the cutoff, ionizes at phase 0.31 and recombines at phase 4.4 rad. The lowest K.E. at recombination is 0 for both trajectories.



By employing the saddle point analysis and the Taylor expansion around zero  $I_p$ , a simple form of the instantaneous dipole  $x(t)$  can be derived [32,33]:

$$x(t) = \frac{(2I_p)^{1/4}}{\sqrt{i\pi}} \sum_n \frac{\sqrt{w(E(t_{b,n}))}}{E(t_{b,n})[(t-t_{b,n})/(2\pi)]^{3/2}} a_{rec} \exp[-iS(p, t_{b,n}, t)], \quad (2.35)$$

where  $I_p$  is the ionization potential;  $w$  is the ionization rate that is usually calculated by the ADK formula [35,36];  $E$  is the driver electric field;  $a_{rec} \equiv \langle g|x|\mathbf{p}-\mathbf{A}(t)\rangle$  is the recombination amplitude;  $S$  is the action of the electron as a function of the canonical momentum  $p$ , the ionization time  $t_{b,n}$ , and the recombination time  $t$  that satisfy the saddle point equations. Because there are usually multiple trajectories that start from different ionization times but return at the same recombination time, we use a subscript  $n$  to distinguish these trajectories. The final dipole is a coherent sum of all of these trajectories. The  $(t-t_{b,n})$  term in the denominator of Eq. (2.35) introduces the quantum diffusion effect [17]: the electron wave packet expands during the free propagation in the continuum states. As the electron wave packet expands, the increasing uncertainty of the electron position decreases the probability the electron returns to the exact location of the parent atom to recombine. Because of this quantum diffusion effect, only few trajectories with small propagation time  $(t-t_{b,n})$  are dominant in the summation of Eq. (2.35).

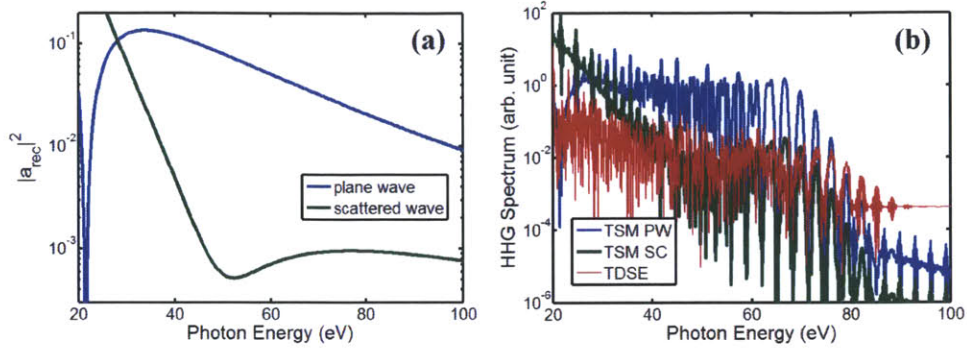


Fig. 2-4 Comparison of the HHG spectra calculated by TDSE and the TSM. (a) Different recombination amplitudes  $a_{rec}$  used in the TSM calculation. In the plane wave model (blue), the continuum states are simply plane waves; in the scattered wave model (green), the continuum states are assumed to be the superposition of plane waves and their scattered waves due to the Coulomb potential. (b) HHG spectra calculated by TSM with plane wave  $a_{rec}$  (blue), TSM with scattered wave  $a_{rec}$  (green), and TDSE (red). The driver pulse has a wavelength of 800 nm, a Gaussian temporal profile with a FWHM of 35 fs, and a peak intensity of  $2.7 \times 10^{14}$  W/cm<sup>2</sup>.

Fig. 2-4 shows the comparison between the TSM and the TDSE calculation result. For TSM, the recombination amplitude  $a_{rec}$  is determined independently. A convenient way is to assume the continuum electron wave function is simply a plane wave, ignoring any scattering from the nucleus. However, this is only accurate for high energy electrons (>500 eV) [37]. An improved version of  $a_{rec}$ , called quantitative rescattering theory [37], considers the scattering due to the nucleus by assuming the continuum wave function is a scattered plane wave, although the scattered electron wave function does not necessarily have a connection to a plane wave. The recombination amplitudes calculated based on the two models are plotted in Fig. 2-4 (a). Fig. 2-4 (b) applies these two recombination amplitudes to the TSM and compares the HHG spectra with that of the TDSE.

### 2.3 Wavelength Scaling of the Single Atom Efficiency

One critical feature of HHG is the strong dependence of the single-atom efficiency (SE) on the driver wavelength  $\lambda$ , which scales as  $\lambda^{-(5-6)}$  [35,36,38-42]. In this section, we will discuss the origin of the scaling law of the SE of HHG. First, we clarify the definition of the HHG efficiency for wavelength scaling. A common definition is the total HHG yield within a certain range of photon energy from driver pulses that differ in wavelengths but have the same number of electric field cycles and the same peak intensity [38-40]. With this definition, a scaling of  $\lambda^{-(5-6)}$  has been reported for IR driver wavelengths [38-40]. However, this definition is not suitable for shorter driver wavelengths because the HHG spectra have narrower bandwidths and sparser harmonics [43]. It is more appropriate to compare the single harmonic yield near some fixed photon energy with the same driver pulse energy and peak intensity [43]. To convert the former wavelength scaling relation to the latter, one should divide the former by a factor of  $\lambda^2$  [44]. One  $\lambda$  factor is due to the higher pulse energy within the driver pulses of a fixed number of cycles and longer wavelengths [45]; the other  $\lambda$  factor is due to the greater number of harmonics within the fixed photon energy range for longer driver wavelengths. The differences between the two definitions are summarized in Fig. 2-5. Here we have assumed similar efficiencies for the harmonics within the considered photon energy range, and this is usually true for the plateau harmonics. Therefore, the wavelength scaling of the SE found in previous works should be restated as  $\lambda^{-(7-8)}$  for single harmonic efficiency with a fixed driver pulse energy.

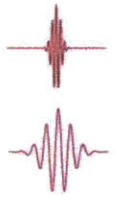
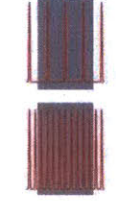

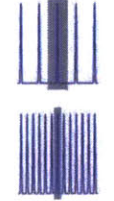
| Driver Pulse Constraint  | Spectral Range   | Wavelength Scaling Law | Driver Pulse Constraint   | Spectral Range   | Wavelength Scaling Law |
|--|--|------------------------|---|--|------------------------|
| Fixed Cycle<br> | Fixed Range<br> | $\lambda^{-(5-6)}$     | Fixed Duration<br> | Single Harmonic<br> | $\lambda^{-(7-8)}$     |

Fig. 2-5 Differences between two definitions for the HHG SE. The left panel (red) compares the total yield within a fixed range of photon energy from driver pulses with the same number of cycles and the same peak intensity, and a scaling law of  $\lambda^{-(5-6)}$  has been reported [35,36,38-42]. The right panel (blue) compares the yield of one single harmonic with the same or similar photon energy from driver pulses with the same pulse duration and the same peak intensity, and the  $\lambda^{-(5-6)}$  scaling law should be modified to  $\lambda^{-(7-8)}$ .

The physics behind the wavelength scaling law is explained below. If we consider driver pulses with different wavelengths but the same pulse duration and the same peak intensity, Eq. (2.35) shows that the intensity of the dipole strength in the time domain scales as  $\lambda^{-3}$  due to the quantum diffusion effect. Therefore, the total yield of all of the harmonics should scale as  $\lambda^{-3}$  if the recombination amplitudes don't vary too much within the photon energy range. Next, the longer driver wavelength has a higher harmonic density (proportional to  $\lambda^{-1}$ ) and a broader HHG bandwidth proportional to  $\lambda^2$  due to the cutoff scaling, so the total harmonic number is proportional to  $\lambda^3$ , and the energy carried by each harmonic peak has a  $\lambda^{-3}$ -dependence according to Parseval's theorem. The  $\lambda^{-3}$  scaling of the total yield due to quantum diffusion and the  $\lambda^{-3}$  proportionality due to the increasing of the total harmonic number together give a  $\lambda^{-6}$  scaling and explain the major wavelength scaling dependence of the SE of HHG. The remaining  $\lambda^{-(1-2)}$  dependence is less obvious and requires a closer look at the action function  $S$  in Eq. (2.35).

To understand the general feature of the wavelength scaling, we first rewrite Eq. (2.35)

as

$$x(t) \sim \frac{1}{E(t_b) [(t-t_b)/(2\pi)]^{3/2}} \exp[-iS(p, t_b, t)], \quad (2.36)$$

where only the first return of the trajectory is considered, and the summation and the subscript  $n$  are dropped. Since the photon energy is fixed in the discussion of wavelength scaling,  $a_{rec}$  is constant and ignored. Although the  $\sqrt{w(E(t_{b,n}))}$  plays an important role, we neglect it for the time being and will include it later. The HHG spectrum can be calculated from the Fourier transform of Eq. (2.36) by saddle point approximation:

$$\int x(t) e^{i\omega t} dt \sim \frac{\exp[-iS(p, t_b, t_r)]}{E(t_b) [(t_r - t_b)/(2\pi)]^{3/2}} \left( \frac{\partial^2 S}{\partial t^2} \right)^{-1/2}. \quad (2.37)$$

To illustrate the  $\lambda$ -dependence, one can normalize the time variables with the corresponding phase of the driver field in Eq. (2.37). Specifically,

$$t_b \rightarrow \frac{\phi_b \lambda}{2\pi c}; \quad t_r \rightarrow \frac{\phi_r \lambda}{2\pi c}; \quad E(t_b) \rightarrow E_0 \cos \phi_b, \quad (2.38)$$

where  $c$  is the speed of light in vacuum. After some algebraic manipulation, the action  $S$  given by Eq. (2.31) can be written as

$$S = \frac{e^2}{8\pi^3 \epsilon_0 c^4 \hbar m} I_0 \lambda^3 F(\phi_r, \gamma), \quad (2.39)$$

where

$$F(\phi_r, \gamma) = (\phi_r - \phi_b) \left\{ \gamma^2 - \frac{(\cos \phi_r - \cos \phi_b)^2}{(\phi_r - \phi_b)^2} + \left[ \frac{1}{2} - \frac{\sin(2\phi_r) - \sin(2\phi_b)}{4(\phi_r - \phi_b)} \right] \right\}. \quad (2.40)$$

Note that  $\phi_b$  has an implicit dependence on  $\phi_r$ , so the only independent variables in  $F$  are  $\phi_r$  and  $\gamma$ . However, the second derivative of the action  $S$  with respect to  $t$  (or  $\phi_r$ ) is independent of  $\gamma$  because of the saddle point property (Eq. (2.32) and Eq. (2.33)).

Therefore, the second derivative of  $S$  with respect to  $t$  is

$$\frac{\partial^2 S}{\partial t^2} \sim \lambda \frac{\partial^2 F}{\partial \phi_r^2}, \quad (2.41)$$

The squared magnitude of Eq. (2.37) gives the spectral density induced by one cycle of the laser field, and the final single harmonic yield will be the summation of the squared magnitude of Eq. (2.37) over the total number of cycles ( $\sim \lambda^{-1}$ ) multiplied by the single harmonic bandwidth ( $\sim \lambda^{-1}$ ). If we assume the driver pulse has a flattop envelope and neglect the depletion of the ground state, it is

$$\sum_{\text{cycles}} \left| \int x(t) e^{i\omega t} dt \right|^2 \Delta E \sim \frac{1}{\cos^2(\phi_b) (\phi_r - \phi_b)^3} \left( \frac{\partial^2 F}{\partial \phi_r^2} \right)^{-1} \frac{1}{\lambda^6}. \quad (2.42)$$

The  $\lambda^{-6}$  factor in Eq. (2.42) has been explained in the beginning of this section. The remaining dependence is related to  $\phi_r$  and  $\phi_b$ . Fig. 2-6 (a) shows the ionization phase ( $\phi_b$ ) and the recombining K.E. (in terms of the ponderomotive energy  $U_p$ , which is quadratically proportional to the driver wavelength) versus the recombination phase ( $\phi_r$ ). As  $U_p$  increases with the driver wavelength, the corresponding recombination phase  $\phi_r$  and ionization phase  $\phi_b$  of the long (short) trajectory will increase (decrease) and decrease (increase) respectively if the recombining K.E. is fixed. Therefore, Eq. (2.42) does not scale as  $\lambda^{-6}$  exactly.

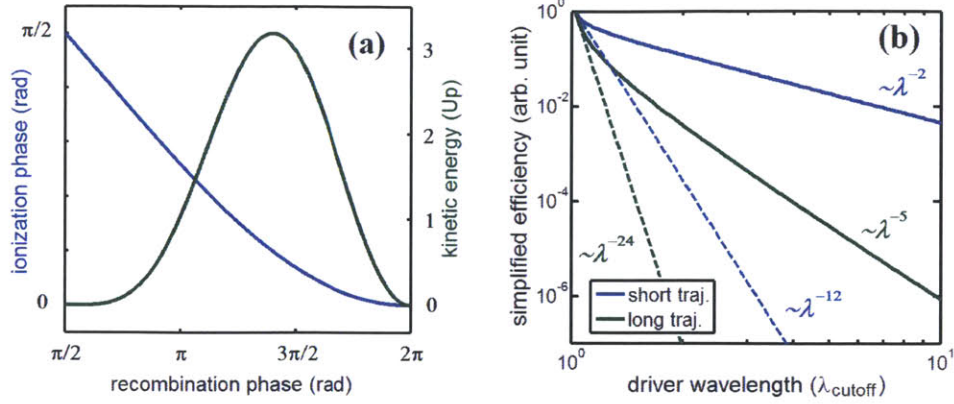


Fig. 2-6 (a) the ionization phase  $\phi_b$  (blue) and the K.E. of the returning electron (green) versus the recombination phase  $\phi_r$ . The K.E. is expressed in terms of the ponderomotive energy ( $U_p$ ) (b) The wavelength scaling of Eq. (2.42) for the long (green) and the short (blue) trajectories without the ionization effect. The dashed lines are tangential to the beginning of the two curves respectively to show the local slopes. The long and the short trajectories asymptotically approach  $\lambda^{-5}$  and  $\lambda^{-2}$  respectively. Note, the actual scaling of the short trajectory will change significantly after the ionization is included.

Fig. 2-6 (b) shows the preliminary wavelength scaling of HHG SE from a flattop driver pulse before including the influence of the ionization effect. The unit of the driver wavelength in Fig. 2-6 (b) is  $\lambda_{\text{cutoff}}$ , which is the shortest wavelength to generate the photon energy of interest at the cutoff. Fig. 2-6 (b) starts from  $1.02\lambda_{\text{cutoff}}$  rather than  $\lambda_{\text{cutoff}}$  because the second order derivative of the action  $S$  is zero at  $\lambda_{\text{cutoff}}$ , and the curves diverge. In fact, saddle point approximation only works for the harmonics at the plateau, and at the cutoff it has to include the third order derivative of  $S$ . Note that, except for the dependence of the ionization effect, expressing the driver wavelength in  $\lambda_{\text{cutoff}}$  makes these scaling curves universal for any driver wavelength range, any driver intensity, and any photon energy as long as the TSM expressed by Eq. (2.35) is applicable. For the long trajectory, the SE shows a sharp scaling near the cutoff and moves asymptotically to  $\lambda^{-5}$ , while the short trajectory moves from a sharp scaling near the cutoff asymptotically to  $\lambda^{-2}$ . These conclusions are not complete until the influence of the ionization is considered. However, they are still helpful because they are the general part of the HHG wavelength scaling. The



actual scaling law can be obtained by simply including the actual ionization condition in this general picture. Moreover, the long trajectory result does not change too much even the ionization is included, as will be shown in Fig. 2-7.

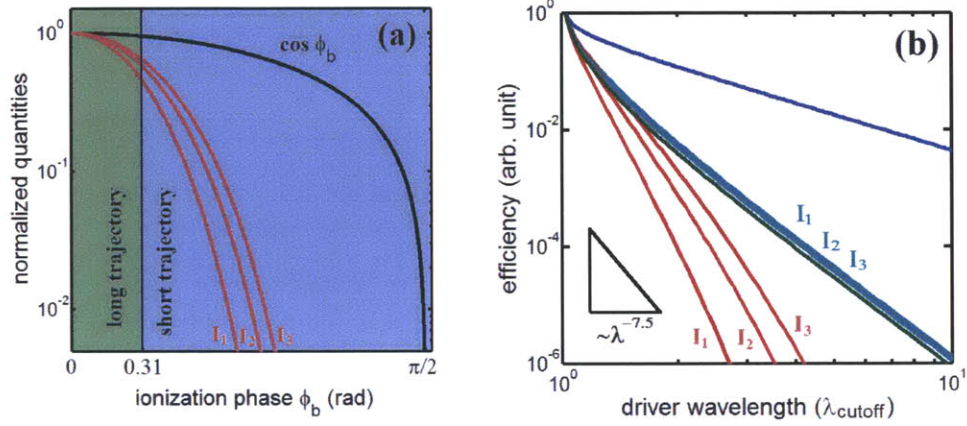


Fig. 2-7 (a) Normalized ADK ionization rate with peak intensities  $I_1=1\times 10^{14}$  W/cm<sup>2</sup>,  $I_2=2\times 10^{14}$  W/cm<sup>2</sup>, and  $I_3=3\times 10^{14}$  W/cm<sup>2</sup> in Ar ( $I_p=15.76$  eV) for a quarter cycle of the driver field. The black curve shows the driver field that is a cosine function. The red curves show the instantaneous ionization rate calculated by the ADK formula at the labeled intensities. Trajectories ionized before and after 0.31 rad become the long and the short trajectories respectively. (b) The wavelength scaling. The blue and the green curves are the same as those in Fig. 2-6 (b) without the ionization effect. The red curves show the scaling of the short trajectories with ionization effect at intensities  $I_1$ ,  $I_2$ , and  $I_3$ . The cyan curves show the long trajectories at  $I_1$ ,  $I_2$ , and  $I_3$ , although they are too close to resolve. The right triangle at the lower left corner shows an example slope of  $\lambda^{-7.5}$ .

Fig. 2-7 (a) shows how the intra-cycle ionization rate varies with the driver electric field calculated by the ADK model [46] in Ar ( $I_p=15.76$  eV) with intensities between  $(1-3)\times 10^{14}$  W/cm<sup>2</sup>, which is typical in HHG. Because ionization is a highly nonlinear process, the ionization rate is very sensitive to the electric field strength and changes much faster than the cosine form of the electric field. Therefore, one can expect that as the ionization phase  $\phi_b$  changes in Eq. (2.42), the efficiency should change as well. In particular, since the ionization rate changes more dramatically at larger ionization phase  $\phi_b$ , the short trajectory is more sensitive to the ionization rate variation than the long trajectory.



Fig. 2-7 (b) confirms this point. The wavelength scaling of the short trajectories becomes much more dramatic while the wavelength scaling of the long trajectory does not change too much after the ionization effect is included. In most literatures, the wavelength scaling is studied with driver wavelengths between 0.8  $\mu\text{m}$  and 2  $\mu\text{m}$  [35,36,38-42], or between 0.4  $\mu\text{m}$  and 0.8  $\mu\text{m}$  [5,9,47], and the interested photon energy is in the mid-high plateau. If the driver wavelength varies by a factor of 2-3 near the cutoff in Fig. 2-7 (b), it is not surprising to conclude a wavelength scaling law of  $\lambda^{-(7-8)}$ .

#### 2.4 Multiphoton and Non-adiabatic Effects

In this section we consider modification of the TSM driven by shorter wavelengths with intermediate Keldysh parameter  $\gamma \approx 1$ . The Keldysh parameter defined as [48]

$$\gamma \equiv \sqrt{I_p / 2U_p}, \quad (2.43)$$

distinguishes strong field physics processes between the tunneling ( $\gamma \ll 1$ ) and the multiphoton ( $\gamma \gg 1$ ) regimes. Eq. (2.35) is derived with Taylor expansion around  $\gamma = 0$ , and the lowest order term of  $\gamma$  (which is purely imaginary) in the expansion of the action  $S$  results in ionization [32,33]. This ionization can be related to the ADK formula for a more accurate description. To study the wavelength scaling of SE using short-wavelength drivers, the TSM needs applying carefully because the semi-classical picture in the conventional TSM assumes that  $\gamma$  is much less than one and neglects its influence. However,  $\gamma$  is rarely much less than one in many HHG experiments. When  $\gamma$  is considered, it has been shown that the ionization time at which an electron exits the atomic potential barrier is slightly advanced from the semi-classical model [49]. Since the ionization time can influence the HHG efficiency through quantum diffusion [17], this can lead to different HHG characteristics.

In general, the solution of the saddle point equations Eq. (2.32) and Eq. (2.33) is complex and is denoted as  $\tilde{t}_{b,n}$  and  $\tilde{p}$  [17]. The physical intuition behind  $\text{Im}(\tilde{t}_{b,n})$  is the tunneling time the electron experiences under the atomic potential barrier, and  $\text{Re}(\tilde{t}_{b,n})$  is the real ionization time at which the electron exits the barrier [50]. Without doing Taylor expansion, the exact action  $S$  is calculated with the complex saddle point, and  $\text{Im}(S)$  can be related to the non-adiabatic (NA) ionization model  $w_{NA}$  [51] rather than the quasi-static ADK formula for more accurate ionization rate [52,53]. The NA ionization model also takes finite  $\gamma$  into account in the saddle point calculation of the ionization moment and shows significant corrections to the intra cycle ionization of the ADK formula [51]. In addition to the modification of the action-related terms, we consistently substitute real ionization time  $t_{b,n}$  by the complex ionization time (CIT)  $\tilde{t}_{b,n}$  and reach the following form of the modified TSM (note,  $\text{Im}(S)$  has been separated from the exponential term and related to the ionization formula  $w_{NA}$  [54], so only  $\text{Re}(S)$  appears explicitly):

$$x(t_r) = \frac{(2I_p)^{1/4}}{\sqrt{i\pi}} \sum_n \frac{g(\text{Re}\tilde{t}_{b,n})g(t_r)\sqrt{w_{NA}[E(\text{Re}\tilde{t}_{b,n})]}}{E(\tilde{t}_{b,n})[(t_r - \tilde{t}_{b,n})/(2\pi)]^{3/2}} a_{rec} \exp[-i\text{Re}S(\tilde{p}, \tilde{t}_{b,n}, t_r)], \quad (2.44)$$

where  $g(t)$  is the ground state amplitude. Eq. (2.44) is the modified version of Eq. (2.35) by including the influences from the NA ionization and the finite Keldysh parameter.

With the CIT, we expect the additional time spent under the barrier to influence the wavelength scaling of the SE. To the first order approximation of  $\gamma$ , we can write the electron traveling time as [43]:

$$\phi_r - \tilde{\phi}_b \approx \phi_r - \phi_b - \frac{i\gamma}{\cos(\phi_b)}. \quad (2.45)$$

For a short driver wavelength,  $\gamma$  is large, and the imaginary part of Eq. (2.45) can thus change the wavelength scaling. Fig. 2-8 (a) shows the magnitude of the exact traveling

time  $|\phi_r - \tilde{\phi}_b|$  as a function of the recombination phase  $\phi_r$ . When the driver wavelength is shorter and  $\gamma$  is higher, the electron has to travel for a longer cycle (i.e. larger phase difference  $|\phi_r - \tilde{\phi}_b|$ ) relative to the driver pulse before recombining with the parent atom, which means the traveling time is not as short as the case ignoring  $\gamma$ . Since the HHG efficiency favors a shorter traveling time, the increasing  $\gamma$  makes the wavelength scaling less dramatic when the HHG process moves from the tunneling regime to the multiphoton regime [43]. This effect is particularly important for the short trajectories because the traveling time is more sensitive to  $\gamma$  with a recombination time near  $\pi/2$ .

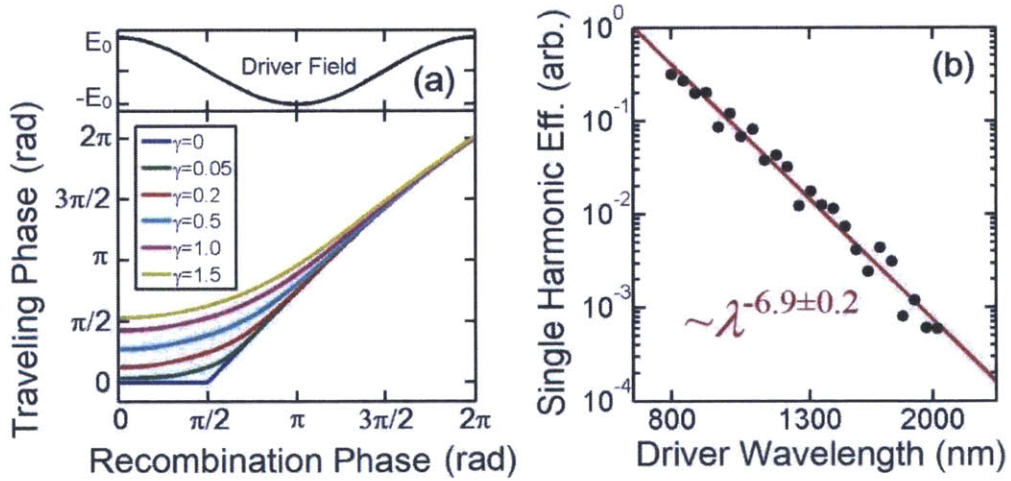


Fig. 2-8 (a) The magnitude of the traveling phase  $|\phi_r - \tilde{\phi}_b|$  as a function of the recombination phase  $\phi_r$  for several different Keldysh parameter  $\gamma$ . (b) The wavelength scaling of Ar SE near 32 eV calculated by Eq. (2.44) with IR driver wavelengths. The peak intensity of the simulated driver pulses is  $2.7 \times 10^{14}$  W/cm<sup>2</sup>, and the pulse duration is 35 fs.

We calculate the wavelength scaling of HHG SE with the modified TSM. Fig. 2-8 (b) shows the single harmonic efficiency with IR driver wavelengths ( $\gamma = 0.3-0.7$ ), and the result roughly agrees with the  $\lambda^{-(7-8)}$  scaling relation. With shorter driver wavelengths, Fig. 2-9 compares the experiment data [43] with the conventional TSM, the modified TSM, and

the time-dependent Schrödinger equation (TDSE) calculations. The detail of the experiment will be presented in Section 4.3. In the conventional TSM, the ionization time is real, and the ionization rate is calculated by the ADK formula; in the modified TSM, the CIT and the NA ionization formula are employed. In Fig. 2-9 (b), both short and long trajectories of the conventional TSM show more dramatic wavelength scaling than the experimental result. In contrast, the short trajectory of the modified TSM in Fig. 2-9 (c) agrees well with the experiment by showing a scaling of  $\lambda^{-4.5}$ . The long trajectory of the modified TSM has a similar scaling as the conventional TSM because the long trajectory is less sensitive to  $\gamma$ . The sum of the two trajectories has a scaling of  $\lambda^{-4.8}$ , so the short trajectories are more dominant. To further confirm this scaling relation, Fig. 2-9 (d) shows the numerical result from the TDSE by the numerical method discussed in Section 2.1 with a model potential from Ref. [31]. The wavelength scaling is  $\lambda^{-4.0}$ , also in good agreement with our modified TSM and experimental result.

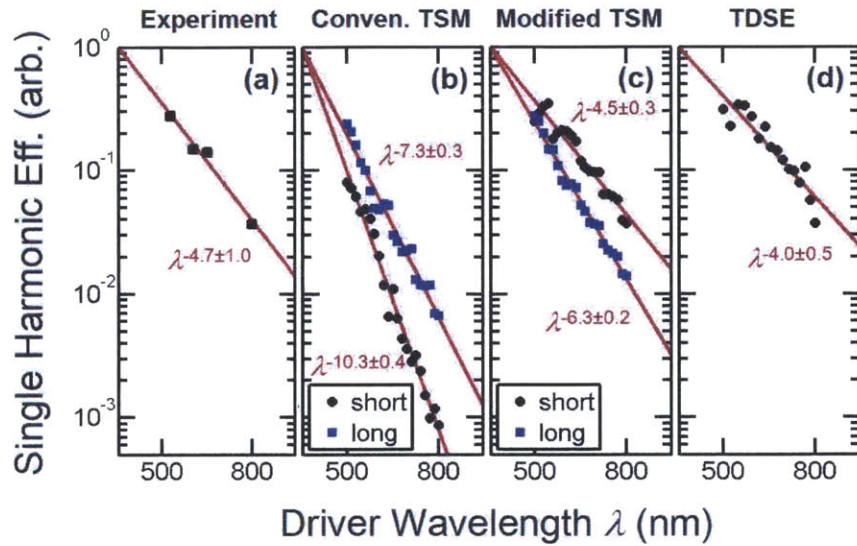


Fig. 2-9 Wavelength scaling of single harmonic efficiency near 32 eV (a) measured by the experiment, and calculated by (b) the conventional TSM, (c) the modified TSM, and (d) the TDSE. In (b)-(d), the peak intensity of the simulated driver pulses is  $2.7 \times 10^{14}$  W/cm<sup>2</sup>, and the pulse duration is 35 fs, same as the experiment parameters. In the TSM calculation, the short (black dot) and long (blue square) trajectories are calculated separately, and the long trajectories are shifted by multiplying by 1.7 and 1.3 in (b) and (c) respectively for comparison. The sums of the two trajectories in (b) and (c) scale with the driver wavelength as  $\lambda^{-7.1 \pm 0.4}$  and  $\lambda^{-4.8 \pm 0.3}$  respectively (not shown).

Including the NA ionization also influences the wavelength scaling in two ways. First, the NA ionization has a higher ionization rate below the peaks of the driver field than the ADK ionization, as shown in Fig. 2-10 (a). This enhances the short trajectory efficiency and makes it more dominant in the wavelength scaling. Second, the more uniform ionization rate close to the  $\pi/2$  phase of the driver field reduces the wavelength scaling of the short trajectories. As the driver wavelength becomes longer, the efficiency of the short trajectory of some fixed photon energy decreases because the corresponding electron is ionized at a phase closer to  $\pi/2$  where the field intensity is weaker [52]. The more uniform NA ionization reduces this effect on the wavelength scaling. With the CIT and the ADK ionization, a wavelength scaling of  $\lambda^{-5.4}$  is obtained, and replacing the ADK by the NA ionization further improves the model and makes it closer to the experimental result.

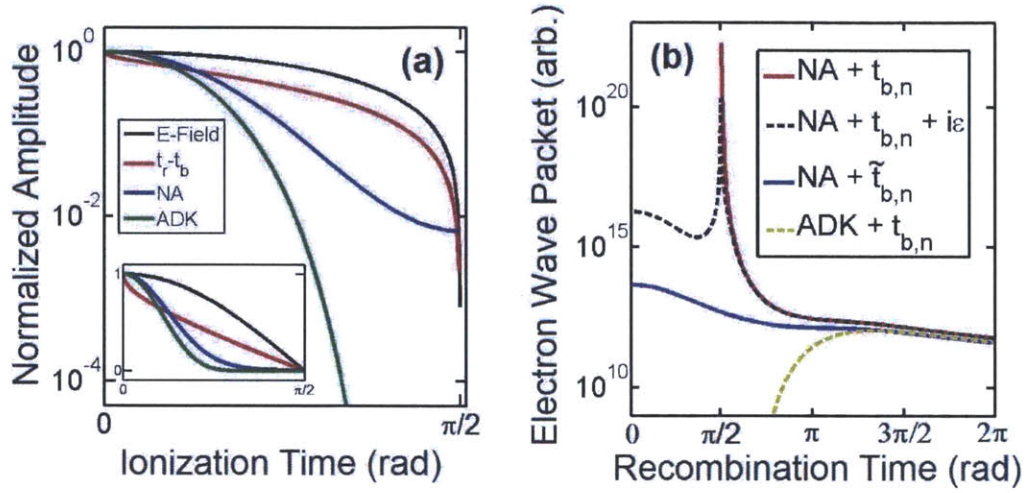


Fig. 2-10 (a) The comparison of the driver electric field (black), the traveling time in the conventional TSM (red), the NA ionization rate (blue), and the ADK ionization rate (green). The horizontal axis shows the phase of the driver field, and the vertical axis shows the normalized values of the four quantities. The inset presents the same plot on a linear scale. (b) The electron wave packet calculated with different ionization models (ADK or NA) and different ionization time formalisms ( $t_{b,n}$  or  $\tilde{t}_{b,n}$ ).

The CIT not only improves the accuracy of the TSM, but avoids the divergence of the TSM due to the replacement of the ADK ionization by the NA ionization. Fig. 2-10 (a) illustrates how the divergence occurs by showing several relevant quantities. As the phase of the driver pulse at the ionization time approaches  $\pi/2$ , the traveling time of the conventional TSM approaches zero, while the NA ionization rate is non-zero due to the contribution from the multiphoton ionization [51], and divergence occurs. This divergence does not exist with the ADK ionization rate because the ADK rate approaches zero at a much faster rate than the traveling time. Fig. 2-10 (b) further illustrates the divergence by showing the electron wave packet that is the squared amplitude of Eq. (2.35) without the recombination amplitude  $a_{rec}$  [28,37]. The divergence occurs for the combination of the NA ionization and the conventional real ionization time  $t_{b,n}$ . When the traveling time is small, a correction factor  $i\epsilon$  in the order of  $I_p^{-1}$  may be added to the traveling time in the



denominator of Eq. (2.35) and Eq. (2.44) [17], which reflects the contribution of the atomic structure to the saddle point integrals. Unless the complex  $\tilde{t}_{b,n}$  is employed, however, the electron wave packet still shows a spike even with the correction factor  $i\varepsilon$ , as shown in Fig. 2-10 (b). Therefore, to apply the more general NA ionization model to the TSM, it is necessary to employ the CIT in the TSM to avoid the divergence.

In conclusion, the wavelength scaling of HHG SE is inspected experimentally and theoretically by visible driver wavelengths with a Keldysh parameter around unity in the transition between the tunneling and the multiphoton ionization regimes. The experimental result shows a less dramatic wavelength scaling than the conventional HHG with IR driver wavelengths and is well explained by our modified TSM that incorporates the NA ionization and the CIT from the saddle point method. For HHG close to the multiphoton regime, the CIT can alter the electron traveling time in the TSM and make the wavelength scaling of the SE less dramatic than HHG driven by longer wavelengths in the tunneling regime. In addition, because the CIT removes the singularity from the traveling time in the conventional TSM, we can replace the quasi-static ADK model by the more general NA ionization model without divergence and obtain a modified TSM that works for a wider range of Keldysh parameters [43].

## 2.5 Conclusion

The fundamental mechanism of HHG is studied in this chapter. We started from the first-principle approach by developing an efficient algorithm to solve the TDSE. The TDSE algorithm separates the simulation work that is independent of the applied electric field from the field-dependent part. Therefore it is more efficient when the simulation has to change the driver pulse frequently, for example, to run a series of simulation for different

driver wavelengths to study the wavelength scaling of the HHG SE, because only the field-dependent part needs to be repeated. Ar with a SAE model potential is solved, and the result correctly shows the ionization behavior and the cutoff of HHG. The first-principle approach of TDSE can provide a good reference for comparison with other theoretical approaches.

TSM is introduced as a convenient substitute to TDSE because the calculation is much simpler and faster. Under the SFA, a solution to the TDSE in an integration form is obtained. Then, the saddle point approximation is applied to the integral solution to further simplify the solution. Finally, a closed-form expression of the dipole moment of HHG is obtained with clear physical meaning of the three steps involved in HHG: ionization, acceleration, and recombination. With this handy expression of HHG dipole moment, we investigate the wavelength scaling of HHG SE to understand the origin of the  $\lambda^{-(5-6)}$  (or  $\lambda^{-(7-8)}$  for single harmonic efficiency in our convention) scaling law. The major contribution to the dramatic wavelength scaling law is from the Parseval theorem due to the increasing numbers of harmonic peaks and the quantum diffusion. The rest dependence of the scaling law is attributed to the electron trajectory, including the action  $S$  and the ionization rate. The long and the short trajectories therefore show quite different wavelength scaling trends.

Last, we try to improve the TSM when the Keldysh parameter is not negligible, and the SFA is not very accurate. Our approach is to include finite Keldysh parameter in the saddle point equations to solve for the complex form of the ionization time. With the CIT, the more general NA ionization model can be incorporated into the TSM to replace the quasi-static ADK ionization model without divergence problem. The modified TSM shows better agreement with the experiment result of the wavelength scaling of HHG SE driven



by visible wavelengths. It also agrees well with the TDSE calculation, which doesn't rely on SFA. Therefore, our modified TSM can work for a wider range of Keldysh parameter, covering both of the tunneling regime and the multiphoton regime.

**THIS PAGE IS INTENTIONALLY LEFT BLANK**

# Chapter 3

## Macroscopic Effects: Phase-Matching and Plasma Defocusing

Because HHG is a coherent process, the phases of the harmonics from different atoms in the medium can significantly affect the final yield of HHG. Therefore, this chapter is devoted to discussing the macroscopic effects of the HHG medium. Section 3.1 discusses the fundamental concept of phase matching in HHG. In addition to the matching between the refractive indices as the conventional nonlinear optical conversion, the Gouy phase and the dipole phase play important roles in the phase-matching of HHG. Because HHG partially ionizes the medium, plasma is induced in the medium and has strong impact on the HHG process. Therefore, Section 3.2 quantitatively analyzes the influence of plasma defocusing on HHG. The major effects include the degradation of the driver pulse intensity and the phase-mismatching. The first two sections in this chapter also lay the foundation of simulating the macroscopic effects of HHG, which is then combined with the TSM presented in last chapter into a complete HHG numerical model, as will be shown in Section 3.3 with several examples. Section 3.4 tries to answer the question: is a shorter medium with higher pressure or a longer medium with lower pressure better, if the product of the length and the pressure is fixed? The answer can be of practical value in choosing

medium geometry. Section 3.5 is the conclusion of the macroscopic effects discussed in this chapter.

### 3.1 Phase-Matching

Because HHG is a coherent process, phase-matching is very important for the efficiency. The matching between the refractive indices of the driver wavelength and the HH is critical, similar to the second or third harmonic generation. Besides, the Gouy phase is also very important due to the very high order harmonic generation [55]. Since HHG generates plasma during the ionization process, the refractive indices should consider the contribution from the plasma dispersion as well, and thus the phase-matching becomes intensity-dependent. Last, the dipole phase that the electron wave function acquires during its propagation plays an important role in the phase-matching, too [55]. The phase-matching of HHG driven by a multi-cycle pulse are mostly determined by the factors mentioned above, and this section will discuss the interplay among them.

The definition of the wave-vector mismatching is the same as the conventional nonlinear optics:

$$\Delta k_q = qk_1 - k_q, \quad (3.1)$$

where  $k_1$  and  $k_q$  are the wave-vectors of the fundamental wavelength (the driver pulse) and the  $q^{\text{th}}$  harmonic respectively. In most cases, the HH and the driver pulse propagate along the same direction, so the wave-vectors can be expressed by scalar values. The wave-vectors can be further decomposed into different components:

$$k_q = \frac{q\omega_1}{c} + \frac{q\omega_1}{c} \frac{P}{P_0} \left[ (1-\eta)(n_q - 1) - \frac{1}{q^2\omega_1^2} \frac{\eta\rho_0 e^2}{2m_e \epsilon_0} \right] + k_q^G, \quad (3.2)$$

where  $\omega_1$  is the angular frequency of the driver field;  $P$  is the pressure of the medium;  $P_0$  is the reference pressure of the medium at which the refractive index at  $q\omega_1$  is  $n_q$ ;  $\eta$  is the

ionization level defined as the fraction of ionized atoms;  $\rho_0$  is the medium density at pressure  $P_0$ ;  $e$  is the elementary charge;  $m_e$  is the mass of electron;  $\epsilon_0$  the permittivity of vacuum;  $k_q^G$  is the wave-vector due to the geometric phase. The pressure  $P$  is assumed to be dilute enough such that  $(n_q-1)$  is much less than one and proportional to  $P$ .

The geometric phase results from the propagation of electromagnetic (EM) waves. The slow-varying envelope approximation and the paraxial approximation are assumed, and the EM wave is expressed as

$$E_q(r, z, t) = A_q(r, z, t) \exp(ik_q z - iq\omega_q t). \quad (3.3)$$

Unless specified, only linearly polarized waves propagating along  $z$ -direction with cylindrical symmetry in the other two spatial dimensions are considered. Then, the propagation equation of Eq. (3.3) is

$$\frac{\partial A_q}{\partial z} = \frac{i}{2k_q} \nabla_r^2 A_q, \quad (3.4)$$

where  $\nabla_r^2 \equiv \nabla^2 - \partial^2 / \partial z^2$  is the transversal Laplacian. During propagation, Eq. (3.4) causes a change of the phase of  $A_q$  whose change rate along the propagation can be calculated by

$$k_q^G \equiv \frac{\partial}{\partial z} \arg(A_q) = |A_q|^{-2} \operatorname{Im} \left( A_q^* \frac{\partial A_q}{\partial z} \right). \quad (3.5)$$

For a Gaussian beam with Rayleigh range  $z_{0q}$ ,  $k_q^G = -z_{0q} / (z^2 + z_{0q}^2)$  on axis. In general, while the envelope of the driver pulse changes its shape during propagation,  $k_q^G$  may have different and more complicated forms.

The dipole phase also plays an important role in HHG phase-matching. The dipole phase is sensitive to the actual trajectory of the electron in the continuum states and changes while the envelope of the driver field varies during propagation. Consider a

trajectory ionizes at time  $t'$ , recombines at time  $t$ , and emits a photon of energy  $\hbar\omega$ . The phase of this photon in atomic unit would be

$$\phi = -\int_{t'}^t dt'' \left\{ \frac{1}{2} [p - A(t'')]^2 + I_p \right\} + \omega t. \quad (3.6)$$

Assume  $A(t) = -A_0 \sin(\omega_1 t)$  for a cosine electric field and  $p = -A_0 \sin(\omega_1 t')$  for a vanishing initial velocity. Because of the saddle point features inherited by the HHG phase, we have

$$\frac{d\phi}{dA_0} = \frac{\partial\phi}{\partial t} \frac{\partial t}{\partial A_0} + \frac{\partial\phi}{\partial t'} \frac{\partial t'}{\partial A_0} + \frac{\partial\phi}{\partial p} \frac{\partial p}{\partial A_0} + \frac{\partial\phi}{\partial A_0} = \frac{\partial\phi}{\partial A_0}. \quad (3.7)$$

After some algebraic manipulation, Eq. (3.7) becomes

$$\frac{d\phi}{dA_0} = \frac{A_0}{\omega_1} \left\{ \frac{1}{2} \omega_1 (t - t') - \frac{1}{4} \sin 2\omega_1 t - \frac{1}{4} \sin 2\omega_1 t' + \sin \omega_1 t' \cos \omega_1 t \right\}. \quad (3.8)$$

An effective wave-vector of the HHG field due to the variation of the envelope of the driver field along propagation can be derived by starting from the ansatz:

$$k^D = \alpha \frac{\partial I}{\partial z}, \quad (3.9)$$

where  $I = \omega_1^2 \epsilon_0 c A_0^2 / 2$  is the intensity of the driver field in SI unit. Then, an expression of  $\alpha_q$  can be found as

$$\alpha = \frac{1}{\omega_1^2 \epsilon_0 c A_0} \frac{\partial\phi}{\partial A_0}. \quad (3.10)$$

We can substitute Eq. (3.8) into Eq. (3.10) and get

$$\alpha = \frac{e^2}{m_e \hbar \epsilon_0 c \omega_1^3} \left\{ \frac{1}{2} (\phi_r - \phi_b) - \frac{1}{4} \sin 2\phi_r - \frac{1}{4} \sin 2\phi_b + \sin \phi_b \cos \phi_r \right\}, \quad (3.11)$$

where  $\hbar$  is the reduced Planck constant. For 800-nm driver wavelength, the  $\alpha$  of short trajectories is between  $(0-1.3) \times 10^{-14}$  cm<sup>2</sup>/W, and the  $\alpha$  of long trajectories is between  $(1.3-2.4) \times 10^{-14}$  cm<sup>2</sup>/W. Longer driver wavelengths are much more sensitive to dipole phase

because  $\alpha$  is proportional to  $\lambda^3$  according to Eq. (3.11). Fig. 3-1 shows  $\alpha$  for 800-nm driver wavelength versus the recombining K.E. of electron.

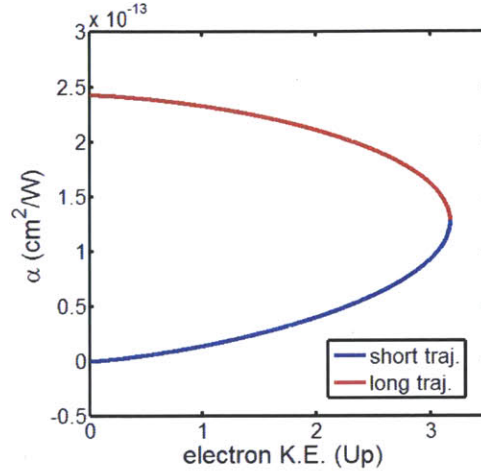


Fig. 3-1 The  $\alpha$  (Eq. (3.9)) coefficient of HHG dipole phase with 800-nm driver wavelength.

Combine these different wave-vector contributions, we reach the following expression for the mismatched wave-vectors:

$$\Delta k_q = \frac{q\omega_1}{c} \frac{P}{P_0} \left[ (1-\eta)(n_1 - n_q) - \frac{\eta\rho_0 e^2}{2m_e \epsilon_0 \omega_1^2} \left( 1 - \frac{1}{q^2} \right) \right] + (qk_1^G - k_q^G) - k_q^D. \quad (3.12)$$

When the pressure is low, phase-matching is achieved by balancing the pressure-independent terms like the geometric phase and the dipole phase. It has been shown that a thin gas jet can be placed behind the laser focus to achieve phase-matching [56]. For high pressure cases, Eq. (3.12) is dominated by the balance between the refractive indices of the neutral medium and the plasma dispersion [55]. The critical ionization level  $\eta_{cr}$  is the ionization level at which the refractive indices of the neutral medium and the plasma dispersion cancel each other [57], and can be easily solved from Eq. (3.12):

$$\eta_{cr} = (n_1 - n_q) \left[ (n_1 - n_q) + \frac{\rho_0 e^2}{2m_e \epsilon_0 \omega_1^2} \left( 1 - \frac{1}{q^2} \right) \right]^{-1} \approx \frac{2m_e \epsilon_0 \omega_1^2 (n_1 - n_q)}{e^2 \rho_0}. \quad (3.13)$$

The last approximation in Eq. (3.13) assumes  $\eta_{cr} \ll 1$  and  $q \gg 1$ , which is a good assumption in most cases. When the medium pressure is high, one should try to maintain  $\eta$  at  $\eta_{cr}$ . Once  $\eta$  equals to  $\eta_{cr}$ ,  $\Delta k_q$  is independent of the pressure according to Eq. (3.12). This is only true for one-dimensional case, and we will see that the fully dimensional calculation (Section 3.3) shows a much more complicated scenario of phase-matching. In a fully dimensional simulation, the driver pulse condition can change so significantly that  $\Delta k_q$  can be maintained constant only for a very short distance. In summary, to achieve phase-matching in HHG, one should control the laser intensity that affects  $\eta$ , the medium pressure, the focus size that influences both of the intensity and the geometric phase, and the position of the laser focus relative to the medium such that a balance can be reached among the phase-mismatches due to the neutral atom dispersion, plasma dispersion, geometric phase from the laser focus, and the dipole phase inherited from the HHG process.

Because phase-matching sets an optimal intensity for HHG, the cutoff cannot be scaled up unboundedly by simply increasing the peak intensity. Once the intensity exceeds the critical intensity  $I_{cr}$ , at which  $\eta$  equals to  $\eta_{cr}$  at the peak of the driver pulse, phase-matching is very difficult, and the HHG efficiency becomes poor. Therefore, the phase-matched cutoff can be defined as the cutoff at  $I_{cr}$ , which varies with the driver wavelength, pulse duration, and the HHG medium. Fig. 3-2 shows the phase-matched cutoff for 6-cycle pulses with Gaussian temporal profiles and different driver wavelengths in different HHG media. When phase-matching is considered, the cutoff roughly scales with the driver wavelength  $\lambda$  as  $\lambda^{1.4-1.7}$  [12,57].



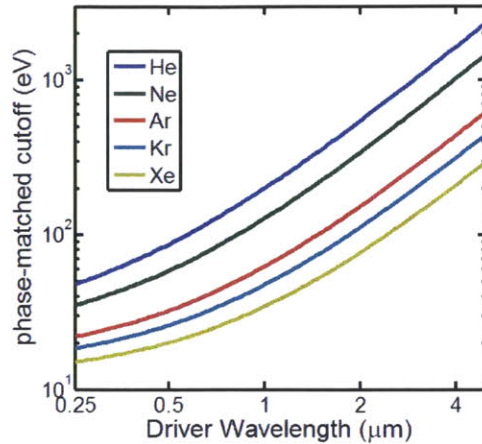


Fig. 3-2 Phase-matched cutoff for 6-cycle pulses with Gaussian temporal profiles and different driver wavelengths in different HHG media.

### 3.2 Plasma Defocusing

Another important macroscopic effect is the plasma defocusing effect on the driver pulse propagation. To compensate the low single atom efficiency, particularly for the long driver wavelength, one straight forward way is to increase the number of participating atoms by applying higher pressure to the interaction region. For low atomic density, the efficiency is enhanced quadratically with pressure [58], but plasma defocusing starts to become important as the free electron density increases. This effect not only decreases the cutoff photon energy but also shortens the interaction length for HHG. In this section, we numerically investigate plasma defocusing on IR pulse propagation in Ne and He and discuss how it affects HHG by defining an enhancement factor, which is a generalization of the analysis of Ref. [59]. For different pressures, the pulse intensity and ionization level may show quite different distributions that strongly impact the phase-matching condition and HHG efficiency.

Our numerical analysis first calculates how an optical pulse propagates and interacts with HHG gas media. In our situation, the model equation should include the effects of

diffraction, self-focusing, plasma defocusing, and ionization loss. Dispersion and other nonlinear effects can be neglected because the medium under consideration is either a short gas jet or a low-pressure 1cm-long gas cell. In the slowly evolving wave approximation, a first order propagation equation adapted from Ref. [60] is employed in our model:

$$\frac{\partial E}{\partial z} = \frac{i}{2k} \nabla_{\perp}^2 E + i \frac{k}{2} n_2 \varepsilon_0 c |E|^2 E - \frac{1}{2c} \int_{-\infty}^{\tau} \omega_p^2 E d\tau' - \frac{I_p}{2c\varepsilon_0 \operatorname{Re}(E)^2} \frac{\partial \rho}{\partial \tau} E, \quad (3.14)$$

where,  $E$  is the complex representation of the electric field;  $z$  and  $\tau$  are the propagation distance and the retarded time in the retarded time frame respectively;  $k$  is the wave-vector at the carrier frequency;  $\nabla_{\perp}^2$  is the transversal Laplace operator;  $n_2$  is the nonlinear index of refraction;  $\omega_p$  is the plasma frequency;  $I_p$  is the ionization potential of the atom;  $\rho$  is the number density of the ionized atoms. We assume that tunneling ionization is the only ionization mechanism, and therefore, the ADK formula gives an accurate description of the ionization rate  $\partial \rho / \partial \tau$  [46]. Since tunneling ionization depends on the phase of the electric field, the ionization loss term contains the real part of the electric field. Because of cylindrical symmetry,  $E$  is a function of  $z$ ,  $\tau$ , and the radial coordinate  $r$ .

Fig. 3-3 shows the peak intensity and ionization level distribution when a 2.5-mJ, 40-fs, 2- $\mu\text{m}$  laser pulse propagates from negative  $z$  to positive  $z$  through a He jet with three different pressures. The laser pulse is focused to an intensity of  $7 \times 10^{14}$  W/cm<sup>2</sup> at the center of the jets ( $z=0$ ). As the pressure becomes higher from Fig. 3-3 (a) to (c), plasma defocusing becomes more and more important. A drop of intensity near the center of the jet can be seen. Such a drop of intensity hinders the pulse from efficiently ionizing the gas and generating high harmonics. Fig. 3-3 (d)-(f) show the distribution of the ionization level (the fraction of atoms that are ionized). The strong defocusing effect in Fig. 3-3 (f) even prevents the pulse from approaching the center of the gas jet with a high intensity, so the

ionization and HHG can only occur in the low pressure wing before the gas jet. This effect decreases the advantage of using a high pressure gas jet. Fig. 3-4 shows the peak intensity and ionization level distributions when the same pulse considered in Fig. 3-3 propagates through a 1-cm-long helium cell with different pressures. The laser pulse is focused to the same intensity ( $7 \times 10^{14} \text{ W/cm}^2$ ) at the center of the cell ( $z=0$ ).

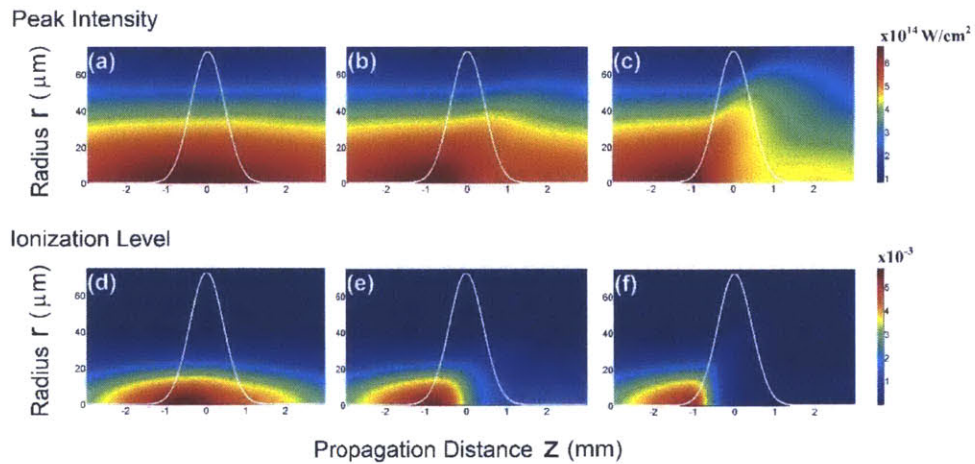


Fig. 3-3 Numerical results of the 2- $\mu\text{m}$  laser pulse propagation toward the  $+z$  direction through a He gas jet. The upper row shows the peak intensity when the peak pressure at the jet is (a) 0.1 bar, (b) 1 bar, and (c) 10 bar. The Gaussian curves illustrate the relative pressure profile of the jet. The lower row shows the ionization level when the pressure is (d) 0.1 bar, (e) 1 bar, and (f) 10 bar. The color scales of the intensity and the ionization level are shown on the side.

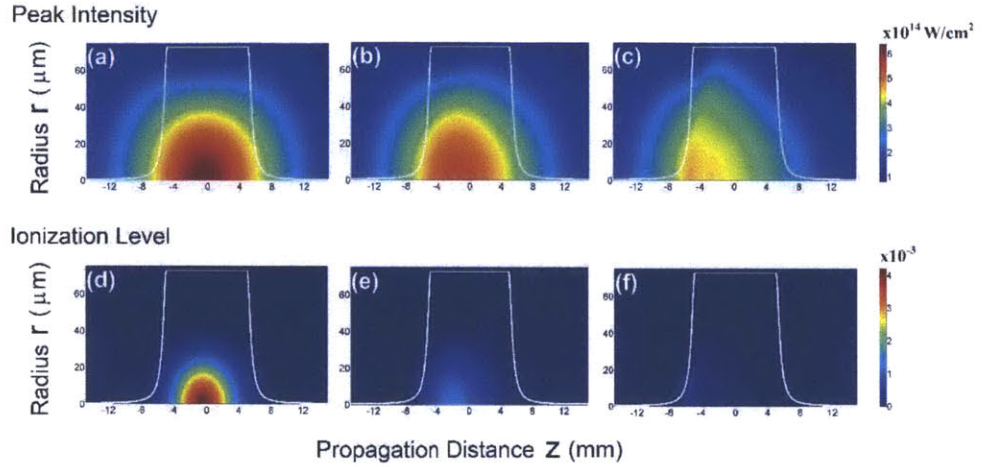


Fig. 3-4 Numerical results of the 2- $\mu\text{m}$  laser pulse propagation toward the  $+z$  direction through a He cell. The upper row shows the peak intensity when the pressure is (a) 0.1 bar, (b) 1 bar, and (c) 10 bar. The relative pressure is shown by the flat-top curve. The lower row shows the ionization level when the pressure is (d) 0.1 bar, (e) 1 bar, and (f) 10 bar. The color scales of the intensity and the ionization level are shown on the side.

To quantitatively discuss the influence of plasma defocusing, we introduce and calculate the HHG efficiency for the various cases. However, solving a three dimensional (3D) TDSE along with the 3D wave propagation is time-consuming, so we follow the analysis of Ref. [59] and generalize it to include plasma defocusing effect. It captures and analyzes the macroscopic properties of the HHG process, including phase-matching and reabsorption of the harmonics, and shows excellent agreement with experiment and HHG energy scaling [8,61]. The HHG energy of the  $q^{\text{th}}$  harmonic is assumed to be in the following form:

$$E_q = A\zeta(q, \lambda_l) \int 2\pi r dr \int d\tau \times \left| \int_{-L/2}^{L/2} \sqrt{w} P(z) \exp[iz\Delta k_q(r, z, \tau)] \exp[-\beta(z)(L-z)] dz \right|^2, \quad (3.15)$$

where  $A$  is a proportional constant;  $\zeta(q, \lambda_l)$ , as a function of the harmonic order  $q$  and the driver wavelength  $\lambda_l$ , is the SE;  $w=w(r, z, \tau)$  is the ionization rate given by the ADK formula;  $P(z)$  is the medium pressure;  $\Delta k_q=qk_l-k_q$  is the mismatch between the fundamental

and the  $q^{\text{th}}$  harmonic wave-vectors;  $\beta(z)$  represents the absorption of the harmonics. The integral with respect to  $z$  is due to the coherent addition of the high harmonic field generated over the non-uniform pressure distribution  $P(z)$ . The integral is over a range from  $-L/2$  to  $L/2$  that is long enough to cover the medium completely. Its magnitude squared would be proportional to the harmonic intensity generated from the point  $(r, \tau)$  in the parameter space. Then, the integrals over  $r$  and  $\tau$  consider the HHG contribution from every part of the driver pulse and result in the total amount of HH energy in a given harmonic. We neglect the depletion of the ground states because the ionization level considered here is always less than few percent. We define the integral part of Eq. (3.15) as the enhancement factor  $\xi$ :

$$\xi \equiv \int 2\pi r dr \int d\tau \left| \int_{-L/2}^{L/2} \sqrt{w} P(z) \exp[iz\Delta k_q(r, z, \tau)] \exp[-\beta(L-z)] dz \right|^2, \quad (3.16)$$

because it shows how much the SE is enhanced by the total HHG medium. Then the total HH energy can be rewritten as

$$E_q = A\zeta\xi. \quad (3.17)$$

This enhancement factor  $\xi$  comprises the propagation effects of HHG and is proportional to the HH energy, so it is useful for the investigation of the plasma defocusing effect.

The wave-vector mismatch  $\Delta k_q$  is important in the calculation of the enhancement factor  $\xi$ . For a multi-cycle pulse, phase-matching mainly depends on the neutral atom dispersion  $\delta k_a$ , the plasma dispersion  $\delta k_p$  that is induced by the free electrons, and the mismatches  $\delta k_g$  and  $\delta k_d$  that result from the geometric phase and the dipole phase respectively [62]. Therefore, the total wave-vector mismatch can be expressed as

$$\Delta k_q = \delta k_a + \delta k_p + \delta k_g + \delta k_d. \quad (3.18)$$



The geometric and dipole phases are particularly important for longer driver wavelengths for several reasons. Because most mid-IR OPA or OPCPA systems have to be focused tightly (usually with a beam size smaller than 100  $\mu\text{m}$ ) to generate HH, and then, the Gouy and dipole phases are not negligible. Besides, the Gouy phase is proportional to the driver wavelength for a fixed spot size, and the dipole phase is proportional to the driver wavelength cubed due to the longer trajectory and higher kinetic energy of electron during propagation. Last, the wave-vector mismatch is also proportional to the harmonic order that is larger for longer driver wavelength. Here we consider the contribution from the short-trajectory to HHG, and the dipole phase can be written as  $-\alpha_s I$ , where  $I$  is the laser intensity, and the coefficient  $\alpha_s$  can be calculated based on the harmonic order and the action of the semi-classical electron trajectory [63]. In the following simulation,  $\alpha_s$  is assumed to be  $5 \times 10^{-14}$  rad-cm<sup>2</sup>/W for 0.8- $\mu\text{m}$  driver wavelength. For other driver wavelengths, the coefficients are scaled with the cube of the wavelength.

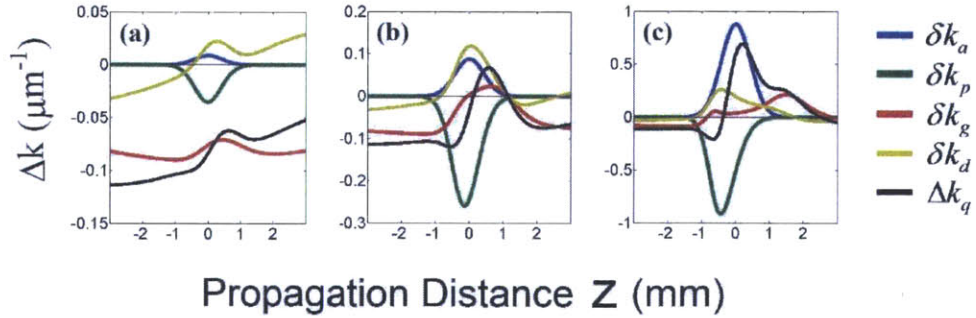


Fig. 3-5 The wave-vector mismatches in a He jet at  $r=0$  and  $\tau=0$  (pulse peak). The laser pulse and medium conditions are the same as Fig. 3-3, and the medium pressures are (a) 0.1 bar, (b) 1 bar, and (c) 10 bar respectively. The harmonic energy considered here is 500 eV. In each plot, the blue, green, red, and yellow curves show the mismatch due to neutral atom dispersion, plasma dispersion, geometric phase, and dipole phase respectively. The black curve shows the total wave-vector mismatch that is the sum of the above four curves.

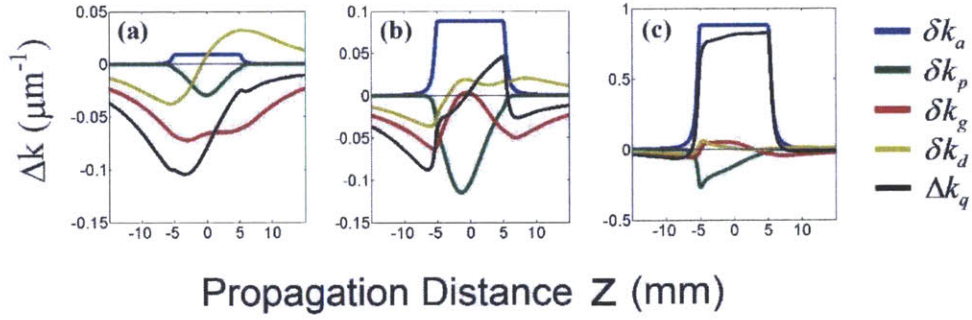


Fig. 3-6 The wave-vector mismatches in a He cell at  $r=0$  and  $\tau=0$  (pulse peak). The laser pulse and medium conditions are the same as Fig. 3-4, and the medium pressure is (a) 0.1 bar, (b) 1 bar, and (c) 10 bar respectively. The harmonic energy considered here is 500 eV. In each plot, the blue, green, red, and yellow curves show the mismatch due to neutral atom dispersion, plasma dispersion, geometric phase, and dipole phase respectively. The black curve shows the total wave-vector mismatch that is the sum of the above four curves.

Fig. 3-5 and Fig. 3-6 show and compare the four different sources of wave-vector mismatch seen by the peak of the driver pulse (i.e. at  $r=0$  and  $\tau=0$ ) under the same driver pulse condition and medium structure as Fig. 3-3 and Fig. 3-4 respectively. The harmonic energy considered in both figures is 500 eV, which is the 807<sup>th</sup> harmonic of the 2- $\mu\text{m}$  driver wavelength. The refractive indices used here for the driver pulses and the harmonics are taken from Ref. [64] and Ref. [65] respectively. At low pressure (Fig. 3-5 (a) and Fig. 3-6 (a),  $P=0.1$  bar), the geometric phase and the dipole phase are more dominant than the other two factors, and phase-matching ( $\Delta k_q=0$ ) can only be realized far behind the focus. As the pressure becomes higher (Fig. 3-5 (b) and Fig. 3-6 (b),  $P=1$  bar), all four contributions are comparable, and the total  $\Delta k_q$  shows complicated behavior. Phase-matching is achieved at some point near the center of the medium. At even higher pressure (Fig. 3-5 (c) and Fig. 3-6 (c),  $P=10$  bar), the total  $\Delta k_q$  basically follows the profile of the neutral atom dispersion because the negative plasma dispersion is roughly cancelled by the positive dipole and geometric phases.

When the ionization level is maintained below a few percent, the neutral atom dispersion is not affected by the plasma, but the other three phase-matching factors are still significantly influenced by plasma defocusing. As shown in Fig. 3-3 and Fig. 3-4, the ionization level that determines the plasma dispersion is very sensitive to the driver pulse intensity, which drops faster due to plasma defocusing. The fast drop of the driver pulse intensity then results in an enhanced dipole phase because the dipole phase of the short trajectory is proportional to the negative gradient of the driver pulse intensity. The geometric phase also changes due to the modification of the intensity profile along the radius direction. At low pressure, the geometric phase is almost the same as the Gouy phase of a focused Gaussian beam. When the pressure increases, and the plasma defocusing becomes stronger, the geometric phase that results from the diffraction can be quite different from the Gouy phase as shown in Fig. 3-5 and Fig. 3-6. Therefore, plasma defocusing not only reduces the pulse intensity, but also influences the phase-matching. It is difficult to control and balance all these factors around  $\Delta k_q=0$  for a long distance. Instead,  $\Delta k_q$  often crosses the  $\Delta k_q=0$  line with some slope. To improve the HHG efficiency in such a situation, one should try to decrease the slope and move the crossing point to the high density part of the medium.



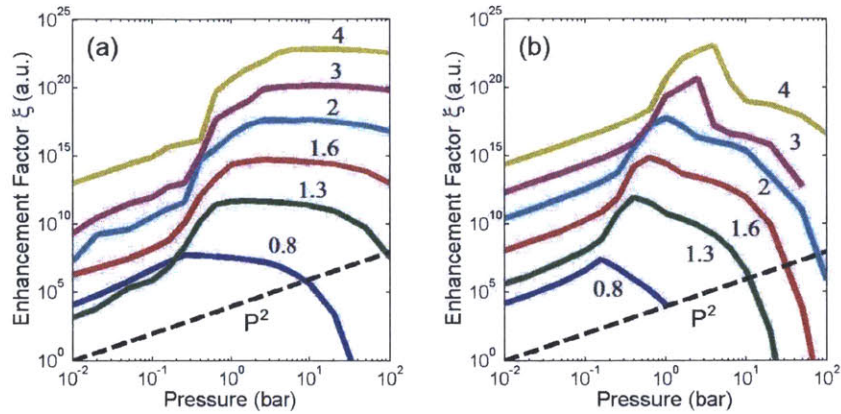


Fig. 3-7 Enhancement factor  $\xi$  for He. (a) and (b) show the enhancement of a 1-mm He jet and a 1-cm He cell respectively. For each driver wavelength, the curve is intentionally shifted for clarity. The number near each curve indicates the driver wavelength in units of  $\mu\text{m}$ . For comparison, the dashed lines show a parabolic dependence on pressure.

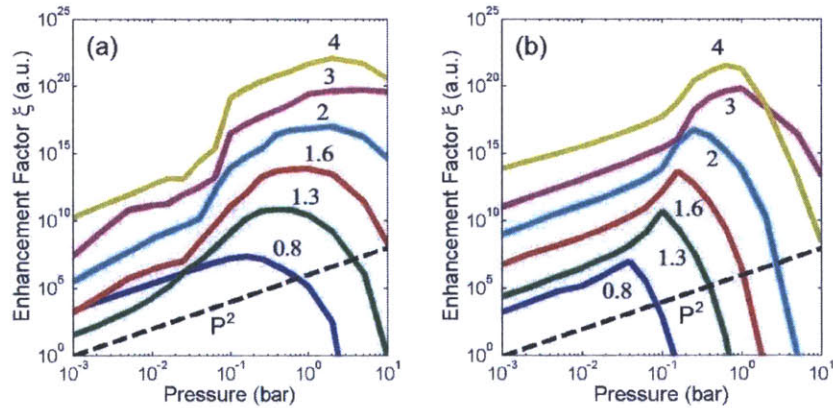


Fig. 3-8 Enhancement factor  $\xi$  for Ne. (a) and (b) show the enhancement of a 1-mm Ne jet and a 1-cm Ne cell respectively. For each driver wavelength, the curve is intentionally shifted for clarity. The number near each curve indicates the driver wavelength in units of  $\mu\text{m}$ . For comparison, the dashed lines show a parabolic dependence on pressure.

Fig. 3-7 shows the calculated enhancement factors  $\xi$  for a He jet and a He cell for six different driver wavelengths and varying pressure. In Fig. 3-7 (a), there are sharp transitions at about 0.1 bar, because at this pressure a transition from phase-mismatched HHG to phase-matched HHG occurs. At low pressure ( $<0.1$  bar), Gouy phase and dipole

phase dominate, and the phase-matching point where  $\Delta k_q=0$  is located far behind the gas jet. Therefore, phase-matching cannot be achieved with low density media density, and the HHG efficiency is poor. When the pressure is low,  $\Delta k_q$  doesn't change much with the increasing pressure. Therefore the HHG efficiency still increases quadratically with the medium pressure although it is not phase-matched at all. Once the pressure is high enough ( $>0.1$  bar), the neutral atom dispersion is able to compensate the other phase-matching factors and results in a phase-matching point within the gas jet. Correspondingly the enhancement factor  $\xi$ , and with it the HHG efficiency, increase drastically. This transition phenomenon is less sharp for shorter driver wavelengths due to the smaller Gouy and dipole phases and smaller harmonic orders. With higher medium density, the strong plasma defocusing and reabsorption start to limit the HHG efficiency and result in a saturation feature with optimal medium pressure for  $\xi$ . In Fig. 3-7 (b), the basic features of a He cell are similar to those of a He jet except that the optimal pressure is lower due to a longer interaction length. Fig. 3-8 shows the enhancement factor  $\xi$  for Ne. The same sharp transition can be seen at lower medium pressures because Ne has larger neutral atom dispersion. Compared to He, the larger reabsorption of Ne limits the optimal pressure to lower values than those of He.

The calculated optimal pressures in Fig. 3-7 and Fig. 3-8 show excellent agreement with experiment. For 0.8- $\mu\text{m}$  driver wavelength, Fig. 3-7 and Fig. 3-8 show optimal HHG efficiency at a few hundreds mbar for gas jets and a few tens mbar for Ne cells. These are typical values applied in experiment [5,58]. To further verify our model, we simulate the experiment in Ref. [8]. As shown in Fig. 3-9, the calculated optimal pressures for He and Ne are 25 mbar and 18 mbar respectively, which are close to the experimental pressures at 26 mbar and 13 mbar. To show that these optimal pressures are closely related to plasma

defocusing, we also calculate the enhancement factor without any plasma defocusing, as shown by the dashed curves in Fig. 3-9. The dashed curves are calculated by neglecting the impacts of refractive index and losses due to plasma onto the driver pulses. The intensity distribution and the ionization level provide the information to calculate the enhancement factor, as shown in Fig. 3-9. The sharp turn on the dashed curve in Fig. 3-9 (b) is due to strong phase mismatching. The initial intensity is too high and generates too much plasma that causes very strong phase-mismatching. This phase-mismatched HHG has a coherence length [59] comparable to the medium length when the pressure is 10 mbar. When the pressure is higher than 10 mbar, the coherence length becomes shorter, and the enhancement cannot benefit more from the higher pressure. In Fig. 3-9 (b), plasma defocusing decreases the intensity to an appropriate level for phase-matching, so the enhancement can be larger than for the case without plasma-defocusing. Beyond 0.8- $\mu\text{m}$  HHG experiments, our 1.6- $\mu\text{m}$  result also matches Ref. [10] well. The Ne jet in Ref. [10] is optimized at 0.76 bar that is close to our optimal pressure at 1 bar for a Ne jet. Determining the working pressure is important to the design of the vacuum system and the choice of appropriate gas geometry. The numerical analysis on plasma defocusing provided here gives the necessary information as well as the maximum enhancement due to the macroscopic propagation effects of the medium, and is therefore of great practical importance.

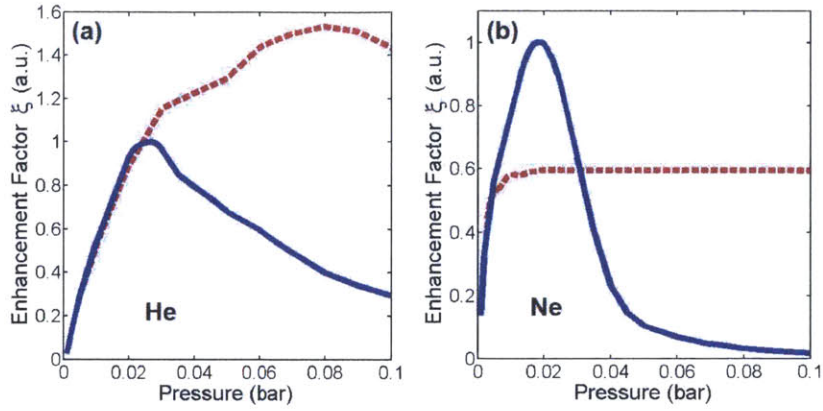


Fig. 3-9 Enhancement factor for 0.8- $\mu\text{m}$  driver wavelength with high pulse energy and loose focusing. For (a) He, a 130-mJ pulse is focused into a 5-cm-long gas cell with 590- $\mu\text{m}$  beam radius. For (b) Ne, a 50-mJ pulse is focused into a 4-cm-long gas cell with 360- $\mu\text{m}$  beam radius [8]. The solid curves consider plasma defocusing, while the dashed ones don't.

In conclusion, we quantitatively analyzed the influence of plasma defocusing and phase-matching on HHG for different driver wavelengths by defining and comparing the enhancement factor  $\xi$  that considers macroscopic characteristics including plasma defocusing, reabsorption of harmonics, and phase-matching. Our numerical result shows good agreement with experiment and provides an easy way to calculate and explain HHG performance without referring to the complex microscopic behavior of strong field dynamics and the atomic parameters. Although increasing the medium pressure can partially make up the severe loss of SE with longer driver wavelengths, the compensation is still limited by the plasma defocusing.

### 3.3 Fully Dimensional Simulation

A fully dimensional HHG simulation that takes into account most physics related to a real HHG experiment is developed by combining the macroscopic factors (phase-matching and pulse propagation) presented in this chapter with the single-atom response discussed in Chapter 2. Since the HHG efficiency is very low, there is little backward interaction from

the HH on the fundamental driver field. In other words, the propagation of the fundamental driver pulse can be calculated independently by Eq. (3.14), and the driver field distribution  $E(r,z,\tau)$  at any spatial-temporal point  $(r,z,\tau)$  is calculated and saved before any computation related to HHG. Next, for each spatial point  $(r,z)$ , the driver electric field  $e(\tau)$  is a function of time, and the HH generated at  $(r,z)$  is determined solely by  $e(\tau)$  and can be calculated by Eq. (2.35) of the TSM. The last step is to convert the HH dipole moment to HH electric field, propagate it through the medium, and integrate the HH fields over  $(r,z)$ .

The bottleneck of the entire computation project is to calculate Eq. (2.35) for a given  $e(\tau)$  efficiently. A routine that takes  $e(\tau)$  as the input and outputs the HH dipole  $x(\tau)$  as a function of time will be called frequently. The temporal grid size of  $x(\tau)$  has to be much smaller than the grid size required for the driver pulse propagation because the wavelength of the HH can be as short as few nm while the driver wavelength is usually in the order of  $\mu\text{m}$ , which means that the minimal temporal grid size has to be 2 to 3 orders finer for HH calculation than for driver pulse propagation. Therefore, a huge number of temporal grids will be needed. Another challenge is the mapping between the recombination time  $t_r$  and the ionization time  $t_b$ . Since  $t_r$  is also the temporal coordinate shared by the other variables in the simulation, it is usually represented by a set of predetermined uniform grids for convenience. Therefore,  $t_b$ , as a nonlinear function of  $t_r$ , should be solved from the saddle point equations Eq. (2.32) and Eq. (2.33). It is time-consuming to calculate  $t_b$  for a given  $t_r$  by searching the root of a nonlinear function.

Fortunately, many variables needed for single-atom response calculation can be easily rescaled for any sinusoidal driver field. In other words, most of the work solving Eq. (2.32) and Eq. (2.33) can be done before the simulation runs. For a sinusoidal driver field

$E(t) = E_0 \cos(\omega t)$  with a constant amplitude  $E_0$ , the saddle point equations Eq. (2.32) and Eq. (2.33) tell us to find a trajectory that starts with vanishing initial velocity at the ionization time  $t_b$  and returns to the origin at the recombination time  $t_r$ . The acceleration  $a$ , the velocity  $v$ , and the position  $d$  of the trajectory at  $t_r$  are

$$a(t_r) = E_0 \cos(\phi_r); \quad (3.19)$$

$$v(t_r) = \frac{E_0}{\omega} [\sin(\phi_r) - \sin(\phi_b)]; \quad (3.20)$$

$$d(t_r) = -\frac{E_0}{\omega^2} [\cos(\phi_r) - \cos(\phi_b)] - \frac{E_0}{\omega^2} (\phi_r - \phi_b) \sin(\phi_b), \quad (3.21)$$

where

$$\phi_r = \omega t_r; \quad (3.22)$$

$$\phi_b = \omega t_b. \quad (3.23)$$

Setting Eq. (3.21) to zero, we can solve  $\phi_b$  as a function of  $\phi_r$ , as shown in Fig. 2-6 (a). The action  $S$ , which is the kernel of Eq. (2.35), can also be calculated by

$$S = \frac{E_0^2}{2\omega^3} (\phi_r - \phi_b) \left\{ \gamma^2 - \frac{[\cos(\phi_r) - \cos(\phi_b)]^2}{(\phi_r - \phi_b)^2} + \left[ \frac{1}{2} - \frac{\sin(2\phi_r) - \sin(2\phi_b)}{4(\phi_r - \phi_b)} \right] \right\}, \quad (3.24)$$

where the dependences on  $E_0$ , and  $\omega$  are factored out in front of a function of  $(\phi_b, \phi_r)$  that is general to any individual cycle of the driver pulse. The central idea to calculate  $x(\tau)$  from  $e(\tau)$  is to identify each cycle of  $e(\tau)$  along with its amplitude  $E_0$  and frequency  $\omega$  (the frequency actually changes during propagation because of plasma blue shift), appropriately rescale the quantities involved in Eq. (2.35) ( $E(t_b)$ ,  $(t_r - t_b)$ ,  $S$ ) with  $E_0$  and  $\omega$ , and calculate  $x(\tau)$  cycle-by-cycle rather than point-by-point. Interpolation is needed to match  $\phi_r$  to  $\tau$  since the instantaneous frequency  $\omega$  may be altered by the plasma blue shift effect. The idea can be generated to electric field of the following form:

$$E = E_0 (1 + \alpha \phi_r) \cos(\phi_r) \quad (3.25)$$

to account for the envelope variation within one cycle as long as the variation is not too dramatic for linear approximation. The coefficient  $\alpha$  will be determined for each cycle individually.

To demonstrate the fully dimensional calculation, we consider several cases of HHG in Ar gas jets with Gaussian pressure profile and 2-mm FWHM jet length. The pulse duration and the central wavelength of the driver pulses are 35 fs and 800 nm respectively for all of the cases, but the pulse energy and the focus spot size are different. The peak pressure of the gas jet also varies. The parameters are summarized in Table 3-1. Basically, Case 1 is very close to the optimal condition for HHG in Ar, and we increase the peak intensity or the medium pressure in Case 2-4 to see how plasma defocusing spoils the conversion efficiency. In Case 5 and Case 6, the peak intensities are the same as Case 1, but the pulse energies and the focus spot sizes are adjusted to demonstrate the effect of loose focusing. In HHG experiment, the relative position between the laser focus and the gas jet position is also important, but this degree of freedom is neglected here for simplicity.

Table 3-1 Simulation Parameters for Fig. 3-10, Fig. 3-11, Fig. 3-12, and Fig. 3-13

| Case | Pulse Energy (mJ) | Peak Pressure (mbar) | Focus Spot Size ( $\mu\text{m}$ ) |
|------|-------------------|----------------------|-----------------------------------|
| 1    | 1                 | 100                  | 90                                |
| 2    | 1                 | 100                  | $90/\sqrt{2}$                     |
| 3    | 1                 | 200                  | 90                                |
| 4    | 2                 | 100                  | 90                                |
| 5    | 2                 | 100                  | $90/\sqrt{2}$                     |
| 6    | 0.5               | 100                  | $90/\sqrt{2}$                     |



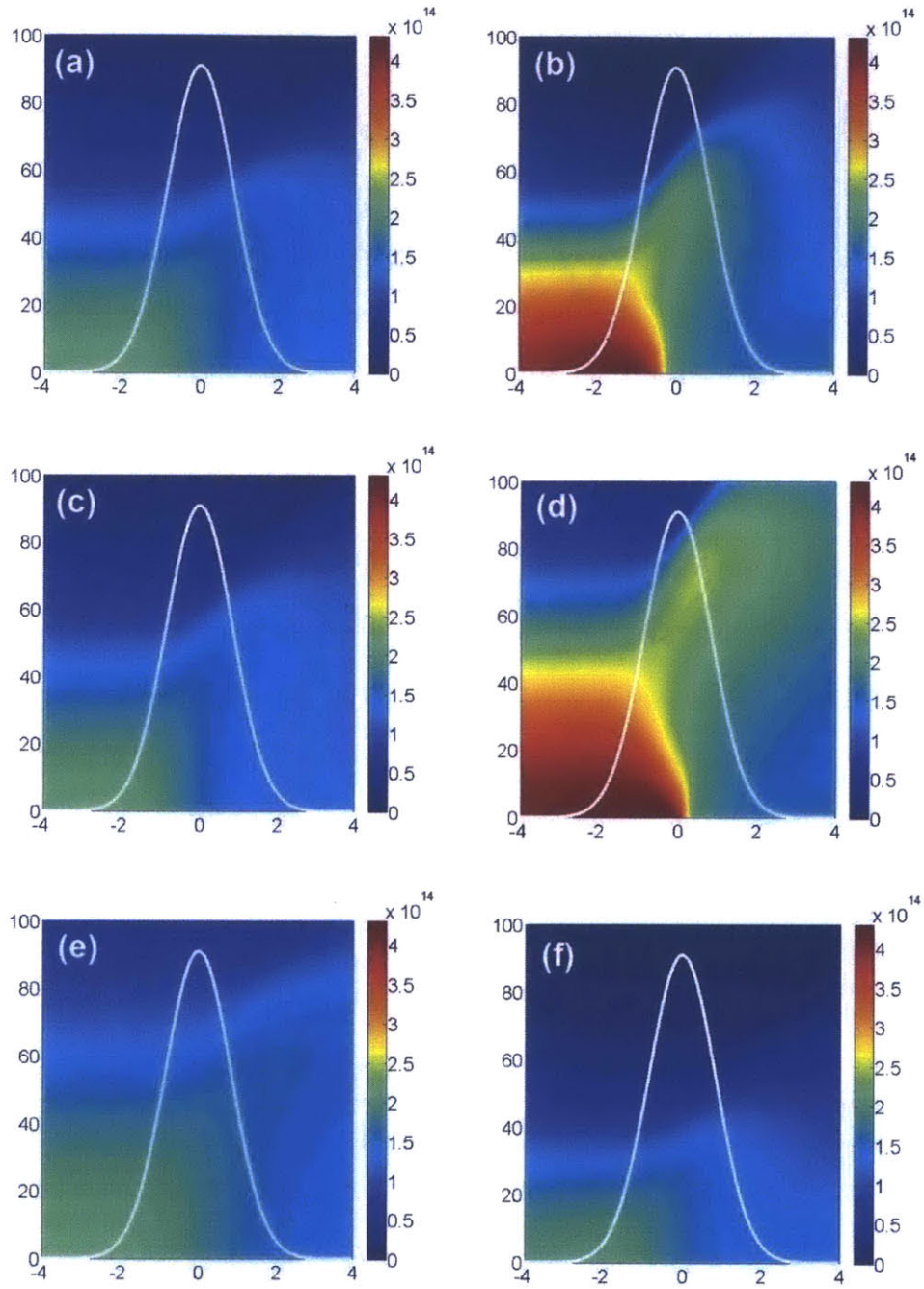


Fig. 3-10 The peak intensity distribution of (a) Case 1, (b) Case 2, (c) Case 3, (d) Case 4, (e) Case 5, and (f) Case 6 listed in Table 3-1. The horizontal axes show the coordinate along the propagation dimension in mm, and the vertical axes show the radial coordinate in  $\mu\text{m}$ . The white contours show the pressure profile of the gas jet. The unit of the color scale is  $\text{W}/\text{cm}^2$ .



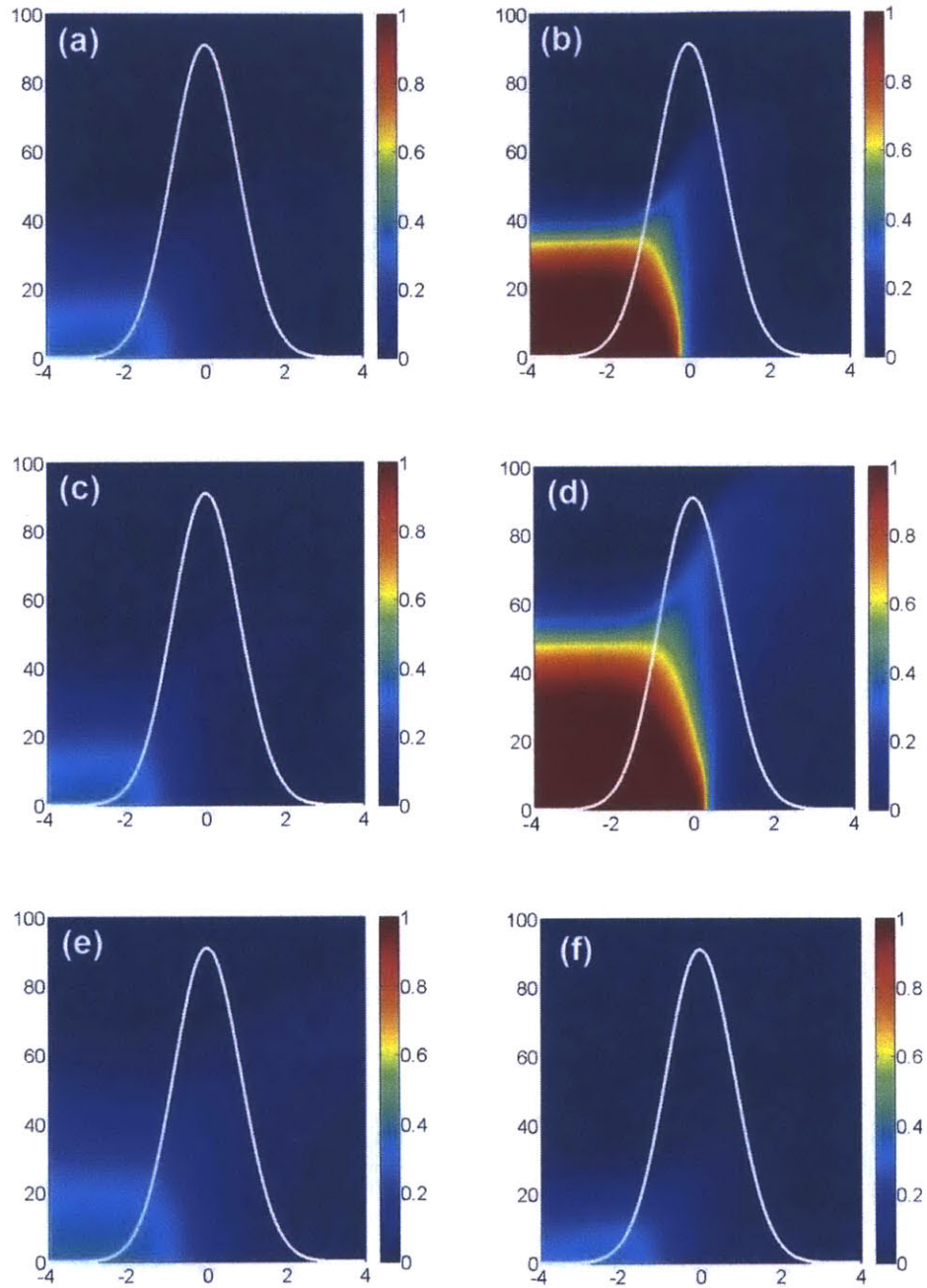


Fig. 3-11 The ionization level of (a) Case 1, (b) Case 2, (c) Case 3, (d) Case 4, (e) Case 5, and (f) Case 6 listed in Table 3-1. The horizontal axes show the coordinate along the propagation dimension in mm, and the vertical axes show the radial coordinate in  $\mu\text{m}$ . The white contours show the pressure profile of the gas jet. The color scale indicates the fraction of ionized atoms.

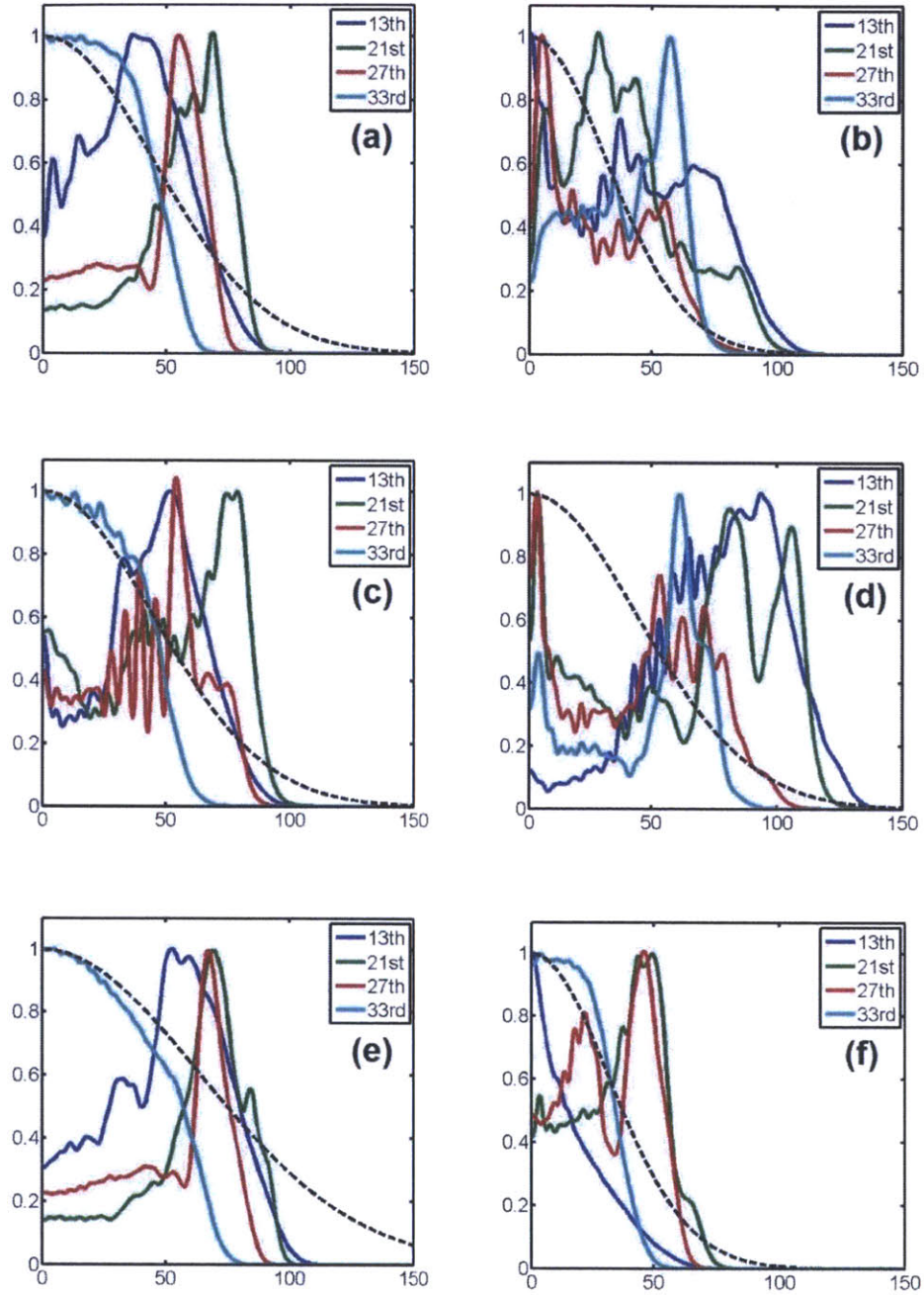


Fig. 3-12 The spatial profiles of the 13<sup>th</sup> (20.2 eV), 21<sup>st</sup> (32.6 eV), 27<sup>th</sup> (41.9 eV), and 33<sup>rd</sup> (51.2 eV) harmonics of (a) Case 1, (b) Case 2, (c) Case 3, (d) Case 4, (e) Case 5, and (f) Case 6 listed in Table 3-1. The horizontal axes indicate the radius in  $\mu\text{m}$ , and the vertical axes show the normalized HH intensities. The dotted black curve is the spatial profile of the focused driver pulse, which is Gaussian.

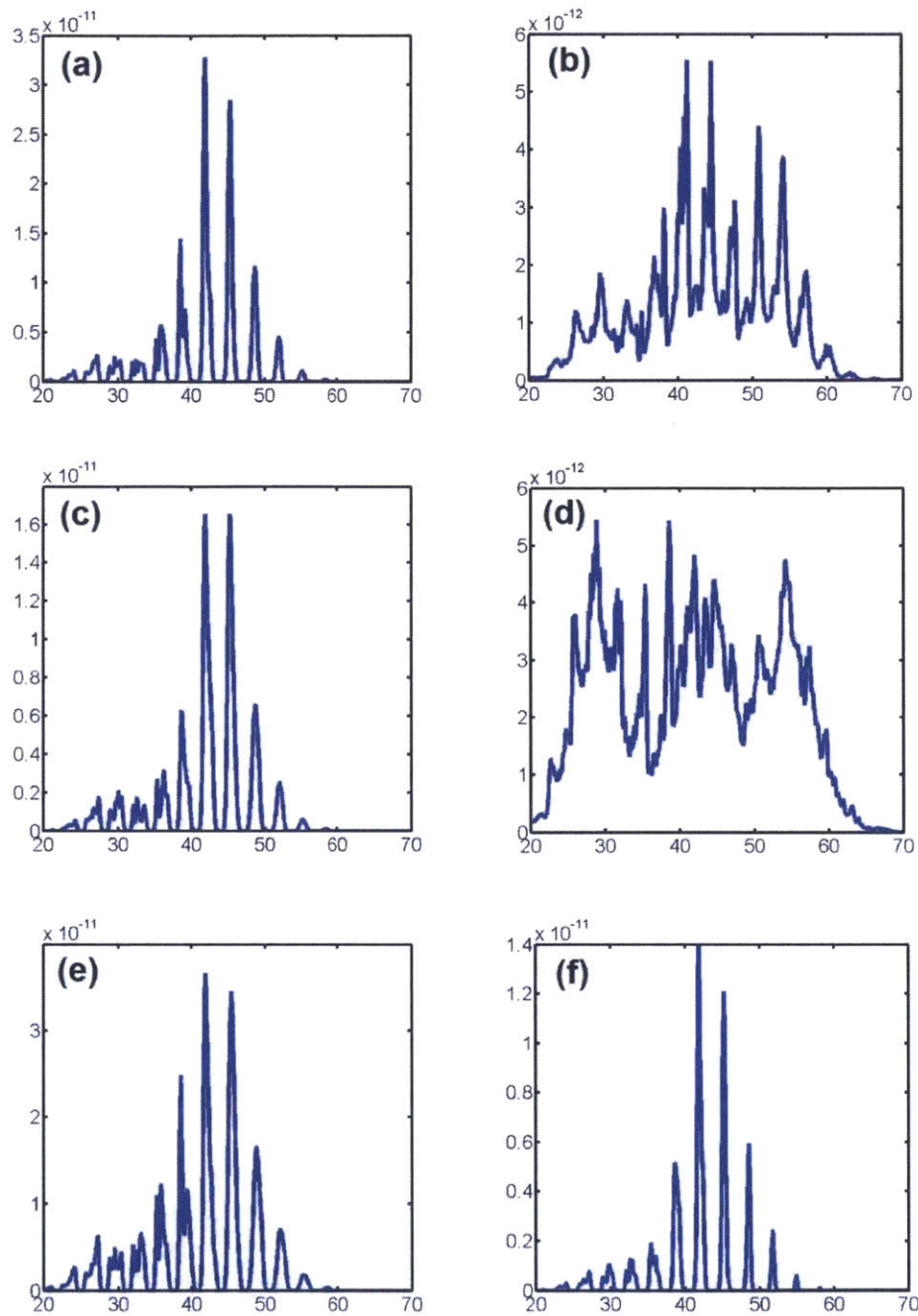


Fig. 3-13 The HHG spectra of (a) Case 1, (b) Case 2, (c) Case 3, (d) Case 4, (e) Case 5, and (f) Case 6 listed in Table 3-1. The horizontal axes show the photon energy in eV, and the vertical axes show spectral energy density in J/eV. Note that the scales of the vertical axes are different. The spectra are obtained by integrating over the radius.

Fig. 3-10 shows the peak intensity distribution, and strong plasma defocusing effect can be clearly seen from the asymmetric distribution around the focus at  $z=0$ . Fig. 3-11 shows the ionization level after the pulses completely pass through the medium. In Fig. 3-11 (b) and Fig. 3-11 (d), a significant portion of the gas is totally ionized due to the twice higher intensity than the other cases. In the other cases, the ionization level is around 0.2-0.4, and thus the ionization level at the peak of the pulse should be about half, i.e. 0.1-0.2. Note that at the center of the gas jet ( $z=0$ ) where the medium is the most dense, the ionization level is even lower such that the ionization level is close to the critical ionization level 0.04 for Ar. Fig. 3-12 shows the spatial profiles of several selected harmonics. In fact, the spatial profiles are not good because of the complicated phase-matching process and dipole phases, particularly for the cases with higher peak intensity (Fig. 3-12 (b) and Fig. 3-12 (d)). Most of the complex structure on the spatial profile is related to the long trajectory. In a real experiment, the long trajectory HHG diverges much faster during propagation than the short trajectory, and thus the far field is mainly composed of the short trajectory that has better spatial quality.

Fig. 3-13 shows the HHG spectra for the six cases. In Fig. 3-13 (a)-(d), the driver energy is 1 mJ, but Fig. 3-13 (a) shows much better efficiency than Fig. 3-13 (b)-(d) due to the moderate intensity and medium pressure. Fig. 3-13 (e)-(f) have the same peak intensity and pressure as Fig. 3-13 (a), but Fig. 3-13 (e) has 2 mJ while Fig. 3-13 (f) has only 0.5 mJ. Although the harmonic intensity in Fig. 3-13 (e) looks similar to Fig. 3-13 (a), the harmonic lines in Fig. 3-13 (e) are actually wider, and the total HHG yield is twice higher than Fig. 3-13 (a) after integrating over the entire bandwidth. This means that the efficiency of HHG has reached some saturation value that does not vary too much as the driver pulse energy increases. However, the efficiency of Fig. 3-13 (f) is clearly worse than Fig. 3-13 (a), and the total yield of Fig. 3-13 (f) is only 37%, rather than 50%, of that of Fig.

3-13 (a), after integrating over the spectrum. The degraded efficiency is due to the tighter focusing and the stronger Gouy phase that impedes the phase-matching. The spectra in Fig. 3-13 have incorporated the scattered-wave recombination amplitude shown in Fig. 2-4 (a).

One important problem of the simulated HHG spectra is the discrepancy between the experiment-measured absolute efficiency and the absolute HHG efficiency calculated here. Fig. 3-13 (a) shows a peak efficiency of  $\sim 10^{-8}$  while experiment has reported an efficiency of  $10^{-6}$ . It is unusual that a theoretical efficiency is lower than the experimental value by several orders. In fact, as shown in Fig. 3-5 and Fig. 3-6, phase-matching condition is difficult to maintain for a long distance in the fully dimensional simulation, although many experiments have claimed that phase-matching is achieved. Since HHG is a complicated coherent process with strong reabsorption from the medium, it is not easy to identify the phase-matching feature from other density-dependent effects, like the reabsorption. Meanwhile, the measurement of the absolute photon flux in the EUV and soft X-ray regime is not easy, and most HHG experiments only report the relative dependence of HHG signal on experimental parameters or show HHG spectra in arbitrary units. Nevertheless, we cannot rule out the possibility that something important has been neglected in the simulation work, or even some hidden new physics is at play.

### **3.4 Medium Length**

One interesting question is the comparison between HHG media with different lengths but same pressure-length product (PLP). In a phase-matched situation, the total yield is proportional to the PLP squared, so the medium length makes no difference as long as the PLP is constant. However, phase-matching and plasma defocusing can make things complex [55]. Under the same peak intensity, a medium of higher pressure must have more free electrons and induce more diverging phase on the driver pulse wave-front. On the

other hand, however, the shorter medium length can mitigate the diffraction effect and reduce the impact of the plasma defocusing. It is not obvious which situation suffers less plasma defocusing and gives better efficiency. This section tries to show that shorter medium with higher pressure may be more favorable under certain conditions.

Because of reabsorption and vacuum pumping issues, HHG targeting at EUV regime usually uses medium with pressure no more than few hundred mbar, and the most critical term in the wave propagation equation is the plasma defocusing according to previous calculation. Under slow varying envelope approximation, the propagation equation can be written as:

$$\frac{\partial A}{\partial z} = \frac{i}{2k} \nabla_T^2 A - \frac{ik}{2} \frac{\omega_p^2}{\omega^2}, \quad (3.26)$$

where  $A$  is the slowly-varying amplitude of the driver pulse;  $z$  is the propagation distance;  $k$  is the wave-vector of driver pulse;  $\nabla_T^2$  is the Laplacian on the transverse spatial coordinate;  $\omega_p$  is the plasma frequency;  $\omega$  is the driver frequency. If  $A = A(r, z, \tau)$  with radius coordinate  $r$  and local time  $\tau$  is a solution to Eq. (3.26), then  $A_N \equiv A(\sqrt{N}r, Nz, \tau)$  satisfies:

$$\frac{\partial A_N}{\partial z} = \frac{i}{2k} \nabla_T^2 A_N - \frac{ik}{2} \frac{N\omega_p^2}{\omega^2}, \quad (3.27)$$

which happens to be the propagation equation for a medium with  $N$  times higher pressure. Here we assume that the change of the wave-vector  $k$  is negligible when the pressure changes, and this is true for dilute gas. Therefore, we can conclude that the propagation behavior is invariant for a medium with  $N$  times higher density if we scale down the propagation dimension by a factor of  $N$  and the beam size by a factor of the square root of  $N$  respectively. Because the peak intensity is constant, the pulse energy will become  $N$  times smaller, too. Table 3-2 lists three cases to illustrate the idea. In Case 1 and Case 2,



the pulses are expected to propagate in the same way except for a scaling factor  $N=2$ . Case 1 and Case 2 should suffer the same amount of plasma defocusing, and the HHG flux of Case 2 will be exactly 50% of Case 1 because Case 2 only has 50% driver pulse energy of Case 1. In other words, Case 1 and Case 2 have the same HHG efficiency.

Table 3-2 Parameters for Medium Length Comparison

| Case | Energy (mJ) | Focus Size ( $\mu\text{m}$ ) | Medium Length (mm) | Pressure (mbar) |
|------|-------------|------------------------------|--------------------|-----------------|
| 1    | 2           | 90                           | 2                  | 100             |
| 2    | 1           | $90/\sqrt{2}$                | 1                  | 200             |
| 3    | 2           | 90                           | 1                  | 200             |

The medium is Ar gas jet with Gaussian pressure profile. The medium length is the FWHM of the jet, and the pressure is the peak pressure at the center of the jet.

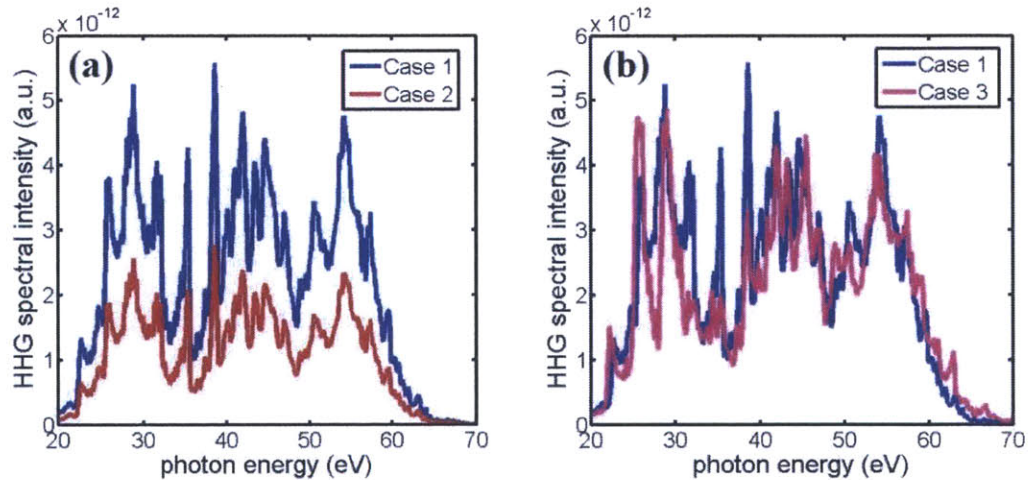


Fig. 3-14 (a) HHG spectra of Case 1 (blue) and Case 2 (Red). The two spectra have exactly the same shape except for an overall scaling factor of 2. (b) HHG spectra of Case 1 (blue) and Case 3 (pink).

The fully dimensional simulation introduced in last section confirms this observation precisely by showing two HHG spectra that have exactly the same shape except for an overall constant factor of 2 in Fig. 3-14 (a). Case 1 here is the same as the Case 4 in Table

3-1, so its peak intensity and ionization level distributions can be found in Fig. 3-10 (d) and Fig. 3-11 (d) respectively. Even the intensity is so high that a significant portion of the gas jet is 100% ionized, the rescaling relation is still preserved in Fig. 3-14 (a), which lends strong support to the analytical conclusion and the accuracy of the fully dimensional simulation at the same time. The plasma defocusing of Case 3 must be less than Case 2 because of the larger beam size under the same medium condition. Furthermore, Case 3 also suffers less Gouy phase due to looser focusing. Therefore, the HHG efficiency of Case 3 should be higher than Case 2 in principle. Logically, one can always split the 2-mJ pulse energy of Case 3 into two halves and repeat the experiment of Case 2 twice, so the efficiency of Case 3 cannot be lower than Case 2. A comparison relation among the HHG efficiencies of the three cases is thus established: Case 1 = Case 2  $\leq$  Case 3.

Fig. 3-14 (b) compares the HHG spectra from Case 1 and Case 3, but the efficiency of Case 3 is actually lower. This is because in the three cases discussed here, there has been too much plasma, and the phases are almost random. Loose focusing can reduce the plasma defocusing and enhance the HHG efficiency only when the phase mismatch is not too chaotic. However, the difference of the two spectra in Fig. 3-14 (b) shows that the HHG spectrum is sensitive to the experimental conditions, and the matching of the spectral shape in Fig. 3-14 (a) is not a coincidence. Since the advantage of loose focusing has been demonstrated by comparing the Case 5 and Case 1 of Table 3-1 in last section, so we can conclude that a shorter but denser HHG medium will give a better efficiency. Last, although Eq. (3.26) only considers the diffraction and the plasma term, it can be generalized by including other terms proportional to the medium density, like the self-focusing, without changing our conclusion.



Care should be taken at the boundary of a gas cell. Assume the gas cell is isolated from the vacuum chamber by a wall with an orifice on it at  $z=0$ , and the pressure continuously drops from the  $+z$  side to  $-z$  side, as illustrated in Fig. 3-15. Practically, when the cell pressure is doubled, the pressure profile usually changes from the lower blue curve in Fig. 3-15 to the higher blue curve with the same pressure decay length. However, our rescaling argument requires the decay length to be scaled down by a factor of 2 as well. Therefore, the correct rescaled pressure profile should be the red one in Fig. 3-15 which can be achieved by decreasing the orifice size. When the medium pressure is high, the decay length outside the orifice is important because it may defocus the driver pulse significantly before it enters the cell.

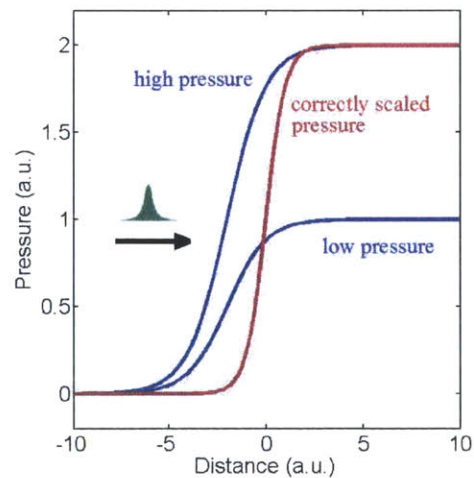


Fig. 3-15 Illustration of length scaling of the HHG medium.

### 3.5 Conclusion

The phase-matching of HHG is more complicated and more difficult than the conventional lower harmonic generation because the much higher harmonic order makes the process extremely sensitive to not only the refractive index of the medium but also the geometric

phase of the driver pulse and the dipole phase due to the excursion of the electron. However, the most difficult part is the control over the plasma. We numerically investigate the influence of plasma defocusing in HHG by solving the first-order wave equation in an ionized medium and defining an enhancement factor to quantitatively analyze the influence of plasma defocusing. While degrading the driver pulse intensity, plasma also has a strong impact on HHG phase-matching. Although the high energy photons generated by longer driver wavelength suffer much less reabsorption, however, increasing the medium density only has a limited enhancement of the efficiency due to the stronger plasma defocusing at higher medium density. Although plasma defocusing is complicated and makes the HHG process less straightforward, by rescaling the variables in the wave equation, we can show that a better confined medium, i.e. a shorter medium with higher density, should be more favorable for HHG.

Combining the macroscopic factors with the single atom response of HHG, a fully dimensional HHG simulation model is built. Our model includes the diffraction, the ionization, and plasma defocusing in the driver pulse propagation along with other minor effects like self-phase modulation and the loss due to ionization and the acceleration of the electron. The single atom response is calculated by the TSM. To speed up the computation, the driver pulse is assumed not in the few-cycle regime. Then, all of the kinematic variables needed for the TSM can be normalized with the driver intensity and the driver frequency, and the computation of the single atom response is improved from a time-consuming point-to-point process to an efficient cycle-by-cycle process. The algorithm allows us to simulate a fully dimensional case of HHG within a reasonable amount of time. However, the calculated absolute efficiency is a few orders of magnitudes less than the experiment result, and this discrepancy requires a careful examination in the future.

# Chapter 4

## High Harmonic Generation Driven by Ti:Sapphire Based Lasers

The typical intensity required for HHG around  $10^{14}$ - $10^{15}$  W/cm<sup>2</sup> can be easily achieved by commercially available Ti:sapphire lasers nowadays, so laser systems based on Ti:sapphire technology, including the 800-nm femtosecond pulses directly from Ti:sapphire lasers, its second or third harmonics, and optical parametric amplification (OPA) systems pumped by Ti:sapphire lasers, have been prevalent in HHG experiment. In this chapter, three experiments done with Ti:sapphire lasers will be discussed. Section 4.1 compares the HHG results from 400-nm and 800-nm driver pulses to show the significant enhancement of HHG efficiency using shorter driver wavelength. Because the HHG efficiency is enhanced at the cost of the HHG cutoff, Section 4.2 studies the wavelength scaling of HHG cutoff driven by shorter wavelengths in the visible regime generated by an OPA that is pumped by the second harmonic of a Ti:sapphire amplifier and has a tunable signal wavelength. The same tunable OPA system is also used to study the wavelength scaling of HHG efficiency, and the experimental results have been discussed in Section 2.4. In Section 4.3, more detail about the experiment design will be presented. Section 4.4 will give a conclusion about these experiments with Ti:sapphire lasers.

#### **4.1 Comparison between 400nm and 800nm Driver Wavelengths**

Efficient HHG driven by short wavelength (visible) will be of significant impact on many applications requiring high-flux EUV sources in the range of 30-100 eV. For example, ~92 eV (~13.5 nm) photons are being paid much attention to because of the existence of high-quality EUV mirrors based on Mo/Si multilayer coatings [8]. This short wavelength radiation is intensively pursued for next-generation EUV lithography as well as seeding of free electron lasers and x-ray lasers. High-flux EUV sources can greatly help attosecond metrology mostly utilizing photoelectron time-of-flight spectrometers that require hours of acquisition due to the limited number of photons per shot currently available. To quantitatively confirm the effectiveness of HHG-based high-efficiency EUV sources, we experimentally study HHG in Ar, Ne, and He gases using a 2-mm-long pulsed gas jet with 400-nm and 800-nm driver pulses.

For the experiments at two different driver wavelengths [9], we used 1-kHz, 800-nm, 35-fs driver pulses with pulse energies up to 5-mJ, and 400-nm driver pulses obtained via second harmonic generation (SHG) in a 150- $\mu$ m-thick beta-barium borate (BBO) crystal. The 800-nm pulses were focused into the gas jet to a spot with a beam waist of 40  $\mu$ m (1/e radius of the electric field) focused by a spherical mirror with 100-cm focal length. The BBO crystal was placed between the focusing mirror and the gas jet for SHG and the remaining 800-nm pulse was removed by two dichroic mirrors. We obtained 1-mJ pulses centered at 400 nm with 18-nm of bandwidth that were focused into the gas jet to a spot with a beam waist of ~30  $\mu$ m. The estimated duration of the 400-nm pulses was 26 fs corresponding to 18 optical cycles.

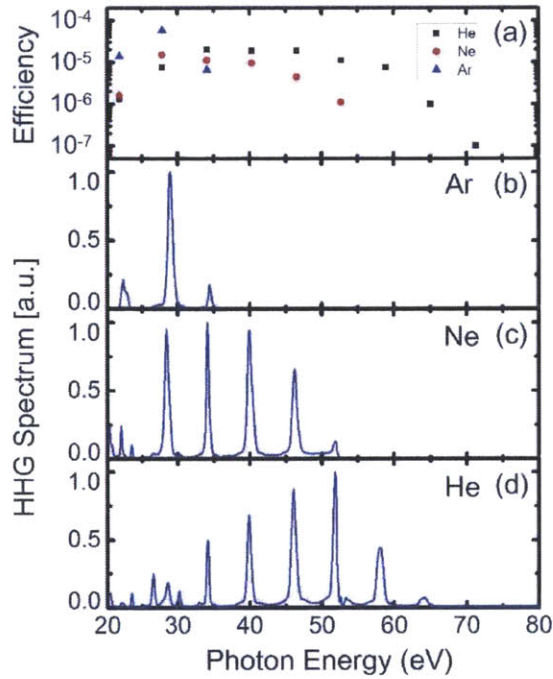


Fig. 4-1 HHG driven by 400-nm wavelength, 1-mJ, 26-fs driver pulses: (a) conversion efficiencies for Ar, Ne, and He using a 2-mm gas jet positioned 1 cm before the focus for Ar and at the focus for Ne and He; (b), (c), (d) HHG spectra respectively for Ar, Ne and He.

The HHG efficiencies and spectra obtained using 400-nm driver pulses in Ar, Ne and He are summarized in Fig. 4-1. The laser peak intensity at the focus is estimated to be  $\sim 2.7 \times 10^{15}$  W/cm<sup>2</sup> for the 1mJ pulse. Fig. 4-1 (a) shows the conversion efficiency into a single harmonic order measured using a calibrated x-ray detector (AXUV100, IRD, Inc.) for the Al-filter transmission range (20-70 eV). The observed conversion efficiencies at the cutoff for the different gases are around  $1 \times 10^{-5}$  at 34 eV for Ar,  $1 \times 10^{-6}$  at 53 eV for Ne, and  $1 \times 10^{-7}$  at 71 eV for He, respectively. The backing pressures of the pulsed gas jet are 50 mbar, 300 mbar, and 2 bar for Ar, Ne, and He respectively. The corresponding high harmonic spectra from Ar, Ne, and He, used for efficiency calculations, are shown in Fig. 4-1 (b)–(d), respectively. Peak efficiencies of almost  $1 \times 10^{-4}$  at 28 eV are reached for Ar,  $1 \times 10^{-5}$  at 28 eV for Ne, and  $1 \times 10^{-5}$  at 53 eV for He.

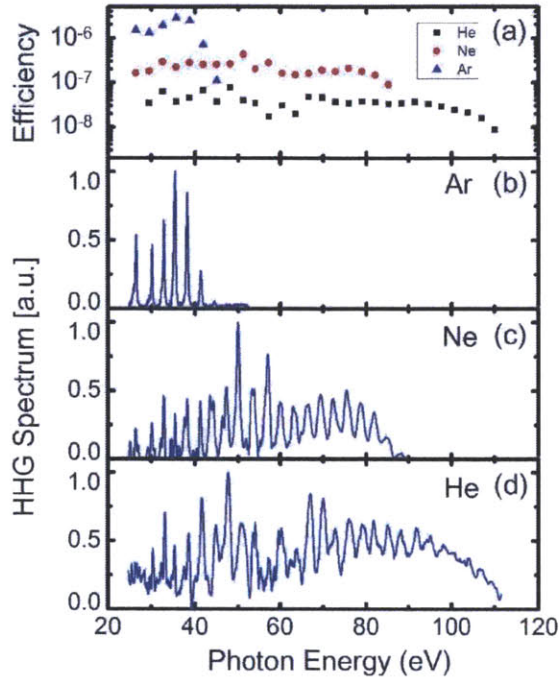


Fig. 4-2 HHG driven by 800-nm wavelength, 35-fs driver pulses: (a) conversion efficiencies for Ar (0.6 mJ), Ne (2.0 mJ), He (2.0 mJ) using a nozzle length  $L = 2$  mm positioned 1 cm before the focus for all the gases; (b), (c), (d) HHG spectra respectively for Ar, Ne and He.

Fig. 4-2 summarizes the HHG conversion efficiencies and corresponding spectra in the range of 20-110 eV driven by 800-nm, 35-fs pulses with energies of up to 2 mJ. Fig. 4-2 (a) is obtained from the efficiency measurements for the low energy range (20-70 eV) covering the Al-filter transmission window and high energy range (60-110 eV) covering the Zr-filter transmission window. Different backing pressures of 50 mbar, 300 mbar and 2 bar are used for Ar, Ne and He, respectively, and the laser peak intensity at the focus is  $\sim 2.3 \times 10^{15}$  W/cm<sup>2</sup> with 2mJ pulses ( $\sim 6.8 \times 10^{14}$  W/cm<sup>2</sup> for 0.6 mJ). The efficiencies at the same EUV wavelength are about 2-3 orders of magnitude lower for the 800-nm driver pulses in comparison with the 400-nm driver pulses, but the cutoff energy is considerably increased to beyond 100 eV for He. As can be observed from Fig. 4-2 (a), the HHG

conversion efficiency at the cutoff is reduced to  $1 \times 10^{-7}$  at 45 eV for Ar,  $1 \times 10^{-7}$  at 88 eV for Ne and  $1 \times 10^{-8}$  at 110 eV for He.

In the entire experiment, the HHG efficiency optimization is achieved by scanning gas pressure, nozzle position, and laser energy. For Ar the nozzle position is  $\sim 7$  mm before the focus for both 400-nm and 800-nm drivers, whereas for Ne and He the nozzle is positioned at the focus for both wavelengths. However, the HHG efficiency is not very sensitive to the nozzle position within the Rayleigh range ( $\sim 6.3$  mm for 800 nm and  $\sim 7.1$  mm for 400 nm) before focus. The energy dependence of the total efficiencies achieved with He over the full Al window are shown in Fig. 4-3 (a) for 400 nm and Fig. 4-3 (b) for 800 nm pulses, respectively. This conversion efficiency is obtained directly from the XUV diode photocurrent, multiplied by quantum efficiency and divided by Al-filter transmission and driver energy. The transmission and quantum efficiency at the center wavelength of the Al window are used to compute the total efficiency. Thus, these efficiency plots are not spectrally calibrated, unlike Fig. 4-1 and Fig. 4-2, but show the relative conversion efficiency versus laser intensity. Fig. 4-3 indicates that significant conversion starts at an intensity of few times  $10^{14}$  W/cm<sup>2</sup> and saturates for  $>10^{15}$  W/cm<sup>2</sup>. This saturation is also observed for Ar and Ne starting at lower intensities. It is interesting that good conversion efficiencies can be obtained for peak intensities of  $>10^{15}$  W/cm<sup>2</sup> at which the ionization becomes substantial. This is attributed to spatial effects of the beam. First, the HHG efficiency is high in the center of the beam and then the high-efficiency region becomes an annulus around the center shifting into the wing of the Gaussian beam for increase in efficiency, leaving the overall efficiency achieved roughly equal. Second, the beam size is increased at higher intensity ( $>10^{15}$  W/cm<sup>2</sup>) due to the plasma-induced self-defocusing [55].



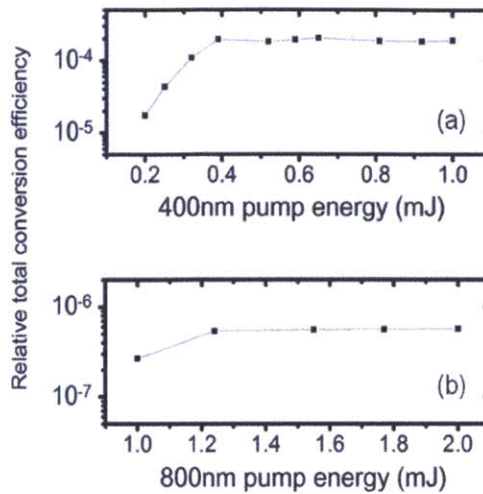


Fig. 4-3 Relative total conversion efficiency in He versus laser peak intensity with (a) 400-nm and (b) 800-nm drivers over Al window. This is obtained by  $(\text{XUV diode photocurrent} \times \text{quantum efficiency}) / (\text{transmission of Al filter} \times \text{pulse energy})$ , where the quantum efficiency and transmission at the center of the Al window are used.

In summary, we present an experimental study of HHG with short 400-nm and long 800-nm wavelength driver pulses. When all of the macroscopic parameters are optimized, the single harmonic efficiency of 400-nm driver pulses are almost three orders of magnitudes higher than the 800-nm driver pulses, higher than the difference from the SE. This is because the phase-matching process is much easier for shorter driver wavelengths, and the plasma dispersion also has less impact on the short wavelength pulses. Therefore, a coherent EUV source based on HHG driven by visible wavelengths is promising [9].

#### 4.2 Cutoff of HHG Spectrum in the EUV Regime with Visible Driver Wavelengths

In last section, we have demonstrated that the visible drivers are particularly suited for the generation of high-flux EUV radiation, because of the higher conversion efficiencies than IR drivers. Besides, the cutoff energy falls within the optimal range for the free-electron laser (FEL) seeding makes HHG driven by visible wavelengths a potential FEL seeding source [7]. As previously discussed, the improvement of the conversion efficiency is at the



expense of the cutoff energy. Therefore, in this section, we study the cutoff of the HHG spectra because it is related to limit of the application scope. We present experimental results utilizing an OPA system whose signal wavelength is tunable between 470 nm and 640 nm [66]. The visible pulses from the OPA are focused into a He gas jet to experimentally study the scaling laws for the cutoff energy of HHG, extending the results from the IR to the visible wavelengths range.

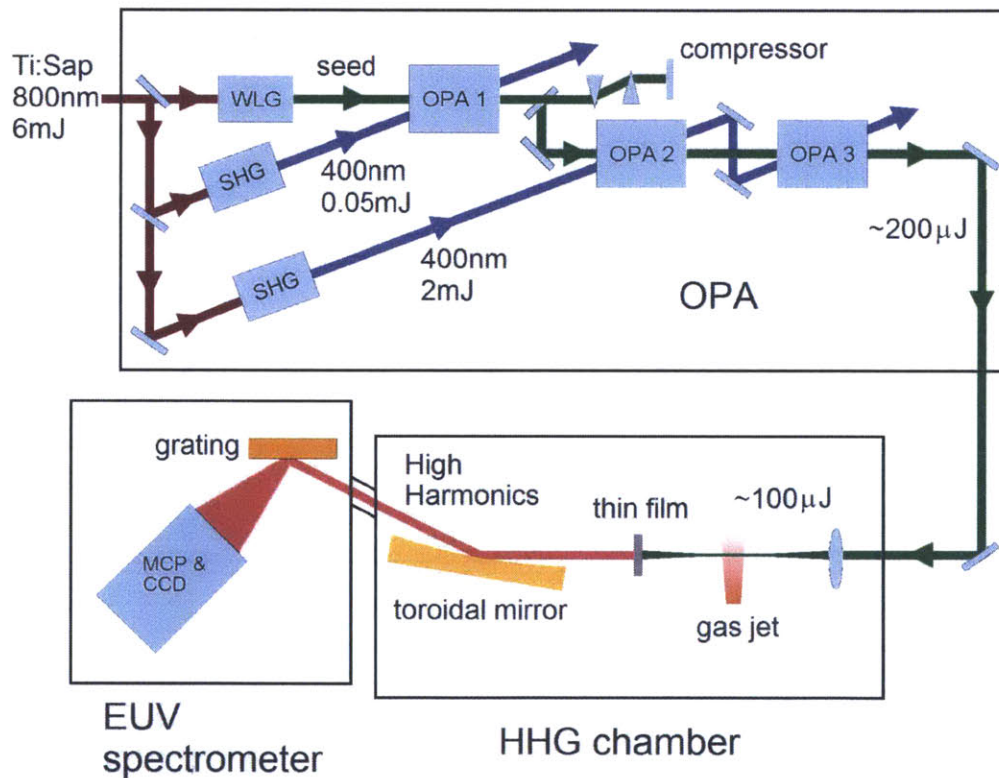


Fig. 4-4 Schematic of the experimental setup, composed of a three-stage OPA pumped by a commercial Ti:sapphire amplifier, the HHG setup, and an EUV spectrometer. WLG: white light generation; MCP: microchannel plate; CCD: charge-coupled device.

Fig. 4-4 shows the experimental setup. We built a three-stage OPA [66] from a commercial chirped pulse amplification system that delivered 1-kHz, 35-fs, 6-mJ pulses with 800-nm central wavelength. The signal of the three-stage OPA that would drive the

HHG could be continuously tuned between 470 nm and 650 nm (Fig. 4-5 (a)) by rotating the phase matching angle of the BBO at OPA 1. The pulse energy within the tuning range was  $\sim 200 \mu\text{J}$  and the pulse duration was 34~39 fs as measured by self-diffraction method with a 0.15-mm-thick BBO (Fig. 4-5 (b)) [67]. The beam quality was good with an  $M^2$  value of 1.9, as shown in Fig. 4-5 (c). The driver pulse was then delivered into the vacuum chamber to generate HH with a pulsed gas jet. The generated HH was refocused by a toroidal mirror into the spectrometer equipped with a microchannel plate (MCP), as shown in the lower part of Fig. 4-4. The gas jet was generated by a piezoelectric pulsed valve synchronized with the laser system at 1 kHz. After the HHG process, the residue driver pulse was filtered out by a 0.5- $\mu\text{m}$ -thick Al or Be thin film that transmit 20-70 eV and 50-110 eV respectively.

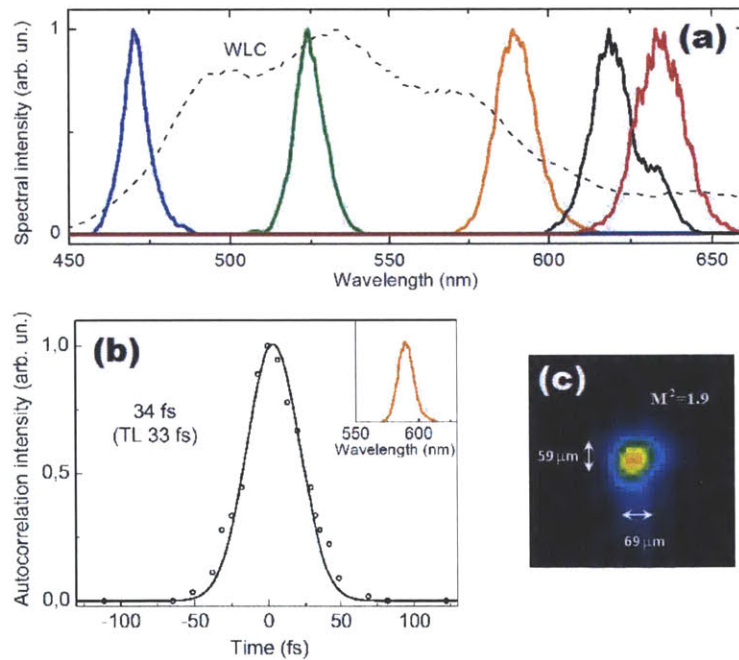


Fig. 4-5 (a) OPA spectra of the signal with different center wavelengths. The white light continuum (WLC) spectrum is also shown as a dashed line. (b) The pulse duration measurement of one of the OPA signal. The measured pulse duration (34 fs) is close to the transform limited (TL) pulse duration (33 fs) calculated from the spectrum. (c) CCD image of the OPA signal focused with a 25-cm focusing lens.

Because He has the highest ionization potential and therefore the highest cutoff, we study the HHG from a He gas jet using the OPA. Fig. 4-6 (a) shows the HHG spectra obtained with four different driver wavelengths. Fig. 4-6 (b) shows the experimental cutoff as green squares, while the blue dashed line shows the linear fitting curve on logarithmic scale ( $\lambda^{1.7\pm 0.2}$ ), which stays within the range of the phase-matched cut-off relation ( $\lambda^{1.4-1.7}$ ) observed in the IR region [12,57]. The absolute value of the cutoff energy is difficult to optimize due to the low energy of the OPA driver pulses. The pulse energy available at the gas jet is about 120  $\mu\text{J}$ , and the OPA pulses has to be focused tightly to reach an intensity high enough to observe a HHG signal. Such a tight focus has the drawback of poor phase matching due to the Gouy phase and limited interaction volume within the medium.

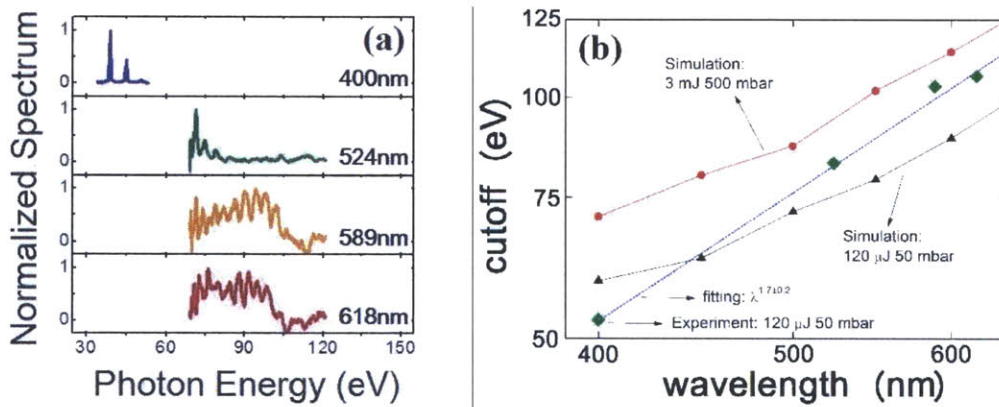


Fig. 4-6 (a) Experimental HHG spectra from He gas jet driven by different wavelengths. (b) Wavelength scaling of HHG cutoff in He. Green squares: experimental data; blue dashed line: linear fit on logarithmic scale; black triangles: simulation with the experimental parameters; red circles: simulations with higher pulse energies and medium pressure to avoid phase-mismatching from the Gouy phase.

To show the cutoff energy improvement with higher pulse energies, we numerically study HHG by applying the fully dimensional simulation introduced in Section 3.3. Fig. 4-6 (b) shows the simulation of the cutoff energy at the experimental conditions (black triangles) and the simulation with much higher pulse energy and medium pressure to avoid

the adversary phase-mismatch from the Gouy phase (red circles). The simulations show that with more pulse energy than possible with the current OPA, higher cutoff energies are reachable. This happens because one can use higher peak intensities without focusing the driver pulses tightly. Phase-matching, which is particularly critical for higher energy photons, also becomes easier with looser focusing due to a lower Gouy phase. As shown in last section, the experimental cutoff of 400-nm driver is 71 eV with higher pulse energy (1 mJ). In this work, the cutoff scaling of HHG is investigated with a continuously tunable OPA at low pulse energy.

Because of the low driver energy, the single harmonic conversion efficiency in the plateau region is only  $\sim 10^{-9}$ , corresponding to  $\sim 10^4$  photons/shot at 100 eV, from the 589-nm driver wavelength. To show the improvement in efficiency with higher pulse energies, we simulate the efficiency for three different He gas jet pressures, as shown in Fig. 4-7. In the simulation, the total efficiency between 80 eV and 90 eV for a 589-nm driver pulse is compared. The pulse duration is the same as in the experiments, 34 fs, and the peak intensity is fixed at  $7.7 \times 10^{14}$  W/cm<sup>2</sup> (same as the experimental value) by changing the beam size accordingly. Fig. 4-7 shows that, as the pulse energy increases from 120  $\mu$ J to few mJ, the simulated efficiency improves by 2 or 3 orders of magnitude due to the loose focusing and the longer interaction length (up to  $10^{-(6-7)}$  in the example considered here). Before reaching the asymptotic value, the efficiency curves show some oscillatory behavior due to phase-matching effect. Further optimization of the gas jet position in the simulation may result in efficiencies higher than those shown in Fig. 4-7, but this doesn't affect the main conclusion that a looser focusing can help phase-matching and give an improvement by a few orders of magnitudes.

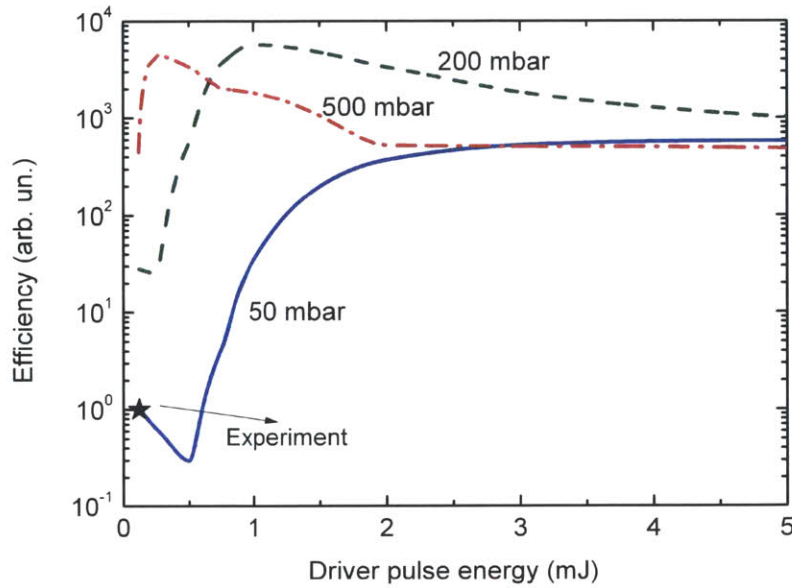


Fig. 4-7 The calculated HHG efficiencies in helium for different driver pulse energies and different pressure values show that one can improve the efficiency by several orders of magnitudes by using more energetic driver pulses.

The cutoff of HHG in He driven by visible wavelengths is studied because of the interest in efficient HHG with shorter driver wavelength. A  $\lambda^{1.7 \pm 0.2}$  experimental scaling law of the cutoff is obtained, which can be an important guideline for choosing the driver wavelength for a given photon energy. As shown by the simulation, the cutoff can be further extended by increasing the driver pulse energy to the mJ level, and the efficiency can be enhanced to around  $10^{-(4-6)}$ , which is sufficient for the seeding of an EUV free electron laser.

### 4.3 Wavelength-Scaling of Single-Atom Efficiency

The wavelength scaling of HHG SE is important not only for building an efficient laser source, but for understanding the physics of HHG itself. Although there have been many theoretical works and experiments devoted to the wavelength scaling of HHG SE using IR driver wavelength, the scaling with shorter driver wavelengths in the visible regime has not been systematically explored yet. For driver wavelengths shorter than 800nm, the scaling



has been studied by comparing the efficiencies with one near-IR driver wavelength and its second harmonic [5,9,47]. Although the second harmonic shows a dramatic enhancement of HHG efficiency, a systematic experiment employing more wavelengths is still necessary to experimentally map out the detailed wavelength scaling. Therefore, the OPA system presented in last section with signal wavelengths tunable in the visible range serves as an excellent tool to study the wavelength scaling of HHG SE.

A fundamental difference between HHG driven by IR and visible wavelengths is the ionization process, which can be distinguished by the Keldysh parameter  $\gamma$  (cf. section 2.4). In the TSM discussed in Section 2.2, the solution of the Schrödinger equation is expanded around  $\gamma = 0$ , and gives the useful formula for HHG dipole moment Eq. (2.35). However,  $\gamma$  is rarely much smaller than one in many HHG experiments. When  $\gamma$  is considered, it has been shown that the ionization time at which an electron exits the atomic potential barrier is slightly advanced from the semi-classical model [49]. Since the ionization time can influence the HHG efficiency through quantum diffusion [17,32], this can lead to different HHG characteristics. To study this difference, visible driver wavelengths are more suitable than IR because  $\gamma$  is higher for shorter wavelengths at a given intensity. The effect due to non-negligible  $\gamma$  has been discussed in Section 2.4, where the theory shows good agreement with HHG experiment performed around  $\gamma \approx 1$ . In this section, the detail of the HHG experiment will be presented.

As shown in Section 3.2 and Section 4.1, the macroscopic experimental conditions have to be carefully controlled in order to extract the information of the SE without the interference from macroscopic factors [42]. The total yield of the  $q^{\text{th}}$  harmonic can be expressed as [43]:

$$S_q = C \int d\tau \int 2\pi r dr \left| \int_{-L/2}^{L/2} dz \zeta \rho \exp(iz\Delta k_q) \exp\left[-\frac{\rho\sigma}{2}(L-z)\right] \right|^2, \quad (4.1)$$

where  $C$  is a proportional constant;  $\tau$  is the time in the co-moving frame of the driver pulse;  $r$  is the radial coordinate;  $z$  is the propagation direction;  $\zeta$  is the SE;  $\rho$  is the medium density;  $L$  is the medium length;  $\Delta k_q$  is the wave-vector mismatch;  $\sigma$  is the absorption cross-section of the harmonic. To directly relate the measured yield  $S_q$  to the SE, we need to fix all of the parameters in Eq. (4.1) except  $\zeta$ . Therefore, the driver pulses must have the same pulse duration and focal beam waist. With the same pulse energy, the peak intensity is fixed as well. We also need to make the HHG phase-matched by keeping  $\Delta k_q L < \pi$ .

In the experiment, the driver wavelengths included three visible wavelengths from our OPA system (Fig. 4-4) and 800nm from the Ti:sapphire amplifier. The OPA signal was continuously tunable between 470 and 650 nm with 34-39-fs pulse duration, similar to the 35-fs pulse duration of the 800-nm pulse. We fixed the focal beam waists at  $26 \pm 2 \mu\text{m}$  by controlling the entrance iris before the focusing lens and measured the beam waists by the knife edge method. The similar temporal and spatial conditions of these driver pulses minimized the difference in the temporal and radial integrals in Eq. (4.1). The pulse energies were  $\sim 90 \mu\text{J}$  at the focus, corresponding to a peak intensity of  $(2.7 \pm 0.2) \times 10^{14} \text{ W/cm}^2$ . The corresponding Keldysh parameters were 0.7-1.1. The HHG medium was an Ar jet from an exit orifice with 1mm diameter. Characterized by a Mach-Zehnder interferometer, the Ar density was  $3 \times 10^{18} \text{ cm}^{-3}$ . The HH signals were detected by an EUV spectrometer equipped with an MCP.

In addition to the driver pulse conditions, another important macroscopic aspect is phase-matching. Fortunately, phase-matching is much easier to achieve for shorter driver

wavelengths because of the lower harmonic order and the smaller Gouy phase [45]. The phase-mismatch for a multi-cycle driver pulse may result from the neutral atom dispersion, the plasma dispersion, the Gouy phase, and the dipole phase [45,55,68]. With moderate peak intensities in the experiment, the neutral atom dispersion and the plasma dispersion were roughly balanced, and the residual phase-mismatch was mainly due to the Gouy phase, which could be cancelled by placing the gas jet behind the laser focus to induce an appropriate amount of dipole phase [56]. To achieve phase-matching, we selected the short trajectory by scanning the gas jet position and maximizing the target HH signal. To check phase-matching, we measured the pressure dependence of the 21<sup>st</sup> harmonic of the 800-nm driver wavelength, which was the highest harmonic order in our experiment and therefore the most difficult one for phase-matching. As shown in Fig. 4-8 (a), when the pressure was low, the HH signal showed a quadratic dependence on the medium pressure. Thus, we ensured phase-matching between the HH and the driver pulse within the interaction length.

After controlling the macroscopic parameters and optimizing the phase-matching, we can directly relate the measured HH signal to the SE. We compare the 13<sup>th</sup>, 15<sup>th</sup>, 17<sup>th</sup>, and 21<sup>st</sup> harmonics of the 524, 589, 633, and 800-nm driver wavelengths respectively. All of these harmonics have similar photon energy at around 32 eV, as shown in Fig. 4-8 (b). We calculate the total HH yield within each specific harmonic peak by integrating the spectrum over the  $\pm\omega_0$  neighborhood of the peak, where  $\omega_0$  is the driver frequency. The HHG efficiency of each specific harmonic peak is plotted in Fig. 4-8 (c), and shows a wavelength scaling of  $\lambda^{-(4.7\pm 1.0)}$ , less dramatic than the  $\lambda^{-(7-8)}$  scaling observed with IR driver wavelengths. We attribute this difference to the larger Keldysh parameter and the deviation from a pure tunneling process, as has been explained by our modified TSM in Section 2.4.



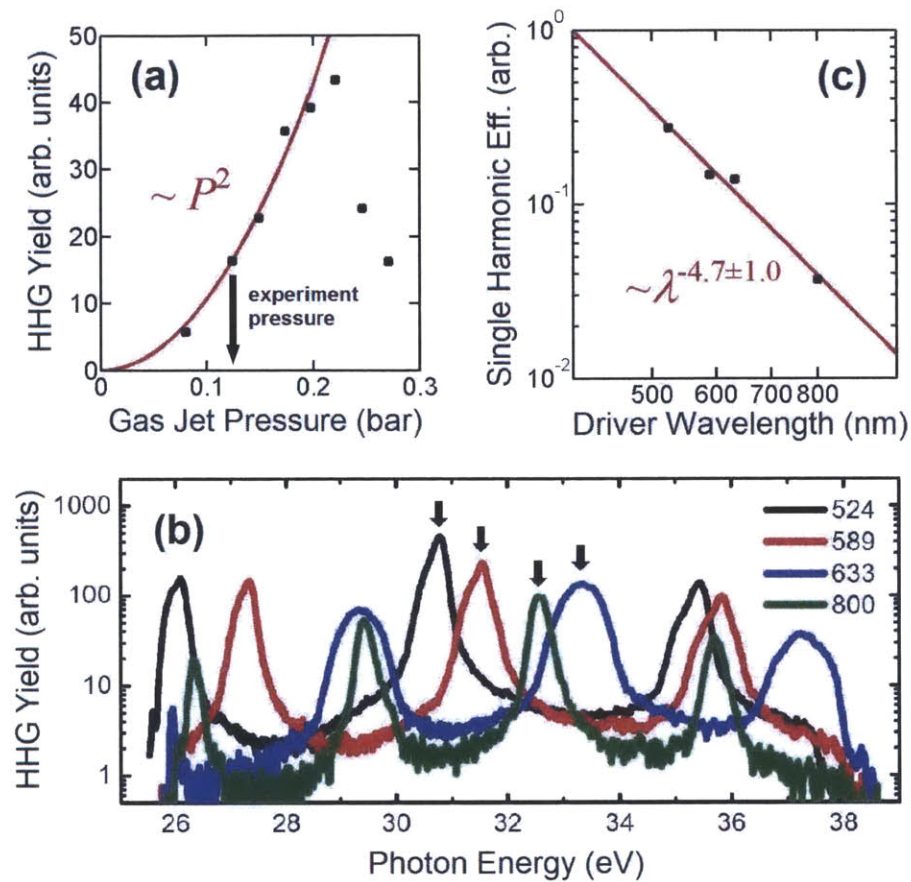


Fig. 4-8 (a) The pressure dependence of the 21<sup>st</sup> harmonic of the 800-nm driver pulse. The arrow indicates the pressure set in the wavelength scaling experiment for the other driver wavelengths. (b) The HHG experiment spectra, where the arrows indicate the optimized phase-matched harmonics to compare. (c) The integrated signal of the individual harmonics indicated by the arrows in (b).

#### 4.4 Conclusion

This chapter discusses several experimental projects done with the Ti:sapphire amplifier with an emphasis on the study of HHG driven by visible driver wavelengths. The wavelength scaling of HHG SE shows a significant enhancement of efficiency with shorter driver wavelength. The enhancement becomes even more dramatic because of several macroscopic effects including the higher ionization level, lower harmonic order, smaller Gouy phase, and easier phase-matching. After optimizing the experimental conditions, we show almost three orders of magnitudes of efficiency enhancement in He when the driver

wavelength changes from 800 nm to 400 nm. This improvement in efficiency will make HHG a much more promising EUV source for <100 eV applications.

Pumped by the second harmonic of the Ti:sapphire amplifier, an OPA with tunable signal wavelength between 470 and 650 nm,  $\sim 200 \mu\text{J}$ , 34-39-fs pulse duration is built to study HHG driven by visible wavelengths. With careful control of the macroscopic experiment conditions as well as the phase-matching, we measured the wavelength scaling of the HHG SE in Ar at 32 eV, and observed a less dramatic scaling relation  $\lambda^{-4.7 \pm 1.0}$ , as compared to the  $\lambda^{-(7-8)}$  scaling of single harmonic efficiency derived by the conventional TSM. This discrepancy has been explained by our modified TSM in Section 2.4. The cutoff in He is roughly between 60 eV and 100 eV as the driver wavelength increases from 400 nm to 618 nm, and a wavelength scaling law of  $\sim \lambda^{1.7 \pm 0.2}$  is observed. Because the pulse energy is small, and tight focusing is required to reach the necessary intensity, the phase-matching condition is poor and decreases the cutoff. The numerical simulation shows that with multi-mJ energy, the cutoff can be extended by  $\sim 20$  eV, and the efficiency can be improved by several orders of magnitudes, as already observed by our experiment with 1-mJ 400-nm driver pulse. The tunable signal wavelength makes the HH energy continuously tunable, which makes our OPA useful for seeding FEL in the <100-eV range.

# Chapter 5

## High Harmonic Generation Driven by Mid-Infrared Ultrashort Pulses

In order to extend the cutoff of HHG further into the soft X-ray regime, longer driver wavelengths in the mid-infrared are considered according to the cutoff scaling law Eq. (1.3). However, the wavelength scaling law of the HHG SE also predicts a poor efficiency for longer driver wavelengths, so high repetition rate and high pulse energy mid-IR becomes necessary to generate a reasonable HHG photon flux for applications. OPCPA, given its potential to scale up the pulse energy, is the best candidate for such high power mid-IR source. Section 5.1 shows our kHz, multi-mJ, 2.1- $\mu\text{m}$  OPCPA system. To achieve multi-mJ pulse energy in OPCPA, a high energy picosecond pumping source is indispensable, and Section 5.2 shows the cryogenic Yb:YAG pumping system that can generate 56-mJ, 17-ps pulse at 1.03  $\mu\text{m}$ . The multi-mJ 2.1- $\mu\text{m}$  pulse is focused into a gas cell with Ar or Ne to generate HH. Section 5.3 shows the HHG result.

### 5.1 Optical Parametric Chirped Pulse Amplification

HHG driven by mid-IR wavelength has been proven to be the most reliable way achieving tabletop water-window soft X-ray [10,12] or even keV source [69]. The extended cutoff

provides new opportunities in attosecond pump-probe studies, high-harmonic spectroscopy, recollision physics, selective X-ray spectroscopy, and biological or nanoscale imaging applications. However, the unfavorable wavelength scaling of the HHG SE (cf. Section 2.3) makes high-flux HHG extremely difficult with the mid-IR driver wavelength. Although the much smaller reabsorption at high photon energy allows the use of high density medium to compensate for the poor SE, the plasma defocusing effect (cf. Section 3.2) becomes a serious issue in high density medium. Recently, phase-matched HHG covering the water window range with an efficiency of  $\sim 10^{-(8-9)}$  has been experimentally demonstrated in Ne and He [10,12] using 10-Hz, multi-mJ OPA sources pumped by a Ti:sapphire laser. However, the photon flux is only  $10^6$  photons per second over 1% bandwidth while an imaging application would require a flux two orders of magnitudes higher than this number [70]. OPA [71] and OPCPA [72] with sub-mJ pulse energy at kHz repetition rate have been reported and show cutoff up to  $\sim 300$  eV. However, the photon flux has not been reported. Therefore, multi-mJ driver pulse energy and kHz repetition rate are keys to achieving high photon flux HHG in the soft X-ray range.

OPCPA is considered one of the most promising mid-IR driving sources for HHG because of the broadband amplification that can support few-cycle pulses and the high energy scalability at high repetition rate [73]. The basic idea of OPCPA is to amplify a chirped seed pulse by OPA pumped by a high energy picosecond pulse, and then compressed the amplified chirped pulse back to the short duration [74]. Compared to the chirped pulse amplification (CPA) technique, OPCPA has several advantages: tunable central wavelength, broader amplification bandwidth, higher single-pass-gain to reduce the B-integral, low amplified spontaneous emission, good amplified beam quality, low thermal effects due to no population inversion [75]. Thanks to the rapid progress in the development of high power picosecond pulse technology [76-78], high energy pump

becomes available for OPCPA to scale up the signal pulse energy and generate high flux HH. This section will introduce our OPCPA system.

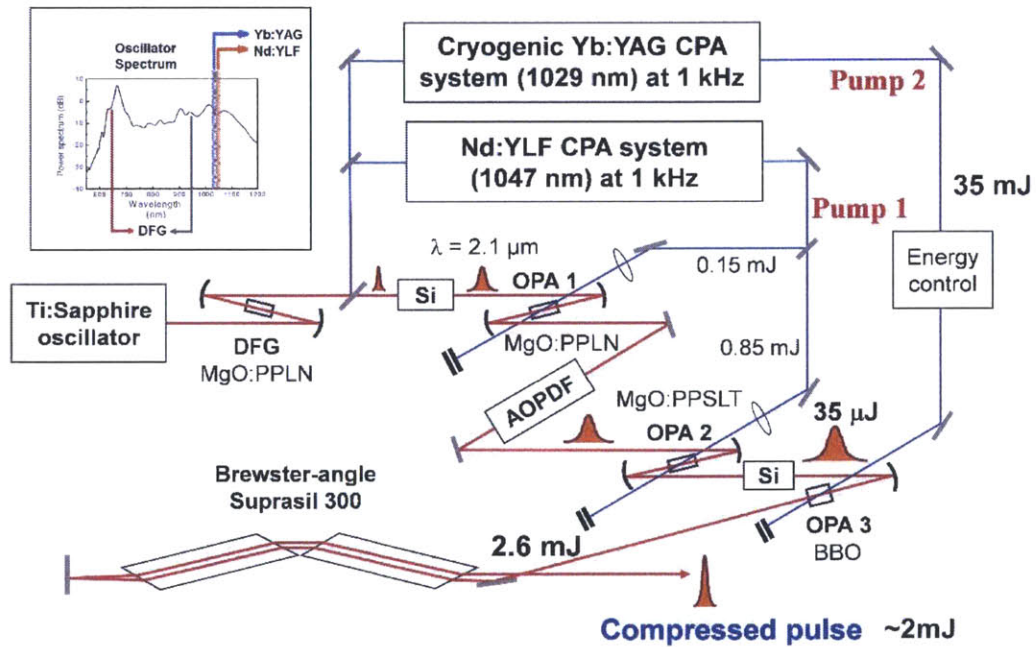


Fig. 5-1 Optical layout of the ultrabroadband 2.1- $\mu\text{m}$  three-stage OPCPA system. The inlet shows the octave-spanning spectrum of the oscillator and the usages of the spectral components.

The OPCPA system is shown in Fig. 5-1. The Ti:Sapphire oscillator first generates an octave-spanning spectrum covering 600-1200 nm from which the 650-nm and the 940-nm portions of the oscillator spectrum are mixed in a MgO-doped periodically poled lithium niobate (MgO:PPLN) to generate  $\sim\text{pJ}$  ultrabroadband ( $\sim 500 \text{ nm}$  at  $-10\text{dB}$ ) seed pulses with central wavelength at  $2.1 \mu\text{m}$  by difference frequency generation (DFG). The 1047-nm and the 1029-nm portions of the oscillator spectrum are sent to the Nd:YLF CPA system and the cryogenic Yb:YAG CPA system respectively to amplify and are then used as the pumps of the three OPCPA stages later. After the DFG stage, the seed pulse is stretched to  $\sim 5 \text{ ps}$  by an anti-reflection (AR) coated 30-mm-long Si block and amplified to  $\sim 2 \mu\text{J}$  in

OPA1 that is pumped by the 1047-nm, 0.15-mJ, 12-ps pulses from the Nd:YLF system. After OPA1, the seed is further stretched to  $\sim 9$  ps by an acousto-optic programmable dispersive filter (AOPDF; Dazzler, Fastlite) before being amplified in OPA2. OPA2 is also pumped by the Nd:YLF system with 0.85-mJ, 12-ps 1047-nm pulses. The seed is amplified to  $\sim 35$   $\mu\text{J}$  by OPA2. Ultrabroadband amplification is achieved by means of a degenerate OPA in periodically poled lithium niobate (MgO:PPLN) and periodically poled stoichiometric lithium tantalite (MgO:PPSLT) crystals. The details of the first two OPCPA stages are described in Ref. [74].

The  $\sim 35$ - $\mu\text{J}$  pulse from OPA2 is further stretched to  $\sim 17$  ps with an AR coated 50-mm-long Si block and then amplified in a 5-mm-long type-I BBO crystal pumped by 35-mJ, 17-ps, 1029-nm pulses from the cryogenic Yb:YAG system, which will be discussed in next section. The beam sizes of both seed and pump pulses are adjusted independently by telescopes to minimize the superfluorescence. At optimal performance, the seed energy is amplified to 2.6 mJ at OPA3 with a gain of  $\sim 10^2$  at a pump intensity of 30~50  $\text{GW}/\text{cm}^2$ . A beam pointing stabilizer for the Yb:YAG pump beam is installed to actively stabilize beam pointing at the BBO crystal due to air fluctuation along the beam path. As a result, the pump-beam position fluctuation is  $\sim 70$   $\mu\text{m}$  over  $\sim 3.0$  mm of beam diameter at the BBO crystal. The spectral bandwidth of the amplified pulses is 407 nm at FWHM centered at 2.1  $\mu\text{m}$ , as shown in Fig. 5-2 (a).

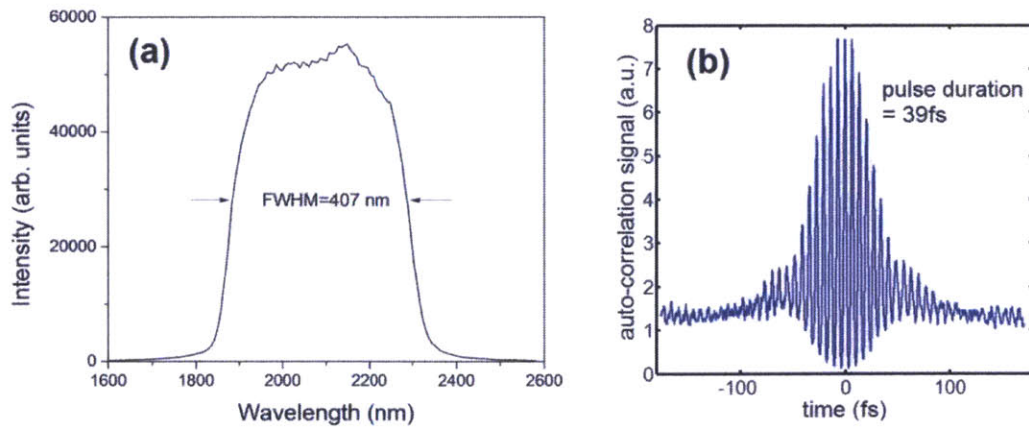


Fig. 5-2 (a) The spectrum of the multi-mJ 2.1- $\mu\text{m}$  pulse. (b) The autocorrelation measurement of the pulse duration of the multi-mJ 2.1- $\mu\text{m}$  pulse.

The multi-mJ 2.1- $\mu\text{m}$  pulse is then compressed by two Brewster-angled Suprasil 300 blocks with a total path length of 620 mm near the HHG chamber. The compressed pulse duration is 39 fs, measured by an interferometric autocorrelator (Fig. 5-2 (b)), while the transform-limited pulse duration is 29 fs. The compression efficiency including loss in the delivery optics (7 silver mirrors) between OPA3 and the HHG chamber is  $\sim 80\%$ , and the maximum energy available for the HHG experiment is  $\sim 2$  mJ. The carrier-envelope phase (CEP) of the 2.1- $\mu\text{m}$  pulses is passively stabilized [74] although the stability is not measured because of the relatively long pulse duration of  $\sim 6$  cycles, making CEP effects negligible in the HHG process.

## 5.2 Cryogenic Yb:YAG System

The promising energy scaling toward high repetition rate in the kHz regime of OPCPA heavily relies on a high power picosecond pump source [78]. Therefore, new high power picosecond sources based on Yb:YAG gain medium at 1029 nm have been explored. A thin-disk Yb:YAG amplifier with 3-kHz repetition rate, 25-mJ pulse energy, and  $\sim 1$ -ps pulse duration has been reported [76], and recently enabled the generation of 1.2-mJ,

2.1- $\mu\text{m}$  OPCPA pulses [79]. The amplification to more than 40-mJ pulse energy at 1029 nm from the Yb:YAG thin-disk amplifiers have also been reported very recently [77]. Yb:YAG is an excellent candidate of high power picosecond laser gain medium because of several favorable properties: broad absorption band at 940 nm and long upper-state life time support accumulation of substantial population inversion pumped by high-power laser diode; high thermal conductivity helps prevent optical damage due to thermal lensing; low quantum defect (9%) leads to high conversion efficiency and low thermal load. The main drawback of Yb:YAG is the high saturation fluence at room temperature ( $\sim 9 \text{ J/cm}^2$ ), which can be lowered by cryogenically cooling and transforming Yb:YAG from a quasi-three-level system to a four-level system [78]. The cryogenic temperature also further improves the thermal optical property of Yb:YAG. In this section, we will present our cryogenic Yb:YAG system that delivers 17-ps pulses with  $>50\text{-mJ}$  pulse energy at 1029 nm central wavelength to pump OPA3 in Fig. 5-1.



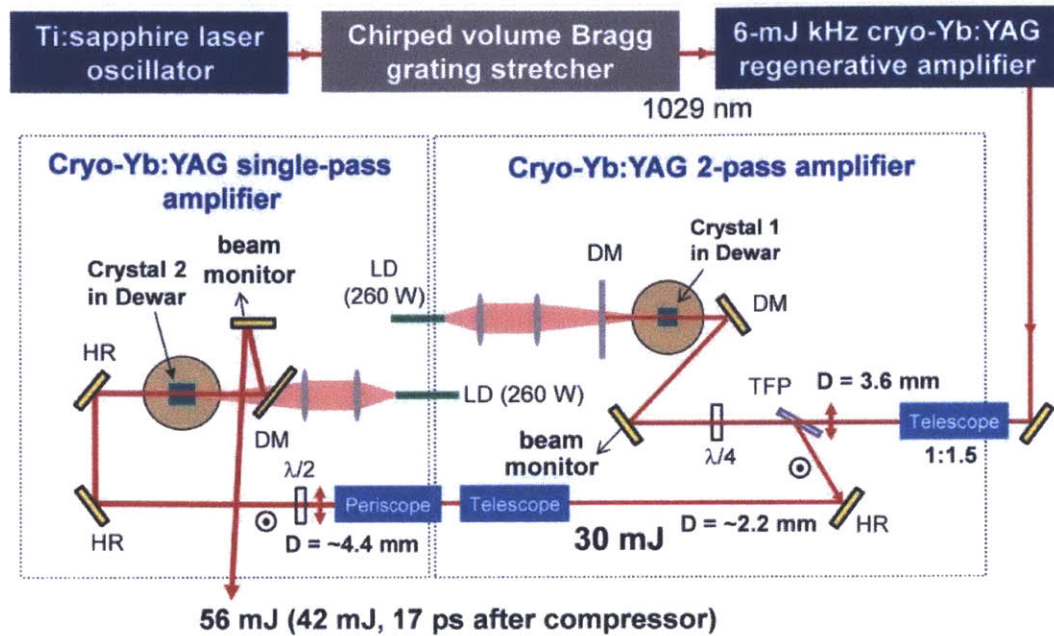


Fig. 5-3 Optical layout of the kHz picosecond cryogenic Yb:YAG CPA laser. Crystal 1, 1%-doped, 10-mm-long Yb:YAG; Crystal 2, 2%-doped, 20-mm-long, Yb:YAG; D, diameter; HR, high reflector; DM, dichroic mirror; TFP, thin-film polarizer;  $\lambda/2$ , half waveplate;  $\lambda/4$ , quarter waveplate; LD, laser diode at 940 nm.

The system layout of the cryogenic Yb:YAG CPA laser system is illustrated in Fig. 5-3. The 1029-nm portion from the spectrum of the same Ti:sapphire oscillator that seeds the OPCPA system is pre-amplified by two Yb-doped fiber amplifiers, stretched by a chirped volume Bragg grating (CVBG) pair to  $\sim 560$  ps with 0.7-nm bandwidth, and then amplified by a kHz regenerative amplifier to 6 mJ. After magnified by a telescope in beam size, the 6-mJ pulse is then sent to a two-pass amplifier whose gain medium is a 1%-doped 10-mm-long Yb:YAG crystal attached tightly to a Dewar cooled by liquid nitrogen to 77 K. The telescope at the entrance plays an important role to control the beam size to match the pump beam size for optimal performance of amplification and to avoid self-focusing triggered by the amplified intense pulse. The self-focusing effect should be minimized to preserve the good spatial quality as well as to protect the optics. The Yb:YAG is pumped by a 240-W fiber-coupled cw  $\sim 940$ -nm laser diodes, and  $\sim 75\%$  of the pump energy is

absorbed by the crystal. After the two-pass amplifier, the beam is amplified to 30 mJ and sent to another single-pass amplifier for further amplification. Again, the beam size is adjusted by another telescope. Because of the thermal gradient inside the Yb:YAG crystal, the amplified beam suffers a little astigmatism. Therefore, a periscope is set at the entrance of the single-pass amplifier to compensate the astigmatism by introducing thermal gradient in the other dimension when the pulse enters the second Yb:YAG crystal. The gain medium of the single-pass amplifier is a 2%-doped 20-mm-long Yb:YAG crystal cooled to 77 K inside a Dewar. The pump source is the same as the two-pass amplifier, but ~95% pump energy is absorbed by the crystal due to the higher doping. The maximum energy after the single-pass amplifier is 56 mJ. Fig. 5-4 (a) and Fig. 5-4 (b) show the output beam profiles of the two-pass and the single-pass amplifiers respectively. The amplified pulse is compressed to 17 ps (Fig. 5-4 (c)) using a multi-layer dielectric grating pair with a throughput efficiency of 75%, delivering a maximum compressed energy of 42 mJ. Although the maximum pulse energy is 42 mJ, only 35 mJ is used to pump the OPCPA to avoid superfluorescence.

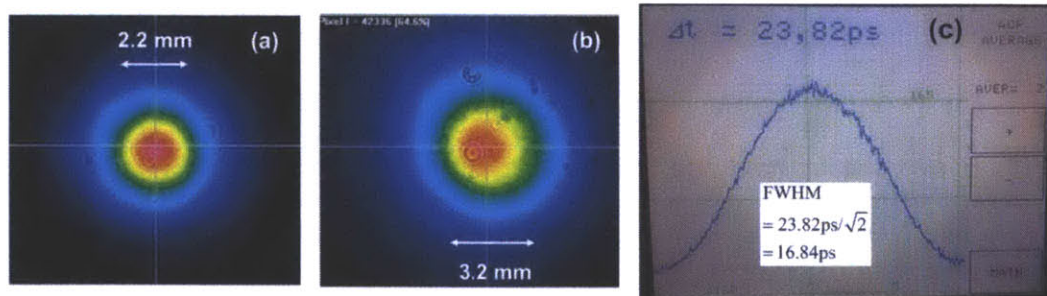


Fig. 5-4 The beam profiles of the outputs of (a) the two-pass amplifier and (b) single-pass amplifier respectively. The circular fringes in the beam profiles are the measurement artifact from neutral density filters. (c) The pulse duration measurement of the compressed 1.03- $\mu\text{m}$  pulse.  $\Delta t$  is the FWHM of the envelope of the electric field, and the FWHM of the intensity is  $\Delta t/\sqrt{2}$ .

### 5.3 HHG Results

The 2.1- $\mu\text{m}$  pulse is focused into a gas cell with two differential pumping stages to generate HH. The gas cell has a simple structure as shown in Fig. 5-5. It stacks five 1/4"-thick 1.33" CF flanges together with four drilled blank copper gaskets in between. The middle three CF flanges with 1/4" gas feedthrough tubes connected on the side walls function as the front differential pumping stage, the gas cell, and the back differential pumping stage respectively. The differential pumping stages help keep the background pressure of the chamber below  $10^{-2}$  mbar while the pressure inside the gas cell may be as high as  $\sim 1$  bar during experiment. The blank copper gaskets have apertures drilled at the centers with desired diameters. In our gas cell, the diameters are either 0.5 mm or 0.6 mm, as indicated in Fig. 5-5.

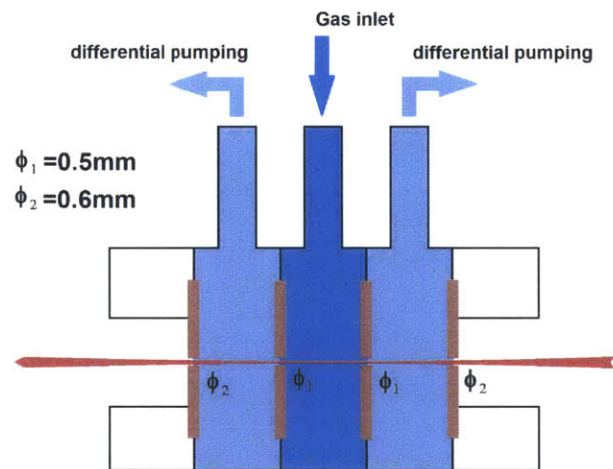


Fig. 5-5 The gas cell with two differential pumping stages.  $\phi_1$  and  $\phi_2$  are the diameters of the apertures on the blank copper gaskets between the CF flanges.

The 2.1- $\mu\text{m}$  beam is focused at the center of the gas cell with a peak intensity of  $\sim 3 \times 10^{14}$  W/cm<sup>2</sup>. Fig. 5-6 shows the HHG spectrum from Ar at a pressure of  $\sim 200$  mbar with a cutoff around 190 eV. Unlike the HHG spectra driven by near-IR or visible wavelengths (cf. Chapter 4), the harmonic peaks in Fig. 5-6 are not resolved. The poor



resolution could be due to the grating of the spectrometer that cannot resolve the high energy photons well, especially when the harmonic peaks are much closer for longer driver wavelengths. The soft X-ray photon flux is measured by a calibrated X-ray photodiode. The photon flux at 160 eV from Ar HHG is  $\sim 2 \times 10^8$  photons/s over 1% bandwidth. The driver energy of 2.1  $\mu\text{m}$  used in these measurements is 0.9 mJ. The shape of the HH spectrum in the range of  $>50$  eV basically follows the transmission curve of Ar, which indicates that the soft X-ray flux is limited by the reabsorption of the HHG medium.

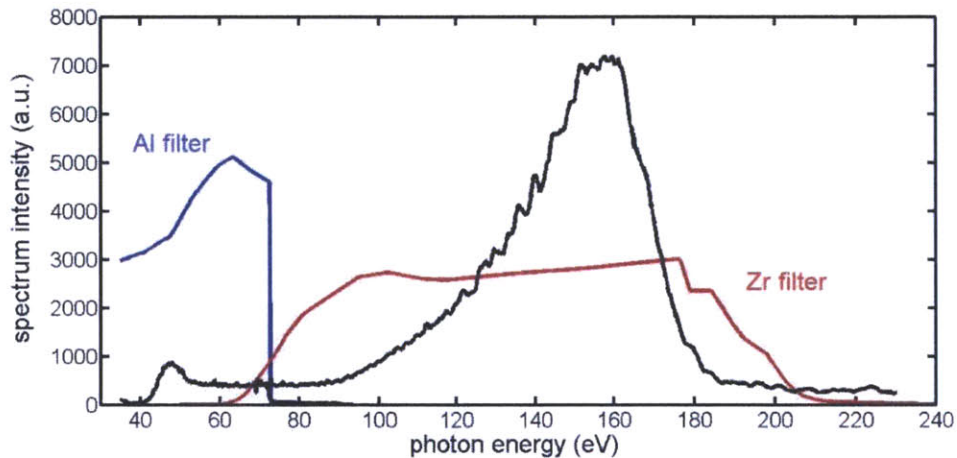


Fig. 5-6 HHG spectrum from Ar (black), and the transmission curves of Al (blue) and Zr (red) filters [80].

To generate water window HHG, the gas in the gas cell is switched to Ne because it has higher ionization potential to sustain higher electric field without generating too much plasma. The intensity at the focus is  $\sim 5 \times 10^{14}$  W/cm<sup>2</sup> with 1.5-mJ pulse energy at the focus. A calibrated photodiode with Ti and carbon coatings is used to detect the photon flux. In addition, two 0.5- $\mu\text{m}$ -thick Ti foils are placed before the photodiode to block the residue of the driver pulse. Therefore, the photodiode should be only responsive to soft X-ray photons between 200-450 eV, as the response curve shows in Fig. 5-7 (a). After the optimization of the input beam size and the focus position, the photodiode shows an optimal signal of

photon flux when the Ne pressure in the gas cell is  $\sim 1.2$  bar. Unfortunately, our toroidal mirror is contaminated by carbon generated by the ionizing vacuum gauge, and thus photons with energy higher than 200 eV are not transferred to the spectrometer. According to the simulation spectrum (Fig. 5-7(b)) with the experimental parameters, the photodiode signal that takes into account the photodiode response and the transmission of the Ti filters corresponds to a photon flux of  $\sim 10^6$  photons/s over 1% bandwidth around 350 eV.

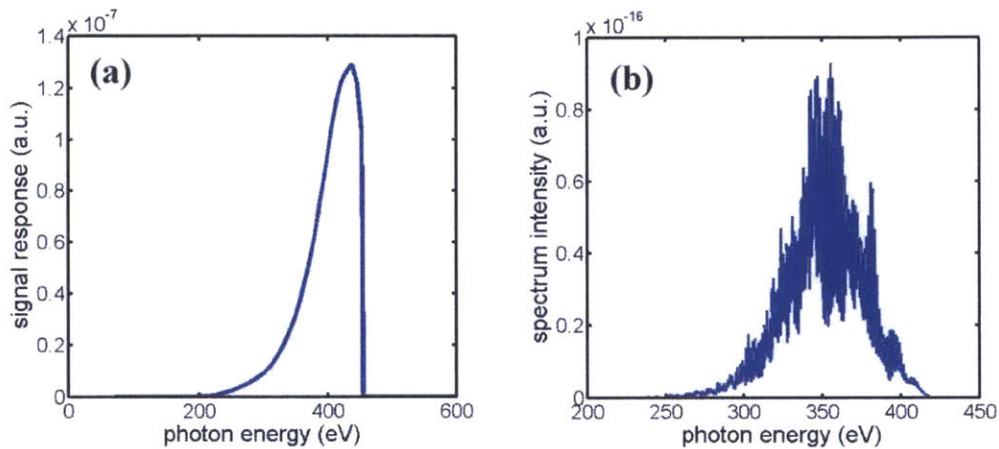


Fig. 5-7 (a) The combined response of the photodiode to different photon energy. The response curve has taken into account the coating layers on the photodiode and two additional 0.5- $\mu\text{m}$ -thick Ti filters. (b) The simulated HHG spectrum of Ne with the experiment parameters.

In summary, we have demonstrated a 2.6-mJ, 39-fs, kHz, 2.1- $\mu\text{m}$  OPCPA system, pumped by 35-mJ, 12-ps, 1029-nm pulses from the cryogenic Yb:YAG amplifier, and high-flux soft X-ray HHG via cutoff extension to 190 eV in Ar. Measured by a calibrated photodiode, the photon flux is  $\sim 2 \times 10^8$  photon/s over 1% bandwidth at 160 eV from Ar. A HHG signal between 300 eV and 400 eV is also observed with 1.2 bar Ne by another calibrated photodiode with selective coatings and filters to measure 200-450 eV signal. The photon flux is  $\sim 10^6$  photon/s over 1% bandwidth at 350 eV, although spectra can not be measured for the time being. This system would be a promising light source for soft X-ray attosecond science as well as biological imaging applications.

**THIS PAGE IS INTENTIONALLY LEFT BLANK**

# Chapter 6

## Conclusion and Future Work

### 6.1 Conclusion

This thesis has covered several topics about HHG. An efficient numerical algorithm to calculate the TDSE for HHG is developed. The feature of the TDSE algorithm is to decompose the radial wave-function by the eigen-functions of the radial part of the TDSE, and simply compute the time-varying coefficients for each eigen-function rather than the detailed structure of the eigen-functions. With a pre-computed library of the eigen-functions of the atom of interest, the algorithm is particularly suitable for testing many different driver waveforms on the same atom, e.g. studying the wavelength scaling characteristics or optimizing the driver waveform for some specific purpose. We next study the TSM with an emphasis on the wavelength scaling of single-atom efficiency (SE). The physical meaning of the  $\lambda^{-(7-8)}$  scaling law for single harmonic efficiency is explained: quantum diffusion accounts for  $\lambda^{-3}$ ; the increasing number of the harmonic peaks accounts for another  $\lambda^{-3}$ ; the rest  $\lambda^{-(1-2)}$  dependence is related to the ionization and recombination phase of the electron and the relative position of the photon energy on the plateau.

While the TSM is supposed to work in the tunneling regime with a negligible Keldysh parameter, we study the wavelength scaling of HHG SE experimentally and theoretically

with visible driver wavelengths and a Keldysh parameter around unity in the transition between the tunneling and the multiphoton ionization regimes. The experimental result shows a less dramatic wavelength scaling than the conventional HHG with IR driver wavelengths and is well explained by our modified TSM that incorporates the non-adiabatic (NA) ionization and the complex ionization time (CIT) from the saddle point method. For HHG close to the multiphoton regime, the CIT can alter the electron traveling time in the TSM and make the wavelength scaling of the SE less dramatic than HHG driven by longer wavelengths in the tunneling regime. In addition, because the CIT removes the singularity from the traveling time in the conventional TSM, we can replace the quasi-static ADK ionization model by the more general non-adiabatic (NA) ionization model without divergence and obtain a modified TSM that works for a wider range of Keldysh parameters.

The influence of plasma defocusing on HHG is another important topic of this thesis. We quantitatively analyzed the influence of plasma defocusing on HHG for different driver wavelengths by defining and comparing the enhancement factor that considers macroscopic characteristics including plasma defocusing, reabsorption of harmonics, and phase-matching. Geometric and dipole phases that are important in the phase-matching of HHG driven by IR or longer wavelengths are also included. Our numerical result shows good agreement with experiment and provides an easy way to calculate and explain HHG performance without referring to the complex microscopic behavior of strong field dynamics and the atomic parameters. Although increasing the medium pressure can partially make up the unfavorable SE with longer driver wavelengths, the compensation is still limited by plasma defocusing. The pulse propagation employed in the study of plasma defocusing here is then combined with the TSM into a fully dimensional HHG simulation program that takes into account most known physics relevant to HHG. The most critical



approximation made in the simulation is the assumption of multi-cycle pulse and the linear approximation of the driver field envelope. By appropriately normalizing the kinematic variables with the driver pulse intensity and the frequency, an efficient algorithm to calculate the TSM dipole response is developed and speeds up the fully dimensional simulation of HHG significantly.

Ultrashort pulses generated from a Ti:sapphire amplifier is the easiest way to generate HH nowadays, and several experiment projects in this thesis are carried out with our multi-mJ Ti:sapphire amplifier. HHG efficiencies driven by the Ti:sapphire wavelength 800 nm and its second harmonic 400 nm are compared. While the wavelength scaling of HHG SE predicts a significant enhancement of SE with the shorter driver wavelength, the actual enhancement can be even larger because shorter driver wavelength is favored by several macroscopic factors including the higher ionization level, lower harmonic order, smaller Gouy phase, and easier phase-matching. Three orders of magnitudes of efficiency enhancement has been observed around 50 eV in He when the driver wavelength is shortened from 800 nm to 400 nm. An OPA system with tunable signal wavelength between 470 nm and 650 nm is built and pumped by the 400-nm pulse generated from the Ti:sapphire amplifier. We used this system to study the wavelength scaling of the SE and the cutoff of HHG driven by visible wavelengths. While the cutoff is consistent with the scaling law found with the near- and mid-IR driver wavelengths, the SE shows a different behavior that can be explained by our modified TSM.

In order to extend the cutoff further into the soft X-ray range, an OPCPA system that generates 2.6-mJ, 39-fs, kHz mid-IR ( $2.1 \mu\text{m}$ ) pulse is developed. The last OPA stage of the OPCPA system is pumped by a cryogenic Yb:YAG system that generates 56-mJ, 17-ps,  $1.029\text{-}\mu\text{m}$  pulse. The two systems are synchronized by seeding from the same oscillator.

OPCPA is known for its energy scalability and the support of high-repetition-rate operation with a high power external pump, which are essential for high-flux soft X-ray generation by HHG. The mid-IR pulse is focused into a differentially-pumped 6mm-long gas cell to generate HH. The HHG spectrum from  $\sim 200$ -mbar Ar shows a cutoff around 190 eV and a photon flux  $\sim 2 \times 10^8$  photon/sec over 1% bandwidth around 160 eV. With 1.2-bar Ne in the gas cell, our photodiode dedicated to 200-450-eV photon measurement detects a photon flux  $\sim 10^6$  photon/sec over 1% bandwidth around 350 eV. Although we have not measured the HHG spectrum of Ne yet, a spectrum around 350 eV is expected by the fully dimensional simulation with the experiment parameters. A HHG-based source driven by mid-IR ultrashort pulses at kHz repetition rate has thus been demonstrated.

## 6.2 Future Work

One important problem to solve about the simulation work is the discrepancy between the HHG efficiencies calculated by the fully dimensional simulation and measured by the experiment. Surprisingly, the calculated efficiency is lower than the experimental result by a few orders of magnitudes. If we track the wave-vector-mismatch  $\Delta k$  between the driver pulse and some harmonic order along the driver pulse propagation, we can find that  $\Delta k$  experiences dramatic change during the propagation that suggests phase-matching over a certain distance is almost impossible. The  $\Delta k$  changes much faster for longer driver wavelength because of the extremely high harmonic order. Even at low pressure conditions, the geometric phase and the dipole phase can kill the phase-matching condition for mid-IR-driven HHG as long as plasma defocusing shows up. The failure to achieve phase-matching in simulation is considered the major reason for the efficiency discrepancy, although we cannot rule out the possibility of incorrect recombination amplitudes used in

the simulation or any new hidden physics. So far, there is not any theoretical work carefully comparing the absolute efficiency with experiment to the best of our knowledge.

For the experiment, it will be great to acquire HHG spectra from Ne driven by the mid-IR pulse to confirm that our OPCPA has generated HH in the water window range (284-543 eV). The water window is defined by the two absorption edges of carbon (284 eV) and oxygen (543 eV), so a water window photon sees strong absorption from carbon (and thus proteins) but good transmission from oxygen (and thus water). On this ground, the water window radiation can be very useful for high resolution (<5 nm) bio- molecule imaging because of its short wavelength. Furthermore, the excellent spatial and temporal qualities due to the nature of HHG also provide high brightness by tight focusing and precise timing, which offers great potential for femtosecond and attosecond study of atomic and molecular and condensed matter dynamics.

Once the generation of water window photon flux is confirmed, the next things to do is to improve the photon flux to  $10^8$  photon/sec over 1% bandwidth, which has been shown to be enough for microscopy application [70]. In Ref. [10], the 1.55- $\mu\text{m}$  driver pulses with 2.2-mJ pulse energy and 40-fs pulse duration are focused on a Ne gas jet having a pressure of 0.76 bar and a width of 2 mm. The focus intensity is estimated as  $3.5 \times 10^{14}$  W/cm<sup>2</sup>, and the measured cutoff is around 400 eV. The generated photon flux is  $2.5 \times 10^6$  photons/shot. In Ref. [12], the 2- $\mu\text{m}$  driver pulses with 2.4-mJ pulse energy and 40-fs pulse duration are focused into a 1cm-long hollow core waveguide with 12-bar of He. The reported cutoff is 520 eV, and the photon flux at 1% bandwidth around 450 eV is  $10^5$  photons/shot, which corresponds to a single harmonic efficiency of  $8 \times 10^{-10}$ . Since our OPCPA generates 2.6-mJ

39-fs 2.1- $\mu\text{m}$  pulse at 1 kHz, there should be room to improve the efficiency to generate sufficient photon flux for water window soft X-ray experiment.

# Bibliography

- [1] J. A. Armstrong, N. Bloembergen, J. Ducuing, and P. S. Pershan, "Interactions between Light Waves in a Nonlinear Dielectric," *Phys. Rev.* **127**, 1918-1939 (1962).
- [2] P. A. Franken, A. E. Hill, C. W. Peters, and G. Weinreich, "Generation of Optical Harmonics," *Phys. Rev. Lett.* **7**, 118-119 (1961).
- [3] P. L. Kelly, "Self-Focusing of Optical Beams," *Phys. Rev. Lett.* **15**, 1005-1008 (1965).
- [4] C. C. Wang and G. W. Racette, "Measurement of parametric gain accompanying optical difference frequency generation," *Appl. Phys. Lett.* **6**, 169-171 (1965).
- [5] I. J. Kim, C. M. Kim, H. T. Kim, G. H. Lee, Y. S. Lee, J. Y. Park, D. J. Cho, and C. H. Nam, "Highly Efficient High-Harmonic Generation in an Orthogonally Polarized Two-Color Laser Field," *Phys. Rev. Lett.* **94**, 243901 (2005).
- [6] I. J. Kim, G. H. Lee, S. B. Park, Y. S. Lee, T. K. Kim, C. H. Nam, T. Mocek, and K. Jakubczak, "Generation of submicrojoule high harmonics using a long gas jet in a two-color laser field," *Appl. Phys. Lett.* **92**, 021125 (2008).
- [7] X. He, M. Miranda, J. Schwenke, O. Guilbaud, T. Ruchon, C. Heyl, E. Georgadiou, R. Rakowski, A. Persson, M. B. Gaarde, and A. L'Huillier, "Spatial and spectral properties of the high-order harmonic emission in argon for seeding applications," *Phys. Rev. A* **79**, 063829 (2009).
- [8] E. J. Takahashi, Y. Nabekawa, H. Mashiko, H. Hirokazu, A. Suda, K. Midorikawa, "Generation of strong optical field in soft X-ray region by using high-order harmonics," *IEEE J. Sel. Top. Quantum Electron.* **10**, 1315-1328 (2004).

- [9] E. L. Falcão-Filho, C.-J. Lai, K.-H. Hong, V. M. Gkortsas, S.-W. Huang, L.-J. Chen, and F. X. Kärtner, "Scaling of high-order harmonic efficiencies with visible wavelength drivers: A route to efficient extreme ultraviolet sources," *Appl. Phys. Lett.* **97**, 061107 (2010).
- [10] E. J. Takahashi, T. Kanai, K. L. Ishikawa, Y. Nabekawa, and K. Midorikawa, "Coherent Water Window X Ray by Phase-Matched High-Order Harmonic Generation in Neutral Media," *Phys. Rev. Lett.* **101**, 253901 (2008).
- [11] C. Ding, W. Xiong, T. Fan, D. D. Hickstein, T. Popmintchev, X. Zhang, M. Walls, M. M. Murnane, and H. C. Kapteyn, "High flux coherent super-continuum soft X-ray source driven by a single-stage, 10mJ, Ti:sapphire amplifier-pumped OPA," *Opt. Express* **22**, 6194-6202 (2014).
- [12] M.-C. Chen, P. Arpin, T. Popmintchev, M. Gerrity, B. Zhang, M. Seaberg, D. Popmintchev, M. M. Murnane, and H. C. Kapteyn, "Bright, Coherent, Ultrafast Soft X-ray Harmonics Spanning the Water Window from a Tabletop Light Source," *Phys. Rev. Lett.* **105**, 173901 (2010).
- [13] J. L. Krause, K. J. Schafer, and K. C. Kulander, "High-order harmonic generation from atoms and ions in the high intensity regime," *Phys. Rev. Lett.* **68**, 3535-3538 (1992).
- [14] P. Dietrich, N. H. Burnett, M. Ivanov, and P. B. Corkum, "High-harmonic generation and correlated two-electron multiphoton ionization with elliptically polarized light," *Phys. Rev. A* **50**, R3585 (1994).
- [15] P. B. Corkum, "Plasma perspective on strong field multiphoton ionization," *Phys. Rev. Lett.* **71**, 1994-1997 (1993).

- [16] P. B. Corkum and F. Krausz, "Attosecond science," *Nat. Phys.* **3**, 381-387 (2007).
- [17] M. Lewenstein, Ph. Balcou, M. Yu. Ivanov, A. L'Huillier, and P. B. Corkum, "Theory of high-harmonic generation by low-frequency laser fields," *Phys. Rev. A* **49**, 2117-2132 (1994).
- [18] E. Goulielmakis, M. Schultze, M. Hofstetter, V. S. Yakovlev, J. Gagnon, M. Uiberacher, A. L. Aquila, E. M. Gullikson, D. T. Attwood, R. Kienberger, F. Krausz, and U. Kleineberg, "Single-Cycle Nonlinear Optics," *Science* **320**, 1614-1617 (2008).
- [19] I. J. Sola, E. Mével, L. Elouga, E. Constant, V. Strelkov, L. Poletto, P. Villoresi, E. Benedetti, J.-P. Caumes, S. Stagira, C. Vozzi, G. Sansone and M. Nisoli, "Controlling attosecond electron dynamics by phase-stabilized polarization gating," *Nat. Phys.* **2**, 319-322 (2006).
- [20] H. Mashiko, S. Gilbertson, C. Li, E. Moon, and Z. Chang, "Optimizing the photon flux of double optical gated high-order harmonic spectra," *Phys. Rev. A* **77**, 063423 (2008).
- [21] F. Ferrari, F. Calegari, M. Lucchini, C. Vozzi, S. Stagira, G. Sansone, and M. Nisoli, "High-energy isolated attosecond pulses generated by above-saturation few-cycle fields," *Nat. Photon.* **4**, 875-879 (2010).
- [22] M. Uiberacker, Th. Uphues, M. Schultze, A. J. Verhoef, V. Yakovlev, M. F. Kling, J. Rauschenberger, N. M. Kabachnik, H. Schröder, M. Lezius, K. L. Kompa, H.-G. Müller, M. J. J. Vrakking, S. Hendel, U. Kleineberg, U. Heinzmann, M. Drescher & F. Krausz, "Attosecond real-time observation of electron tunneling in atoms," *Nature (London)* **446**, 627-632 (2007).

- [23] A. L. Cavalieri, N. Müller, Th. Uphues, V. S. Yakovlev, A. Baltuška, B. Horvath, B. Schmidt, L. Blümel, R. Holzwarth, S. Hendel, M. Drescher, U. Kleineberg, P. M. Echenique, R. Kienberger, F. Krausz & U. Heinzmann, "Attosecond spectroscopy in condensed matter," *Nature (London)* **449**, 1029-1032 (2007).
- [24] M. Schultze, M. Fieß, N. Karpowicz, J. Gagnon, M. Korbman, M. Hofstetter, S. Neppl, A. L. Cavalieri, Y. Komninos, Th. Mercouris, C. A. Nicolaides, R. Pazourek, S. Nagele, J. Feist, J. Burgdörfer, A. M. Azzeer, R. Ernstorfer, R. Kienberger, U. Kleineberg, E. Goulielmakis, F. Krausz, and V. S. Yakovlev, "Delay in Photoemission," *Science* **328**, 1658-1662 (2010).
- [25] E. J. Takahashi, P. Lan, O. D. Mücke, Y. Nabekawa, and K. Midorikawa, "Attosecond nonlinear optics using gigawatt-scale isolated attosecond pulses," *Nat. Commun.* **4**, 2691 (2013).
- [26] H. J. Wörner, H. Niikura, J. B. Bertrand, P. B. Corkum, and D. M. Villeneuve, "Observation of Electronic Structure Minima in High-Harmonic Generation," *Phys. Rev. Lett.* **102**, 103901 (2009).
- [27] M. C. H. Wong, A.-T. Le, A. F. Alharbi, A. E. Boguslavskiy, R. R. Lucchese, J.-P. Brichta, C. D. Lin, and V. R. Bhardwaj, "High Harmonic Spectroscopy of the Cooper Minimum in Molecules," *Phys. Rev. Lett.* **110**, 033006 (2013).
- [28] A. D. Shiner, B. E. Schmidt, C. Trallero-Herrero, H. J. Wörner, S. Patchkovskii, P. B. Corkum, J.-C. Kieffer, F. Légaré, D. M. Villeneuve, "Probing collective multi-electron dynamics in xenon with high-harmonic spectroscopy," *Nat. Phys.* **7**, 464-467 (2011).



- [29] J. Itatani, J. Levesque, D. Zeidler, H. Niikura, H. Pépin, J. C. Kieffer, P. B. Corkum and D. M. Villeneuve, "Tomographic imaging of molecular orbitals," *Nature (London)* **432**, 867-871 (2004).
- [30] C. J. Joachain, N. J. Kylstra, and R. M. Potvliege, *Atoms in Intense Laser Fields* (Cambridge University Press, New York 2012), Chap. 5.
- [31] H. G. Muller, "Numerical simulation of high-order above-threshold-ionization enhancement in argon," *Phys. Rev. A* **60**, 1341-1350 (1999).
- [32] M. Y. Ivanov, T. Brabec, and N. Burnett, "Coulomb corrections and polarization effects in high-intensity high-harmonic emission," *Phys. Rev. A* **54**, 742-745 (1996).
- [33] A. Gordon and F. X. Kärtner, "Quantitative Modeling of Single Atom High Harmonic Generation," *Phys. Rev. Lett.* **95**, 223901 (2005).
- [34] M. Y. Ivanov, M. Spanner, and O. Smirnova, "Anatomy of strong field ionization," *J. Mod. Opt.* **52**, 165-184 (2005).
- [35] E. L. Falcão-Filho, V. M. Gkortsas, A. Gordon and F. X. Kärtner, "Analytic scaling analysis of high harmonic generation conversion efficiency," *Opt. Express* **17**, 11217-11229 (2009).
- [36] V. S. Yakovlev, M. Ivanov, and F. Krausz, "Enhanced phase-matching for generation of soft X-ray harmonics and attosecond pulses in atomic gases," *Opt. Express* **15**, 15351-15364 (2007).
- [37] A.-T. Le, R. R. Lucchese, S. Tonzani, T. Morishita, and C. D. Lin, "Quantitative rescattering theory for high-order harmonic generation from molecules," *Phys. Rev. A* **80**, 013401 (2009).

- [38] J. Tate, T. Augustine, H. G. Muller, P. Salières, P. Agostini, and L. F. DiMauro, "Scaling of Wave-Packet Dynamics in an Intense Midinfrared Field," *Phys. Rev. Lett.* **98**, 013901 (2007).
- [39] K. Schiessl, K. L. Ishikawa, E. Persson, and J. Burgdörfer, "Quantum Path Interference in the Wavelength Dependence of High-Harmonic Generation," *Phys. Rev. Lett.* **99**, 253903 (2007).
- [40] M. V. Frolov, N. L. Manakov, T. S. Sarantseva, M. Yu. Emelin, M. Yu. Ryabikin, and A. F. Starace, "Analytic Description of the High-Energy Plateau in Harmonic Generation by Atoms: Can the Harmonic Power Increase with Increasing Laser Wavelengths?" *Phys. Rev. Lett.* **102**, 243901 (2009).
- [41] T. Augustine, F. Catoire, P. Agostini, L. F. DiMauro, C. C. Chirila, V. S. Yakovlev, and P. Salières, "Driving-frequency scaling of high-harmonic quantum paths," *New J. Phys.* **14**, 103014 (2012).
- [42] A. D. Shiner, C. Trallero-Herrero, N. Kajumba, H.-C. Bandulet, D. Comtois, F. Légaré, M. Giguère, J.-C. Kieffer, P. B. Corkum, and D. M. Villeneuve, "Wavelength Scaling of High Harmonic Generation Efficiency," *Phys. Rev. Lett.* **103**, 073902 (2009).
- [43] C.-J. Lai, G. Cirmi, K.-H. Hong, J. Moses, S.-W. Huang, E. Granados, P. Keathley, S. Bhardwaj, and F. X. Kärtner, "Wavelength scaling of high harmonic generation close to the multiphoton ionization regime," *Phys. Rev. Lett.* **111**, 073901 (2013).
- [44] D. R. Austin and J. Biegert, "Strong-field approximation for the wavelength scaling of high-harmonic generation," *Phys. Rev. A* **86**, 023813 (2012).

- [45] C. Jin, A.-T. Le, and C. D. Lin, "Medium propagation effects in high-order harmonic generation of Ar and N<sub>2</sub>," *Phys. Rev. A* **83**, 023411 (2011).
- [46] M. V. Ammosov, N. B. Delone, and V. P. Krainov, "Tunnel ionization of complex atoms and atomic ions by an alternating electromagnetic field," *Sov. Phys. JETP* **64**, 1191-1194 (1986).
- [47] T. Ditmire, J. K. Crane, H. Nguyen, L. B. DaSilva, M. D. Perry, "Energy-yield and conversion-efficiency measurement of high-order harmonic radiation," *Phys. Rev. A* **51**, R902 (1995).
- [48] L. V. Keldysh, "Ionization in the field of a strong electromagnetic wave," *Sov. Phys. JETP* **20**, 1307-1314 (1965).
- [49] D. Shafir, H. Soifer, B. D. Bruner, M. Dagan, Y. Mairesse, S. Patchkovskii, M. Yu. Ivanov, O. Smirnova, and N. Dudovich, "Resolving the time when an electron exits a tunneling barrier," *Nature (London)* **485**, 343-346 (2012).
- [50] L. Torlina and O. Smirnova, "Time-dependent analytical R-matrix approach for strong-field dynamics. I. One-electron systems," *Phys. Rev. A* **86**, 043408 (2012).
- [51] G. L. Yudin and M. Yu. Ivanov, "Nonadiabatic tunnel ionization: Looking inside a laser cycle," *Phys. Rev. A* **64**, 013409 (2001).
- [52] D. R. Austin and J. Biegert, "Strong-field approximation for the wavelength scaling of high-harmonic generation," *Phys. Rev. A* **86**, 023813 (2012).
- [53] V.-M. Gkortsas, S. Bhardwaj, C.-J. Lai, K.-H. Hong, E. L. Falcão-Filho, and F. X. Kärtner, "Interplay of multiphoton and tunneling ionization in short-wavelength-driven high-order harmonic generation," *Phys. Rev. A* **84**, 013427 (2011).

- [54] V. M. Gkortsas, S. Bhardwaj, E. L. Falcão-Filho, K.-H. Hong, A. Gordon, and F. X. Kärtner, "Scaling of high harmonic generation conversion efficiency," *J. Phys. B: At. Mol. Opt. Phys.* **44**, 045601 (2011).
- [55] C.-J. Lai and F. X. Kärtner, "The influence of plasma defocusing in high harmonic generation," *Opt. Express* **19** 22377-22387 (2011).
- [56] P. Salières, A. L'Huillier, M. Lewenstein, "Coherence Control of High-Order Harmonics," *Phys. Rev. Lett.* **74**, 3776-3779 (1995).
- [57] T. Popmintchev, M.-C. Chen, A. Bahabad, M. Gerrity, P. Sidorenko, O. Cohen, I. P. Christov, M. M. Murnane, and H. C. Kapteyn, "Phase matching of high harmonic generation in the soft and hard X-ray regions of the spectrum," *Proc. Natl. Acad. Sci. USA* **106**, 10516-10521 (2009).
- [58] C. Altucci, T. Starczewski, E. Mevel, C.-G. Wahlstrom, B. Carre, and A. L'Huillier, "Influence of atomic density in high-order harmonic generation," *J. Opt. Soc. Am. B* **13**(1), 148-156 (1996).
- [59] E. Constant, D. Garzella, P. Breger, E. Mevel, Ch. Dorrer, C. Le Blanc, F. Salin, and P. Agostini, "Optimizing High Harmonic Generation in Absorbing Gases: Model and Experiment," *Phys. Rev. Lett.* **82**, 1668-1671 (1999).
- [60] M. Geissler, G. Tempea, A. Scrinzi, M. Schnurer, F. Krausz, and T. Brabec, "Light Propagation in Field-Ionizing Media: Extreme Nonlinear Optics," *Phys. Rev. Lett.* **83**, 2930-2933 (1999).

- [61] S. Kazamias, S. Daboussi, O. Guilbaud, K. Cassou, D. Ros, B. Cros, and G. Maynard, “Pressure-induced phase matching in high-order harmonic generation,” *Phys. Rev. A* **83**, 063405 (2011).
- [62] H. Dachraoui, T. Auguste, A. Helmstedt, P. Bartz, M. Michelswirth, N. Mueller, W. Pfeiffer, P. Salieres, and U. Heinzmann, “Interplay between absorption, dispersion and refraction in high-order harmonic generation,” *J. Phys. B: At. Mol. Opt. Phys.* **42**, 175402 (2009).
- [63] Maciej Lewenstein, Pascal Salières, and Anne L’Huillier, “Phase of the atomic polarization in high-order harmonic generation,” *Phys. Rev. A* **52**, 4747-4754 (1995).
- [64] Marvin J. Weber, *Handbook of Optical Materials* (CRC Press, 2003), Chap. 6.
- [65] B. L. Henke, E. M. Gullikson, and J. C. Davis, “X-ray interactions: photoabsorption, scattering, transmission, and reflection at  $E=50\text{-}30000$  eV,  $Z=1\text{-}92$ ,” *Atomic Data and Nuclear Data Tables* **54**, 181-342 (1993).
- [66] G. Cirmi, C.-J. Lai, E. Granados, S.-W. Huang, A. Sell, K.-H. Hong, J. Moses, P. Keathley, and F. X. Kärtner, “Cut-off scaling of high-harmonic generation driven by a femtosecond visible optical parametric amplifier,” *J. Phys. B: At. Mol. Opt. Phys.* **45**, 205601 (2012).
- [67] H. T. Kim, d. G. Lee, K.-H. Hong, J.-H. Kim, I. W. Choi, and C. H. Nam, *Phys. Rev. A* “Continuously tunable high-order harmonics from atoms in an intense femtosecond laser field,” **67**, 051801 (2003).
- [68] H. Dachraoui, T. Auguste, A. Helmstedt, P. Bartz, M. Michelswirth, N. Mueller, W. Pfeiffer, P. Salieres, and U. Heinzmann, “Interplay between absorption, dispersion and

refraction in high-order harmonic generation,” *J. Phys. B: At. Mol. Opt. Phys.* **42**, 175402 (2009).

[69] T. Popmintchev, M.-C. Chen, D. Popmintchev, P. Arpin, S. Brown, S. Alisauskas, G. Andriukaitis, T. Balciunas, O. Muecke, A. Pugzlys, A. Baltuska, B. Shim, S. E. Schrauth, A. Gaeta, C. Hernandez-Garcia, L. Plaja, A. Becker, A. Jaron-Becker, M. M. Murnane, and H. C. Kapteyn, “Bright Coherent Ultrahigh Harmonics in the keV X-ray Regime from Mid-Infrared Femtosecond Lasers,” *Science* **336**, 1287-1291 (2012).

[70] D. H. Martz, M. Selin, O. von Hofsten, E. Fogelqvist, A. Holmberg, U. Vogt, H. Legall, G. Blobel, C. Seim, H. Stiel, and H. M. Hertz, “High average brightness water window source for short-exposure cryomicroscopy,” *Opt. Lett.* **37**, 4425-4427 (2012).

[71] H. Xiong, H. Xu, Y. Fu, J. Yao, B. Zeng, W. Chu, Y. Cheng, Z. Xu, E. J. Takahashi, K. Midorikawa, X. Liu, and J. Chen, “Generation of a coherent x ray in the water window region at 1 kHz repetition rate using a mid-infrared pump source,” *Opt. Lett.* **34**, 1747-1749 (2009).

[72] N. Ishii, K. Kaneshima, K. Kitano, T. Kanai, S. Watanabe, and J. Itatani, “Carrier-envelope phase-dependent high harmonic generation in the water window using few-cycle infrared pulses,” *Nat. Commun.* **5**, 3331 (2014).

[73] K.-H. Hong, S.-W. Huang, J. Moses, X. Fu, C.-J. Lai, G. Cirmi, A. Sell, E. Granados, P. Keathley, and F. X. Kärtner, “High-energy, phase-stable, ultrabroadband kHz OPCPA at 2.1mm pumped by a picosecond cryogenic Yb:YAG laser,” *Opt. Express* **19**, 15538-15548 (2011).

[74] J. Moses, S.-W. Huang, K.-H. Hong, O. D. Mücke, E. L. Falcão-Filho, A. Benedick, F. Ö. Ilday, A. Dergachev, J. A. Bolger, B. J. Eggleton, and F. X. Kärtner, “Highly stable

ultrabroadband mid-IR optical parametric chirped-pulse amplifier optimized for superfluorescence suppression," *Opt. Lett.* **34**, 1639-1641 (2009).

[75] A. Dubietis, R. Butkus, and A. P. Piskarskas, "Trends in Chirped Pulse Optical Parametric Amplification," *IEEE J. Sel. Top. Quantum Electron.* **12**, 163-172 (2006).

[76] T. Metzger, A. Schwarz, C. Y. Teisset, D. Sutter, A. Killi, R. Kienberger, and F. Krausz, "High-repetition-rate picosecond pump laser based on a Yb:YAG disk amplifier for optical parametric amplification," *Opt. Lett.* **34**, 2123-2125 (2009).

[77] M. Chyla, T. Miura, M. Smrz, H. Jelinkova, A. Endo, and T. Mocek, "Optimization of beam quality and optical-to-optical efficiency of Yb:YAG thin-disk regenerative amplifier by pulsed pumping," *Opt. Lett.* **39**, 1441-1444 (2014).

[78] K.-H. Hong, J. Gopinath, D. Rand, A. Siddiqui, S.-W. Huang, E. Li, B. Eggleton, John D. Hybl, T. Y. Fan and F. X. Kärtner, "High-energy, kHz-repetition-rate, ps cryogenic Yb:YAG chirped-pulse amplifier," *Opt. Lett.* **35**, 1752-1754 (2010).

[79] Y. Deng, A. Schwarz, H. Fattahi, M. Ueffing, X. Gu, M. Ossiander, T. Metzger, V. Pervak, H. Ishizuki, T. Taira, T. Kobayashi, G. Marcus, F. Krausz, R. Kienberger, and N. Karpowicz, "Carrier-envelope-phase-stable, 1.2 mJ, 1.5 cycle laser pulses at 2.1  $\mu\text{m}$ ," *Opt. Lett.* **37**, 4973-4975 (2012).

[80] B.L. Henke, E.M. Gullikson, and J.C. Davis, "X-ray interactions: photoabsorption, scattering, transmission, and reflection at E=50-30000 eV, Z=1-92," *At. Data and Nucl. Data Tables* **54**, 181-342 (1993).